IVAN PIQUER ROBLEDO

Oceanography data acquisition and analysis

UNIVERSIDADE DO ALGARVE

Faculty of Science and Technology

2025

IVAN PIQUER ROBLEDO

Oceanography data acquisition and analysis

GIS project for the master's degree

Work carried out under the guidance of:

Professor Dr. Adam Gauci

Professor Dr. Helena Fernandez

UNIVERSIDADE DO ALGARVE

Faculty of Science and Technology

2025

Oceanography data acquisition and analysis

Statement of Authorship

I declare that I am the author of this work, which is original and unpublished. Authors and work consulted are duly cited in the text and included in the reference list.

(Ivan Piquer Robledo)

Acknowledgments

Finishing this thesis wasn't just about checking an academic box, it was a personal journey that tested and grew me in ways I never expected. I couldn't have done it without the incredible people who supported me along the way.

First, to my girlfriend, family and closest friends: thank you for being my constant source of strength and for your love. The sacrifices of time spent apart were crucial during this overseas period.

To my supervisors, Dr. Adam Gauci and Dr. Helena Fernandez: your patience and wisdom were encouraging. You pushed me to think deeply, kindly called out my fuzzy logic and somehow made even the most tedious revisions feel purposeful. Before starting this journey, I never thought I could make it.

And to the faculty and colleagues who offered advice, shared resources or just lent an ear:

Muito obrigado / Muchas gracias / Moltes gràcies

Abstract

Detailed bathymetry is necessary for reliable coastal zone management and operations. While traditional in-situ echo sounding offers high precision, it suffers from inefficiencies in shallow waters and incurs logistical costs. Similarly, LiDAR mapping provides efficient coverage of coastal areas but comes with high acquisition expenses. In contrast, Satellite Derived Bathymetry presents a more cost-effective alternative for mapping coastal regions, albeit typically at a lower resolution. This study addresses the need for precise shallow water bathymetry around the Maltese Islands by integrating in-situ and remote data from Landsat 9, Planet Scope and Sentinel 2-A satellites. We investigate both conventional linear regression models and advanced machine learning techniques, specifically the Random Forest algorithm. An empirical workflow was developed from various band combinations, calibrated against extensive on-site measurements. The research provides a comprehensive insight into the depth accuracy achievable for shallow coastal regions using these diverse satellite platforms and modeling approaches, contributing to more efficient and reliable bathymetric mapping for coastal applications.

Keywords: **bathymetry**, **satellite derived bathymetry**, **machine learning**, **Random Forest**

Resumo

A batimetria detalhada é essencial para uma gestão eficaz das zonas costeiras e as operações marítimas. Métodos tradicionais oferecem alta precisão, mas são ineficientes em águas rasas e envolvem custos logísticos elevados. Alternativamente, o mapeamento por LiDAR proporciona cobertura eficiente de áreas costeiras, porém com custos de aquisição significativos. Em contraste, a Batimetria Derivada de Satélite surge como uma solução mais económica para o mapeamento costeiro, embora geralmente com resolução mais baixa. Este estudo aborda a utilização desta técnica em águas rasas ao redor das ilhas maltesas, integrando dados dos satélites Landsat 9, Planet Scope e Sentinel 2-A. Foi desenvolvido um fluxo de trabalho empírico baseado em diversas combinações de bandas espectrais, calibrando-as com medições extensivas in-situ. Posteriormente, foram investigados tanto modelos convencionais de regressão linear quanto técnicas avançadas de *machine learning*, especificamente o algoritmo Random Forest.

Os resultados demonstraram que os modelos de regressão linear convencional apresentaram tendência de superestimação da profundidade, especialmente na St. Paul Bay, enquanto o algoritmo Random Forest mostrou-se mais robusto, capturando relações não lineares e reduzindo a necessidade de segmentação manual por faixas de profundidade. O Sentinel 2-A exibiu variações de desempenho dependendo da localização, com previsões equilibradas na Ghadira Bay, mas subestimando profundidades em St. Paul Bay, destacando a influência das condições locais nos resultados.

Esta pesquisa oferece uma alternativa viável às técnicas tradicionais de sondagem para monitoramento costeiro, gestão ambiental, segurança na navegação e avaliação de riscos. A alta resolução temporal e espacial dos dados satelitais permite capturar mudanças sazonais e de longo prazo em ecossistemas costeiros, além de auxiliar no estudo do transporte de sedimentos.

Apesar dos avanços, limitações persistem na hora de utilizar a Batimetria Derivada de Satélite. Certas variáveis podem introduzir incertezas, mas métodos bem calibrados minimizam estas. Recomenda-se a expansão e diversificação de conjuntos de dados de treinamento, o desenvolvimento de técnicas de correção e a incorporação de mais fatores ambientais no

processo. A exploração de abordagens de *machine learning* pode melhorar ainda mais as previsões de mudanças sazonais e de longo prazo, enquanto a validação com dados reais de Malta garantirá a confiabilidade e aplicabilidade do modelo.

Palavras-chave: **batimetria**, **batimetria derivada de satélite**, ***machine learning***, **Random Forest**

Index

Figures index

Tables index

Acronyms

AUV - Autonomous Underwater Vehicle

CSV - Comma Separated Values

EROS - Earth Resources Observation and Science

ESA - European Space Agency

GIS - Geographic Information System

LiDAR - Light Detection and Ranging

MAE - Mean Absolute Error

MBES - Multibeam EchoSounder

ML – Machine Learning

MSI - MultiSpectral Instrument

NIR - Near-Infrared

OOB - Out-of-Bag

OLI - Operational Land Imager

pSDB - pseudo-depth value

Q - Q - Quantile-Quantile

R^2 - Coefficient of determination

RF - Random Forest

RMSE - Root Mean Square Error

ROV - Remotely Operated Vehicle

RSV - Remote Surface Vessel

SDB - Satellite-Derived Bathymetry

SBES - Single-Beam EchoSounder

TIRS - Thermal Infrared Sensor

USGS - United States Geological Survey

1. Introduction

The oceans cover 362 million km² of the Earth's surface, playing a prime role in environmental balance and human activities. Within this vast expanse, coastal zones assume vital importance from social, economic and biological perspectives (Wölfl *et al*., 2019). Home to 10% of the world's population in low-elevation areas, these sectors are particularly exposed to risks exacerbated by natural hazards, intensified by both climate change and anthropogenic pressures (Lichter *et al*., 2011). Consequently, the continuous study of the evolution of coastal marine environments is essential to anticipate hydrometeorological hazards (Lubac *et al*., 2022). In this context, bathymetric monitoring stands as a key parameter. This scientific discipline is responsible for measuring water depths to map and characterize the topography of the submerged terrain (Cesbron *et al*., 2021).

Approximately 50% of the world's coastal zone lacks updated bathymetric maps and, in many regions, including Europe, available information is incomplete or decades old (Fitton *et al.*, 2021). Therefore, precise knowledge of underwater terrain characteristics is needed since it facilitates various applications, including the creation of realistic three-dimensional hydrodynamic representations, the exploration of submerged landscapes and archaeological sites, coastal climate assessment (Amrari *et al.*, 2021) and the dredging of ports and waterways, in addition to resource management (Duan *et al.*, 2022).

Traditionally, bathymetric studies have primarily relied on acoustic echo sounding. This technique, which measures depth using sound waves, is mainly implemented through two systems: the Single-Beam EchoSounder (SBES), which offers a less detailed view and limited coverage and the Multibeam EchoSounder (MBES), which, by covering a larger area and recording multiple depth points simultaneously, provides a completer and more meticulous image of the seabed (Janowski *et al.*, 2018). Nevertheless, these techniques have limitations in shallow water environments, with depths of only a few tenths of a meter (Han *et al.,* 2023).

Moreover, a challenge in coastal zones and one closely linked to bathymetry, is the issue of sediment transport. The variable interplay of currents, waves and human activities can lead to substantial erosion and deposition, dramatically altering the seabed and impacting coastal stability (Wang & Andutta, 2013). The resulting sediment displacement can have detrimental effects, including the loss of beaches, damage to coastal infrastructure and the smothering of

sensitive marine ecosystems (Vanneste *et al.*, 2014). Understanding the patterns and rates of sediment transport requires reliable bathymetric data, as changes in water depth can notably influence sediment fluctuations (Szczyrba *et al.*, 2024). Therefore, monitoring bathymetric changes is needed for managing coastal erosion and mitigating the negative impacts of sediment transport.

In recent years, various modern methodologies have been incorporated, such as airborne Light Detection and Ranging (LiDAR), the use of Remotely Operated Vehicles (ROVs) and Autonomous Underwater Vehicles (AUV) for the determination of depth in coastal waters. Despite their robustness, the high operational cost of these hydrographic surveys restricts the performance of repetitive and frequent studies in all areas of interest (Ashphaq *et al.,* 2021). Thus, Satellite-Derived Bathymetry (SDB) has emerged as a viable alternative over the past five decades, especially for characterizing coastal regions with high sedimentary and complex morphology. While SDB represents a valuable solution, the accuracy of its results depends on the availability and quality of *in-situ* bathymetric data and meteorology (Chénier *et al.*, 2019). Based on principles of underwater optics and the analysis of water spectral reflectance, SDB employs specific algorithms for the derivation of bathymetric information from optical remote sensing data (Zhang & Al Shehhi, 2025). Its wide coverage allows obtaining information at different spatial and temporal scales, offering an economical solution (Giordan *et al.*, 2018). Given the obsolescence or inaccessibility of traditional bathymetric data, the integration of *in-situ* information and SDB data is presented as a key technique for the exhaustive characterization of shallow coastal zones.

The present research focuses on the Maltese archipelago, located in the heart of the Mediterranean, between Sicily and the North African coast. The Maltese Islands consist of three main islands - Malta, Gozo and Comino - along with several islets and rocks, covering a total land area of 316.75 km^2 (Thomas *et al.*, 2021). Geologically, the archipelago extends over the northern edge of the Pantelleria rift, an active graben system from the late Miocene to the present, connecting Europe and Africa (French *et al.*, 2020). The bathymetry bordering the eastern flank of the islands is characterized by a wide, flat continental shelf, bounded by a linear escarpment parallel to the coast. In contrast, the western side presents a few hundred meters from the coast and including steep escarpments of around 100 m in height.

This complex coastal morphology, combined with wave exposure and the islands' geological background, makes sediment transport a particularly relevant process in Malta (Sammut *et al*., 2017). Correct bathymetric data is pivotal for understanding and modeling these sediment transport pathways. Given this, the present study proposes the development of a bathymetric reconstruction of two coastal regions of the Maltese archipelago, using remote sensing satellite data and *in-situ* technologies. This system will then be refined using various machine learning algorithms to identify the most exact one. Finally, its extrapolation will enable the application of the methodology to the remaining coastal areas of the country, facilitating the creation of bathymetric models for those and a holistic understanding of coastal sediment transportation.

2. Dissertation structure

This dissertation is structured around three key conceptual strategies in the Geographic Information Systems (GIS) software ArcGIS Pro 3.4.0: acquisition, analysis and validation. The acquisition stage focuses on the collection of both on-site bathymetric data and satellite-derived reflectance. The analysis section details the development of a robust SDB estimation workflow, including the application of Machine Learning (ML) algorithms to improve accuracy. Validation assesses the accuracy of the predicted bathymetry, evaluates the efficacy of the ML techniques and compares results obtained from different satellite platforms.

Figure 2.1 - RSV Powerdolphin produced by PowerVision

1. **Acquisition:**
    - In-situ data: previously collected through the BathMalta project, a two-year program that concluded in November 2024. For the very nearshore coastal zone,

on-site bathymetric data was gathered by using a PowerDolphin (Figure 2.1). This is an Remote Surface Vessel (RSV), produced by PowerVision. Additionally, depth readings from other areas were sourced from using the Voxometer, a high-resolution sonar system utilizing voxel measurement technology.

- Satellite image mosaics: three different satellites were utilized:
    I. The Sentinel 2-A MultiSpectral Instrument (MSI) Level 2-A product (ID: S2A_MSIL2A_20241217T095421_N0511_R079_T33SVV_20241217T121249.SAFE) (Figure 2.2) was acquired on December 17, 2024, through the European Space Agency (ESA) Copernicus Data Ecosystem. The revisit frequency is approximately 10 days. This 10 m spatial resolution product included the download of the following bands: blue (B02), green (B03), red (B04) and near-infrared (NIR) (B08), all at 10 m resolution.

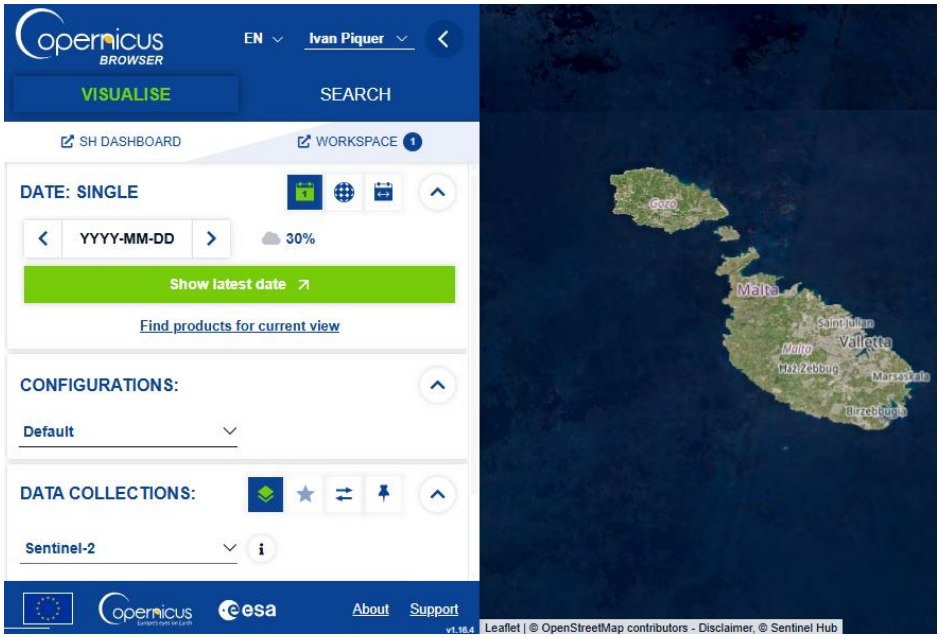

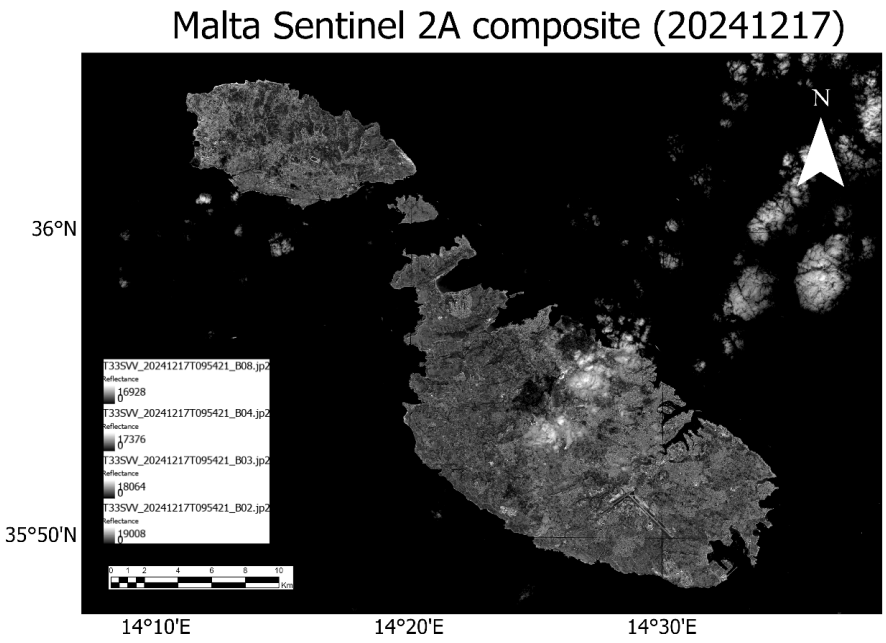

Figure 2.2 - Screenshot from the Copernicus Data Space Ecosystem showing Sentinel 2-A data download (top) and a grayscale Sentinel 2-A composite (December 17, 2024), represented by bands B08, B04, B03 and B02 (bottom)

II. The Landsat 9 Operational Land Imager (OLI) and Thermal Infrared Sensor (TIRS) Level-2SP product (acquired on November 1, 2024) (Figure 2.3) was retrieved from the United States Geological Survey (USGS) Earth Resources Observation and Science (EROS) Center. The Level-2SP processing includes atmospheric correction and provides surface reflectance values. For this study, bands B02, B03, B04 and NIR (B05) were used, all at a 30 m spatial resolution.

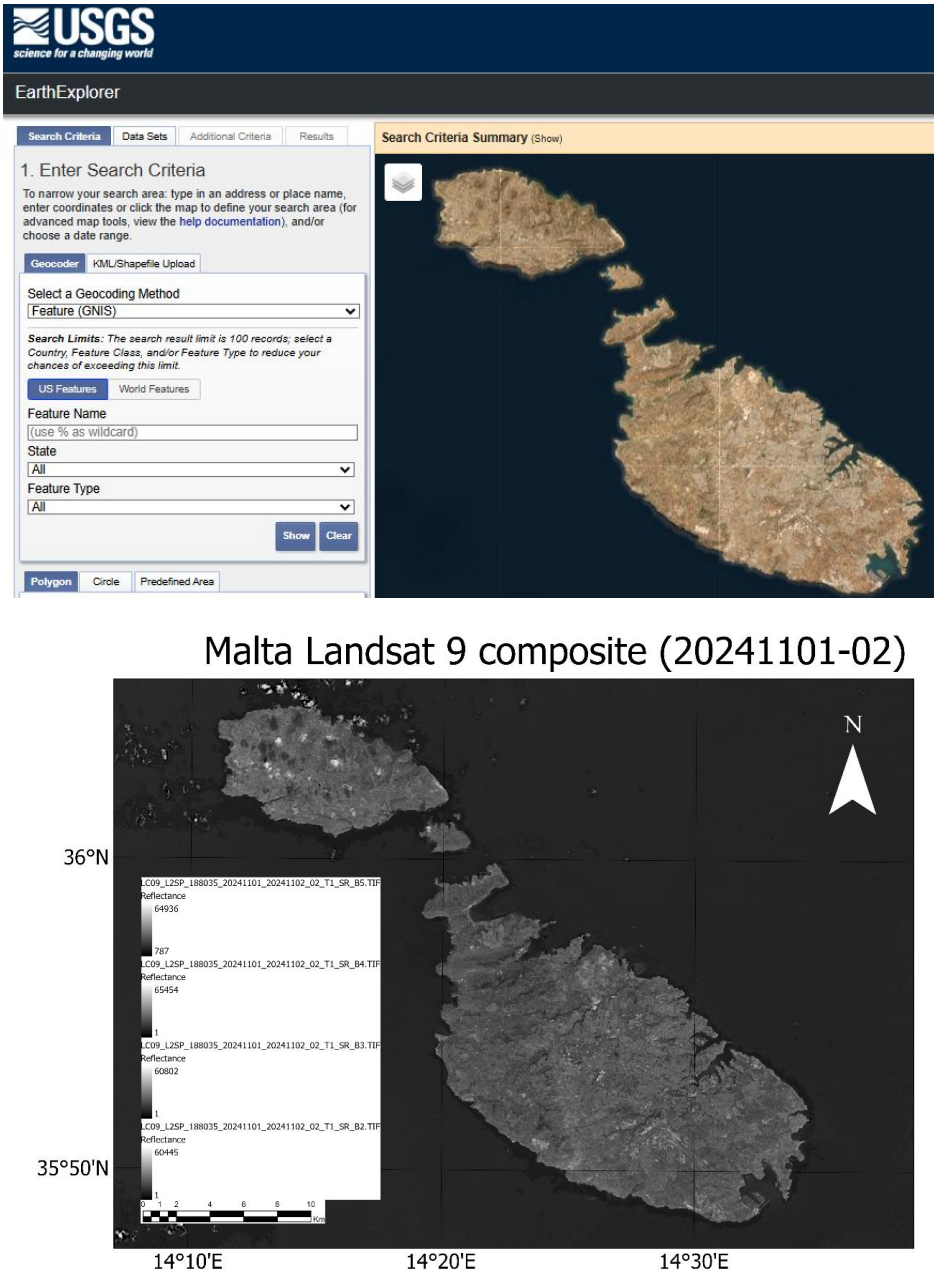

Figure 2.3 - Screenshot from the USGS EROS center showing Landsat 9 data download (top) and a grayscale Landsat 9 composite (1st and 2nd of November 2024), represented by bands B05, B04, 3 and B02 (bottom)

III. The Planet Scope Level-3B AnalyticMS product (ID: 20231027_085644_22_24c3_3B_AnalyticMS) (Figure 2.4) was acquired on October 27, 2023, through Planet Labs PBC and provided by the University of Malta to consider it in the study. Due to the large number of satellites, Planet Scope can provide limited daily coverage of the Earth.

This 3 m spatial resolution product included the download of the following bands: B01, B02, B03 and B04.

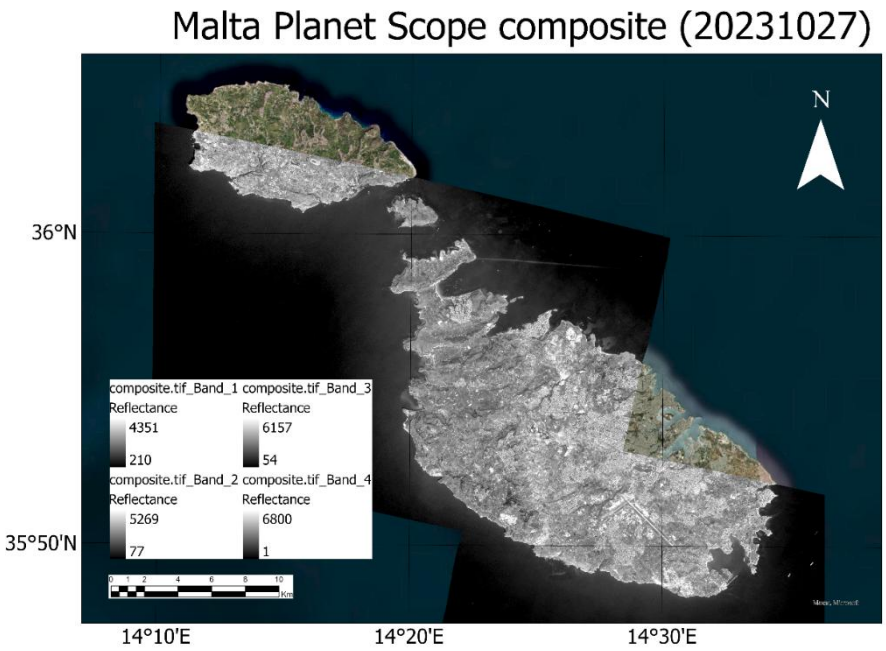

Figure 2.4 - Grayscale Planet Scope composite (October 27, 2023) represented by bands B04, B03 B02 and B01

2. **Analysis:**
    - Determination of the calculated pseudo-depth value (pSDB).
    - pSDB comparison and selection: the various pSDB indices for each satellite were compared to determine the most faultless for subsequent analysis.
    - Predicted depth derivation: predicted depths were derived using the selected pSDB indices.
3. **Validation:**
    - Spatial comparison of in-situ and pSDB values: in-situ depth measurements were spatially joined with corresponding pSDB values to facilitate comparison.
    - Validation of predicted depths: the predicted depths were compared to the in-situ data to evaluate accuracy.
    - Comparison of satellite platforms: the results were compared across the different satellite platforms to assess their relative performance.

- Usage and evaluation of ML techniques: the efficacy of ML techniques used was evaluated.

3. Study area

The Maltese archipelago (Figure 3.1) occupies a strategic position in the central Mediterranean, influencing regional marine dynamics. Positioned roughly 90 km south of Sicily (Italy) and 345 km north of the African coast, the islands are located within the WGS 1984 UTM Zone 33N coordinates of 35°48' to 36°05' N and 14° 11' to 14° 34' E (Schembri, 1993). The archipelago consists of three main islands: Malta (245.7 km²), Gozo (67.1 km²) and Comino (2.8 km²) (along with several smaller uninhabited islets, including Cominotto, Filfla, St. Paul's Islands and Fungus Rock). These islands are primarily composed of limestone and their coastlines are largely made up of steep cliffs punctuated by various bays, inlets and secluded coves (Said & Schembri, 2010).

The North and South Comino Channels, 1 km and 2 km wide respectively, separate Gozo from Comino and Comino from Malta. The archipelago is situated on the shallow Malta-Ragusa Rise, a submarine ridge connecting Sicily and North Africa. This shallow shelf (<90m) contrasts with the deep waters (>1000m) to the west (Schembri, 1993). The coastline (≈190 km) is varied, featuring rocky cliffs, sheltered bays and sandy beaches, particularly on Gozo. The region experiences a Mediterranean climate, characterized by hot, arid summers and mild, wet winters. While westerly winds are most common, ocean swells can approach from any direction. Tidal variations are minimal, with a maximum range of roughly 40 cm.

Understanding how rainfall and temperature are distributed in Malta is essential to analyze the local climate. To do this, two maps were created: one showing the average annual rainfall and the other showing the average annual temperature, both using data collected between 1970 and 2000 by WorldClim 2.1. Figure 3.2 reveals how much rain falls in Malta and the surrounding Mediterranean areas each year, on average. We can observe that Malta does not receive much rain, with amounts varying from 0 mm to 380 mm per year. This lack of rain is typical of the Mediterranean climate, where summers are dry and winters are mild. Figure 3.3 shows the average annual temperature in Malta and the central Mediterranean region. It is observed that Malta has high temperatures, with annual averages above 17.5 °C, which is also characteristic of the Mediterranean climate.

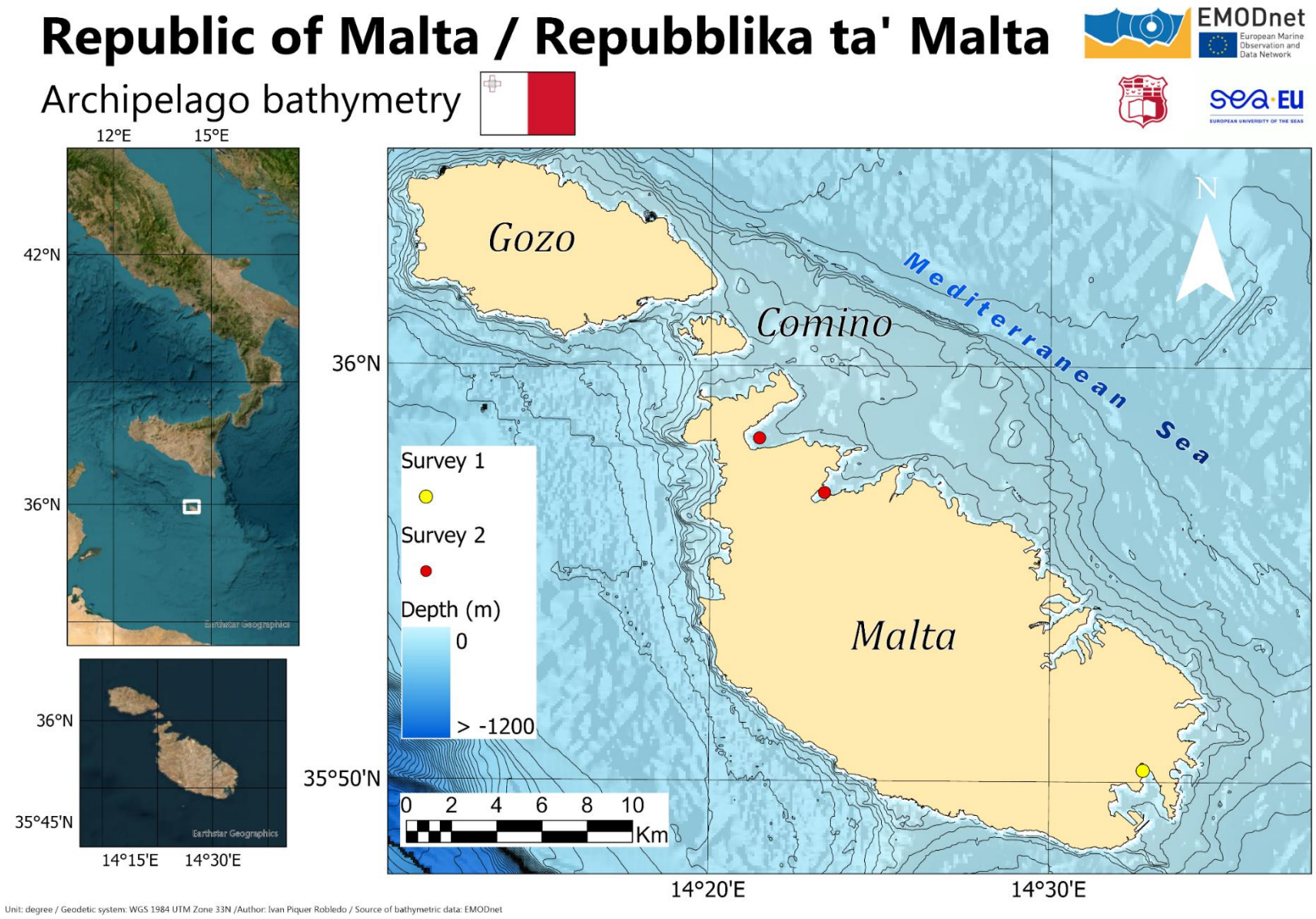

Figure 3.1 - Maltese archipelago and its bathymetry and surveys

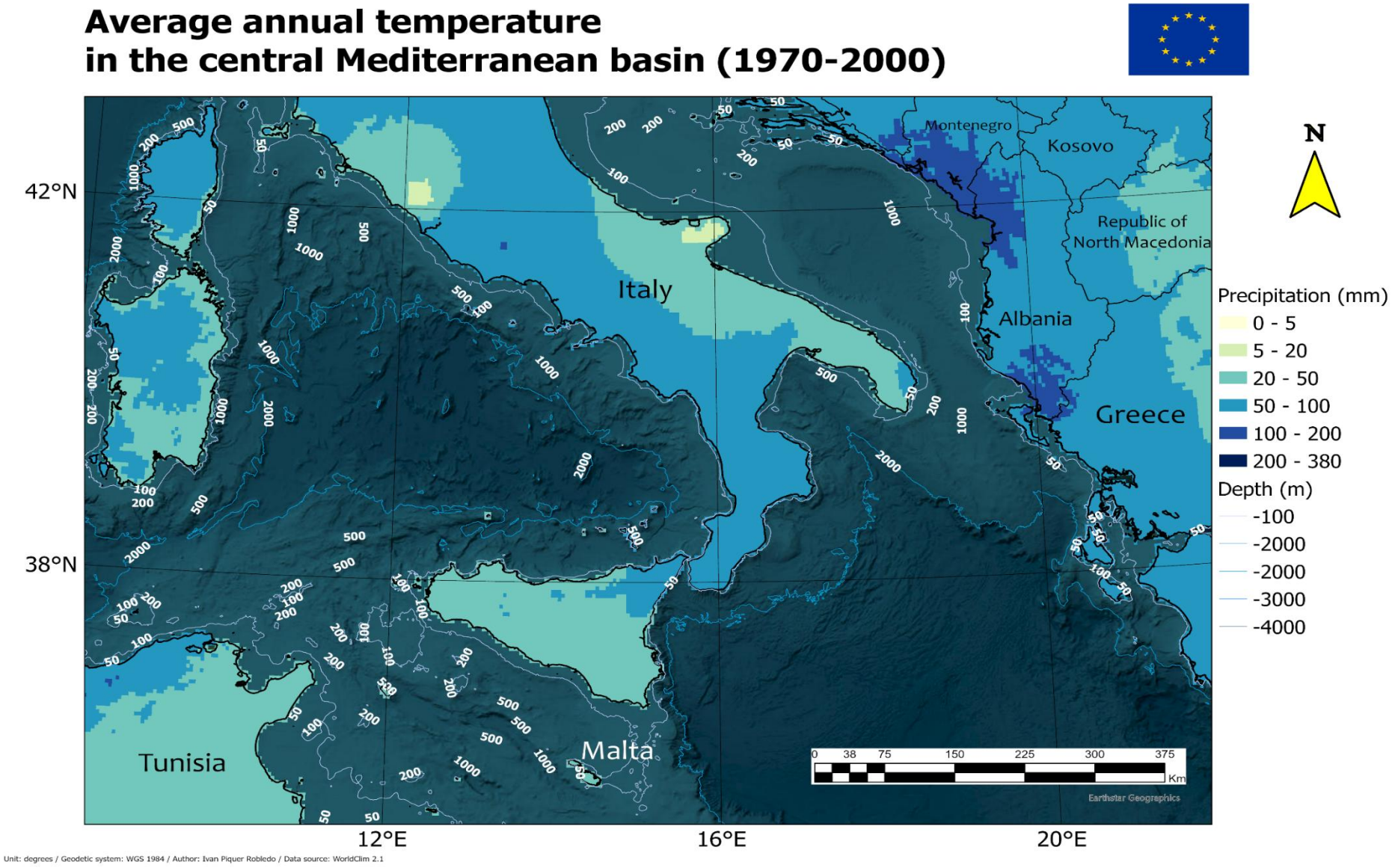

Figure 3.2 - Average annual precipitation in the central Mediterranean basin (1970-2000)

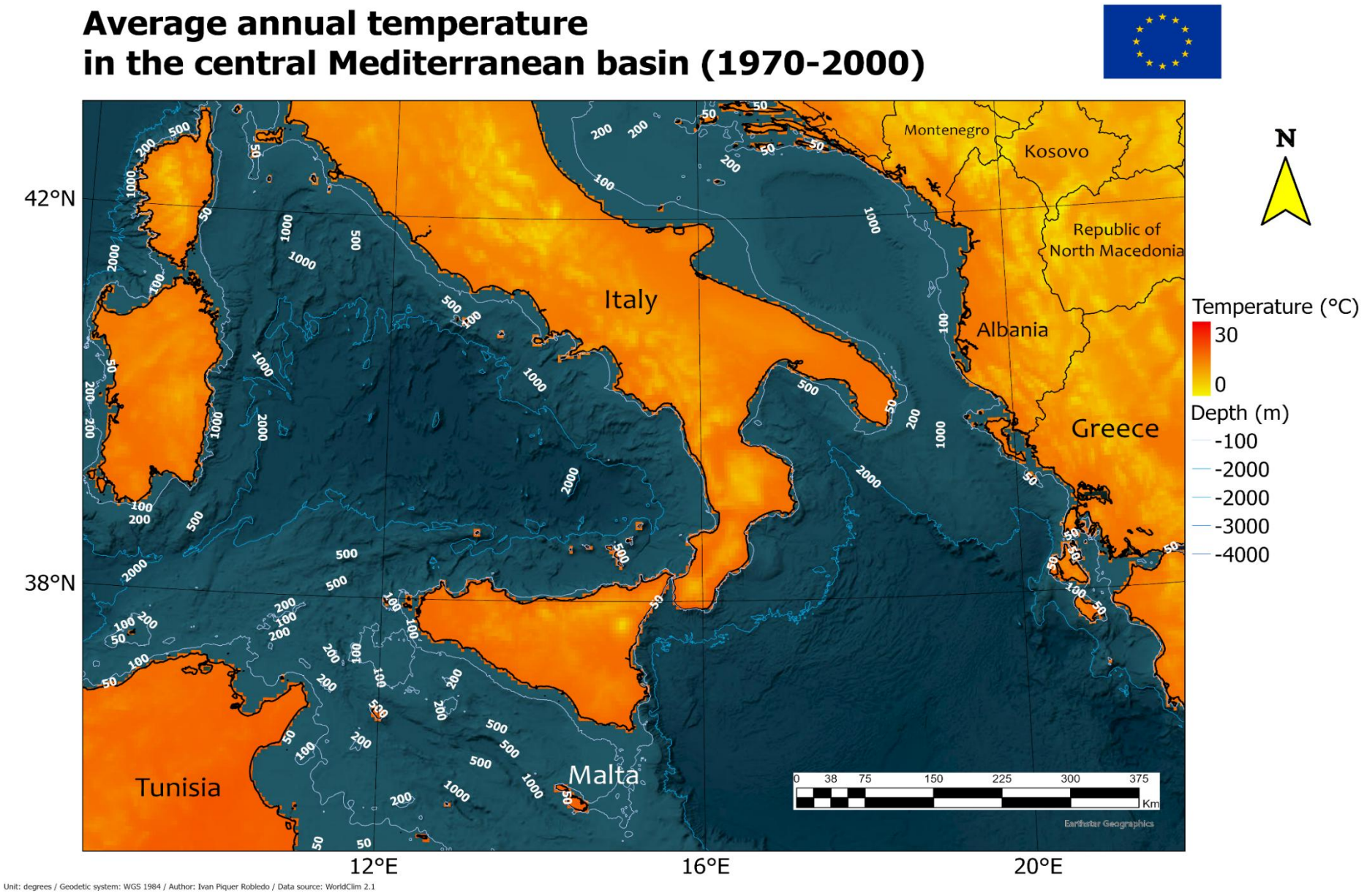

Figure 3.3 - Average annual temperature in the central Mediterranean basin (1970-2000)

The study comprises two surveys encompassing three distinct coastal locations around Malta. “Survey One” focused on Marsaxlokk Bay (4.48 km²) and “Survey Two”, included St. Paul’s Bay (11.84 km²) and Ghadira Bay (7.84 km²). The combined area covered by “Survey Two” was 19.68 km² and the total area surveyed across both surveys was 24.16 km². Data from “Survey One” was used to generate three bathymetric representations depicting predicted depth values derived from pSDB calculations by combining various satellite bands. These very versions were then evaluated using “Survey Two” raster data acquired by using a Voxometer on June 19, 2024, comparing their performance and obtaining error margin. Simultaneously, ML algorithms were employed in an empirical workflow to generate more rigorous predicted depth values and comparisons:

I. **Survey One - Marsaxlokk Bay** (Figure 3.4): situated at the southernmost point of the Maltese coastline (35°49’ N, 14°31’ E). The bay exhibits a complex geomorphology characterized by promontories, cliffs and sandy shorelines, indicative of a coastal system shaped by both erosional and depositional processes. As the second largest natural harbor of the Maltese archipelago, Marsaxlokk Bay served as the primary site for integrating the previous in-situ depth measurements collected with pSDB values from the three satellite platforms. The dataset of in-situ depth samples was compiled into a shapefile consisting of discrete point measurements.

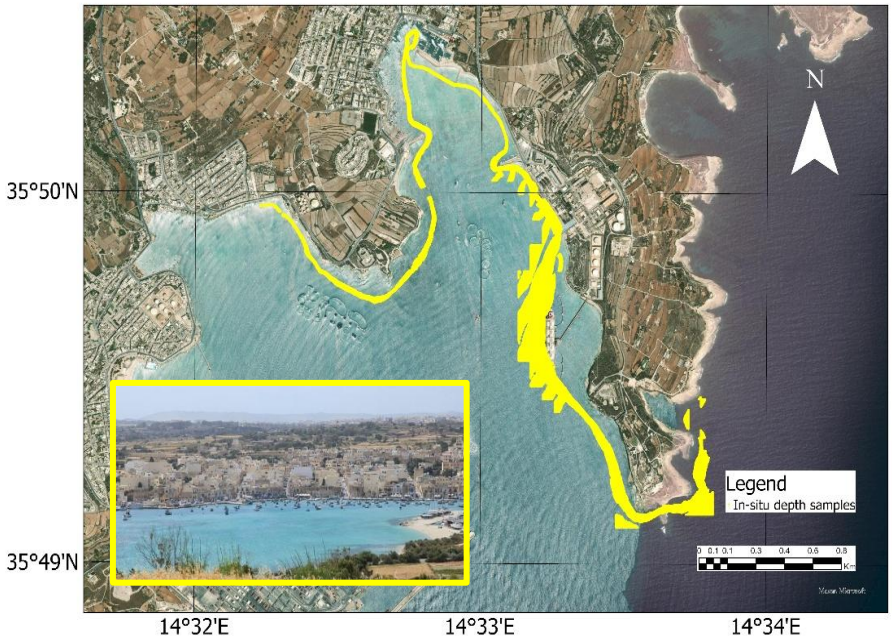

	OBJECTID *	Shape *	Easting	Northing	Longitude	Latitude	Depth
1	1	Point Z	458192.75	3965490.25	14.53711	35.832688	-0.5
2	2	Point Z	458192.75	3965490.75	14.53711	35.832693	-0.49
3	3	Point Z	458192.75	3965491.25	14.53711	35.832697	-0.45
4	4	Point Z	458192.75	3965491.75	14.53711	35.832702	-0.44
5	5	Point Z	458192.75	3965492.25	14.53711	35.832706	-0.39
6	6	Point Z	458192.75	3965492.75	14.53711	35.832711	-0.38

Figure 3.4 - Marsaxlokk Bay (Survey One) (top) and showing overlaid in-situ depth measurement points with their attributes table sample (bottom)

II. **Survey Two - St. Paul Bay and Ghadira Bay** (Figure 3.5):

- **St. Paul Bay**, located on the northeastern coast of Malta (35°56’ N, 14°24’ E), is a large, sheltered bay renowned for its scenic beauty and historical significance. It offers a mix of rocky shores and sandy beaches, reflecting varying degrees of exposure to wave action and other marine forces. The bay is dotted with small islands, including St. Paul’s Island.

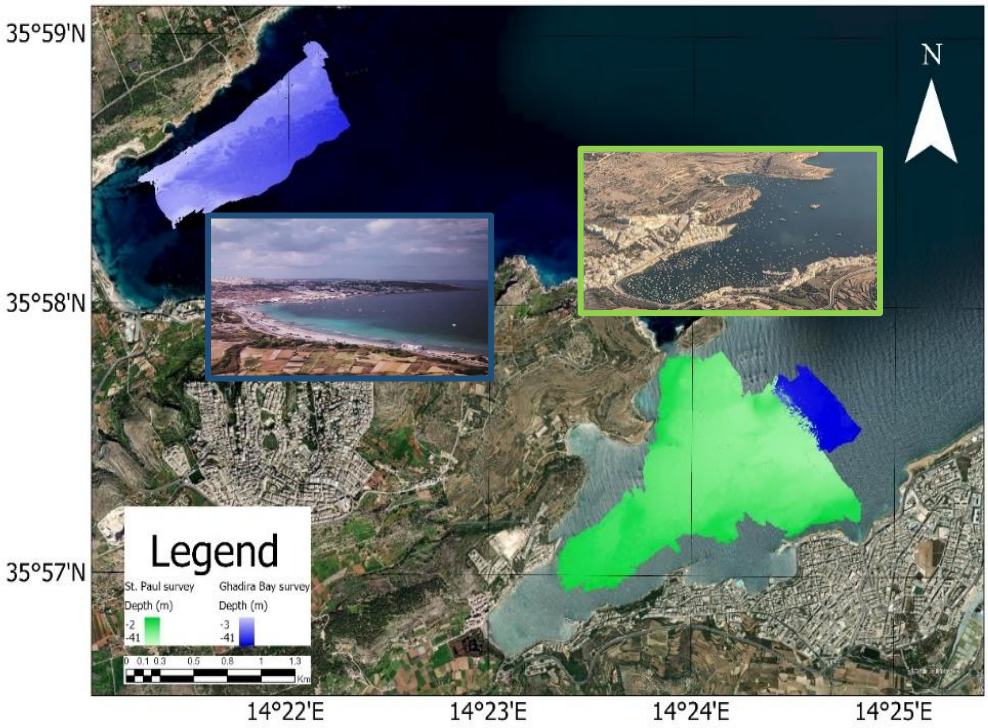

Figure 3.5 - St. Paul Bay (green) and Ghadira Bay (blue) (Survey Two) showing overlaid raster depth measurement grids

- **Ghadira Bay (or Mellieħa Bay)**, found in the northern part of the island (35°58’ N, 14°21’ E), near the village of Mellieħa, is the largest sandy beach in Malta and one of the most popular. It is renowned for its extensive sandy shores, suggesting a predominantly depositional environment and a relatively sheltered location.

4. Methodology

4.1 Satellite data

Within the framework of this research, data from three primary satellite were utilized: Landsat 9 (USGS), Planet Scope (Planet Labs) and Sentinel 2-A (ESA). These data sources were chosen due to their accessibility, the precision of their spectral measurements and their frequency of data acquisition, all of which are essential for accurately predicted water depth, denoted as pSDB.

To determine bathymetric depths from satellite imagery, intensity values from six spectral bands were extracted at each in-situ vector point. Employing the non-linear band ratio method (Stumpf *et al.*, 2003), depth values were subsequently calculated. This computational approach is predicated on the principle of exponential light attenuation, wherein the reflectance of two spectral bands diminishes as water depth increases (Amrari *et al.* 2021). It is noteworthy that bands with shorter wavelengths experience reduced attenuation compared to those with longer wavelengths, leading to an increase in the band ratio with depth (Vargas *et al.*, 2021). The pSDB was then calculated using Equation 1:

$$\mathrm{pSDB} = \frac{\ln\left(\mathrm{nRw}(\lambda_i)\right)}{\ln\left(\mathrm{nRw}(\lambda_j)\right)} \qquad \text{(Equation 1)}$$

where nRw(λi) and nRw(λj) are the water reflectance values for two distinct spectral bands, λi and λj, respectively. The natural logarithm (ln) is employed in the pSDB calculation to linearize the relationship between the band ratio and water depth. This transformation is predicated

on the principle of exponential light attenuation, wherein the ratio of water reflectances (nRw) diminishes exponentially with increasing depth. Thus, ln(nRw(λi)/nRw(λj)) provides a linear approximation of the depth-dependent attenuation.

Additionally, this approach mitigates the influence of substrate albedo, enhancing the accuracy of bathymetric data (Jawak *et al.*, 2015). While variations in bottom albedo affect both band ratios, the ratio remains more sensitive to depth variations than albedo fluctuations. Importantly, this research diverges from traditional methodologies, which typically rely on blue and green spectral bands. To optimize SDB techniques specifically for the Maltese Islands, four additional band ratios, including red and NIR wavelengths, were incorporated to identify the most productive spectral combinations for this geographic setting.

The pSDB index was calculated for each satellite data set using optimized combinations of band ratios. It was obtained by using the "Raster calculator" tool within ArcGIS Pro. This tool allowed for the pixel-by-pixel application of the band ratio formula across the satellite imagery, generating a pSDB raster layer for each dataset. The bands used in these combinations were:

- B02
- B03
- B04
- B05
- B08

The specific combinations used were for Landsat 9 (B02/B03, B02/B04, B02/B05), Sentinel 2-A (B02/B03, B02/B04, B02/B08) and Planet Scope (B01/B02) (Figure 4.1.1):

Satellite	Sensor	Band	Wavelength (nm)	Resolution (m)	Description
Landsat 9	OLI-2	B01	430-450	30	Coastal/Aerosol
Landsat 9	OLI-2	B02	450-515	30	Blue
Landsat 9	OLI-2	B03	535-600	30	Green
Landsat 9	OLI-2	B04	630-680	30	Red
Landsat 9	OLI-2	B05	845-885	30	Near Infrared (NIR)
Landsat 9	OLI-2	B06	1560-1660	30	Shortwave Infrared 1 (SWIR 1)
Landsat 9	OLI-2	B07	2100-2300	30	Shortwave Infrared 2 (SWIR 2)
Landsat 9	OLI-2	B08	500-680	15	Panchromatic
Landsat 9	OLI-2	B09	1360-1390	30	Cirrus
Landsat 9	TIRS 1	B10	10600-11190	100	Thermal Infrared 1 (TIR 1)
Landsat 9	TIRS 2	B11	11500-12510	100	Thermal Infrared 2 (TIR 2)
Planet Scope	PSB.SD	B01	465-515	3	Blue
Planet Scope	PSB.SD	B02	547-583	3	Green
Planet Scope	PSB.SD	B03	650-680	3	Red
Planet Scope	PSB.SD	B04	845-885	3	Near Infrared (NIR)
Sentinel 2-A	MSI	B01	443	60	Coastal Aerosol
Sentinel 2-A	MSI	B02	490	10	Blue
Sentinel 2-A	MSI	B03	560	10	Green
Sentinel 2-A	MSI	B04	665	10	Red
Sentinel 2-A	MSI	B05	705	20	Red Edge 1
Sentinel 2-A	MSI	B06	740	20	Red Edge 2
Sentinel 2-A	MSI	B07	783	20	Red Edge 3
Sentinel 2-A	MSI	B08	842	10	Near Infrared (NIR)
Sentinel 2-A	MSI	B8A	865	20	Narrow Near Infrared (NIR)
Sentinel 2-A	MSI	B09	945	60	Water Vapor
Sentinel 2-A	MSI	B10	1375	60	Cirrus
Sentinel 2-A	MSI	B11	1610	20	Shortwave Infrared (SWIR 1)
Sentinel 2-A	MSI	B12	2190	20	Shortwave Infrared (SWIR 2)

Figure 4.1.1 - Landsat 9, Planet Scope and Sentinel 2-A spectral bands. The ones highlighted in yellow were used in this study

I. **Landsat 9 (USGS)**: The selected bands were B02, B03, B04 and B05:

- pSDB_B02B03: The combination of the B02 and B03 bands is essential for estimating pSDB in clear waters. Figure 4.1.2 shows Landsat 9 pSDB_B02B03:

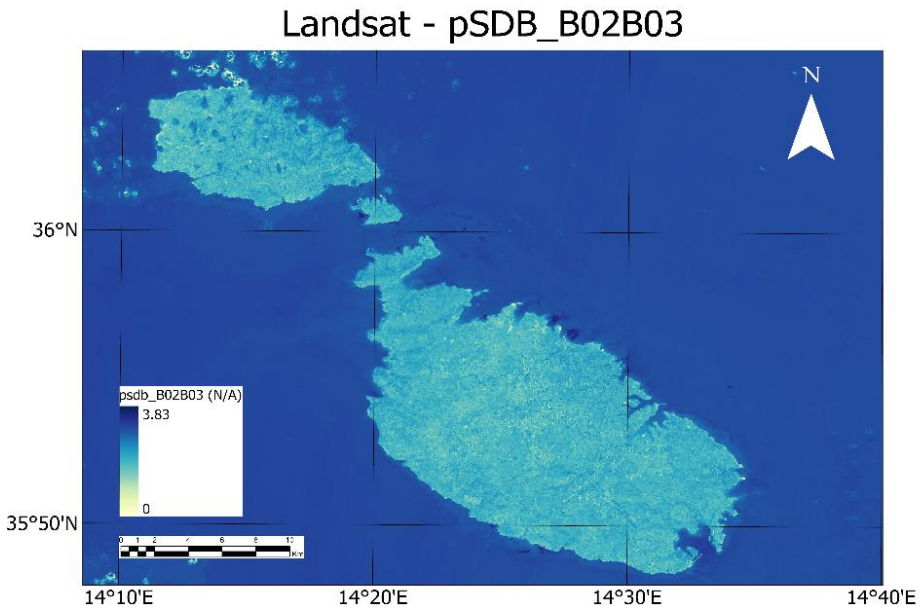

Figure 4.1.2 - Landsat 9 pSDB_B02B03

- pSDB_B02B04: the ratio of the B02 and B04 bands is used to enhance sensitivity to depth in waters with higher sediments or dissolved organic matter content. The red band, although with less penetration, provides information about surface reflectance and light absorption by these components. Figure 4.1.3 shows Landsat 9 pSDB_B02B04:

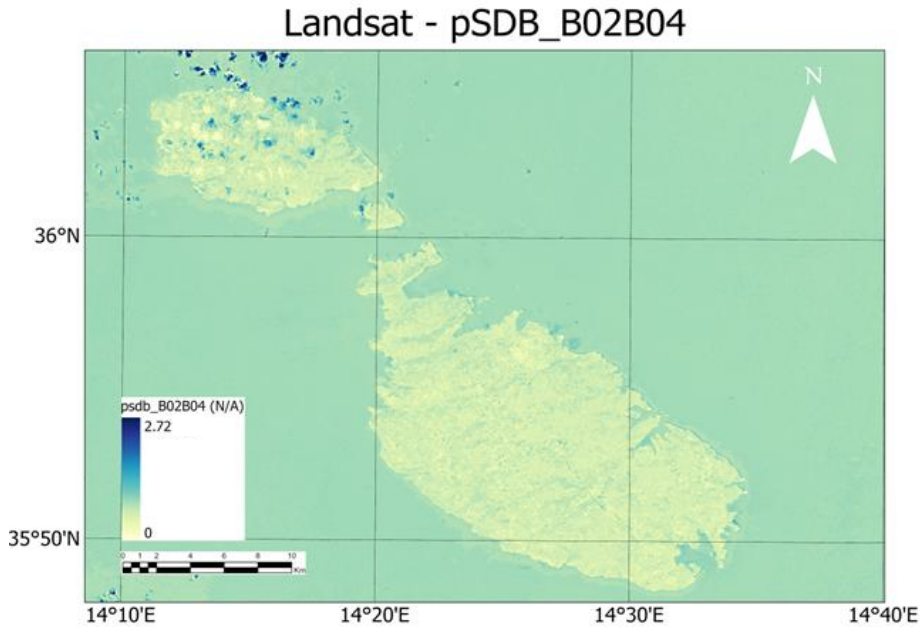

Figure 4.1.3 - Landsat 9 pSDB_B02B04

- pSDB_B02B05: the fraction of the B02 and B05 bands allows for discrimination between shallow water and land, as NIR is strongly absorbed by water. This combination is useful for delineating coastlines and correcting for the effects of emergent vegetation. Figure 4.1.4 shows Landsat 9 pSDB_B02B05:

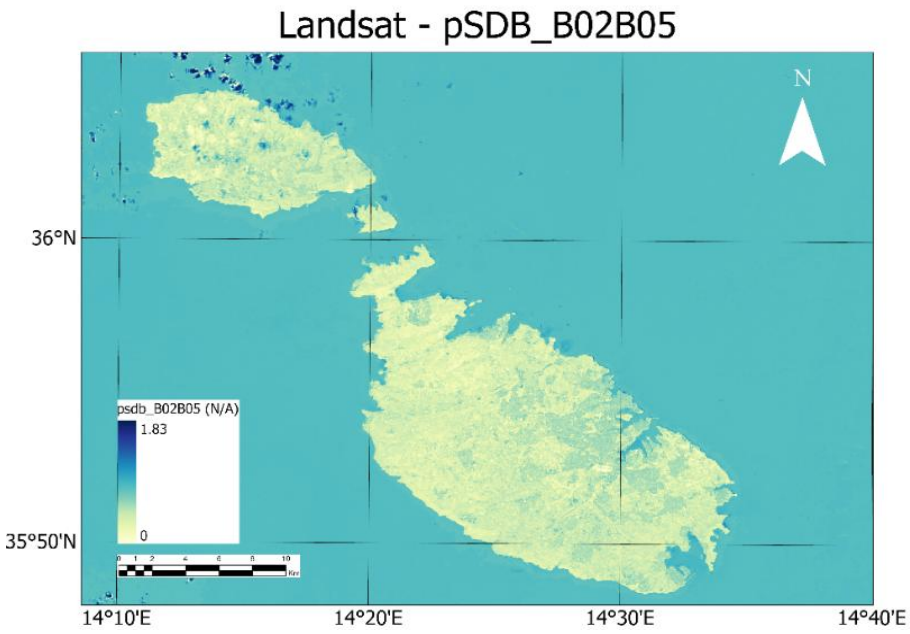

Figure 4.1.4 - Landsat 9 pSDB_B02B05

II. **Planet Scope (Planet Labs)**: the selected bands were B01 and B02:

- pSDB_B01B02: like Landsat 9, mixing B01 and B02 bands in Planet Scope is used for estimating pSDB's in clear waters. Planet Scope high spatial resolution enables more enhanced precision in detecting small-scale depth variations. Figure 4.1.5 shows Planet Scope pSDB_B01B02:

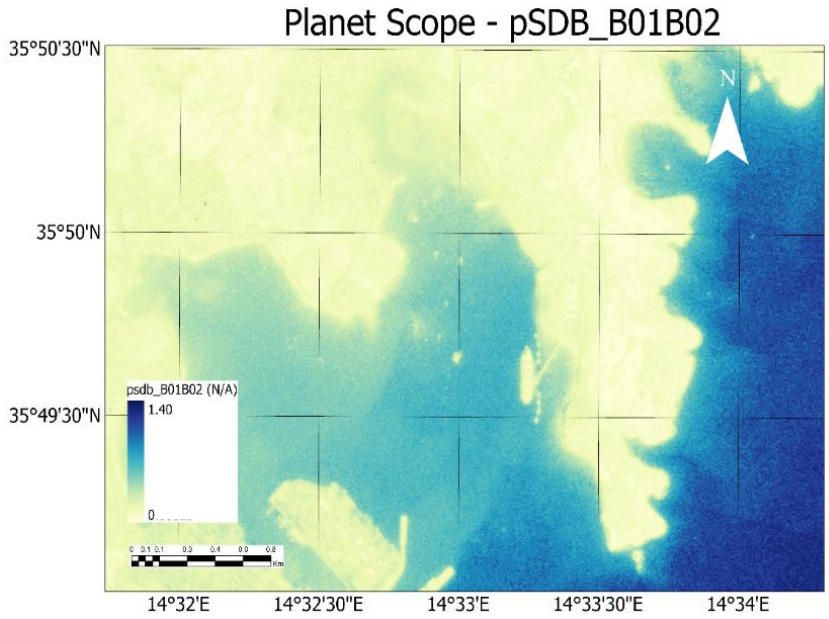

Figure 4.1.5 - Planet Scope pSDB_B01B02

III. **Sentinel 2-A (ESA)**: the selected bands were B02, B03, B04 and B08:

- pSDB_B02B03: as with Landsat 9 and Planet Scope, the combination of B02 and B03 bands is essential for estimating pSDB in clear waters. Figure 4.1.6 shows Sentinel 2-A pSDB_B02B03:

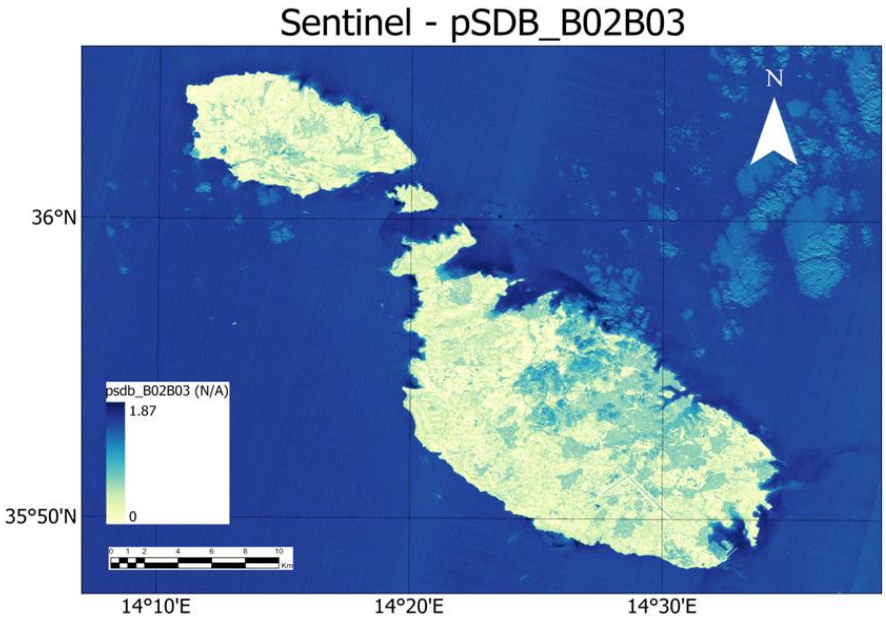

Figure 4.1.6 - Sentinel 2-A pSDB_B02B03

- pSDB_B02B04: the combination of B02 and B04 bands is used to improve pSDB estimation in waters with higher turbidity or sediment content. Figure 4.1.7 shows Sentinel 2-A pSDB_B02B04:

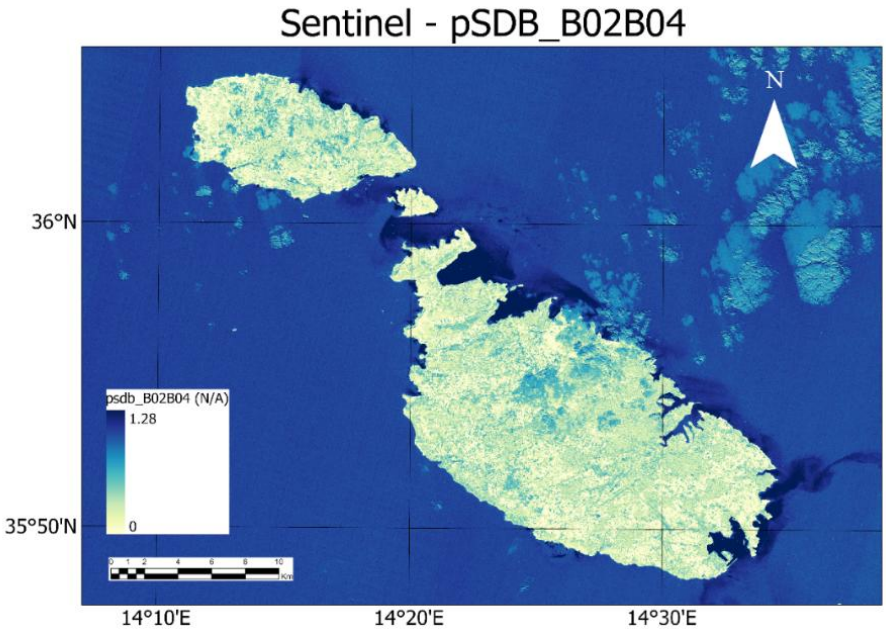

Figure 4.1.7 - Sentinel 2-A pSDB_B02B04

- pSDB_B02B08: the combination of the B02 and B08 bands allows for better discrimination between shallow water and land, as well as correction for atmospheric effects and the presence of vegetation. Figure 4.1.8 shows Sentinel 2-A pSDB_B02B08:

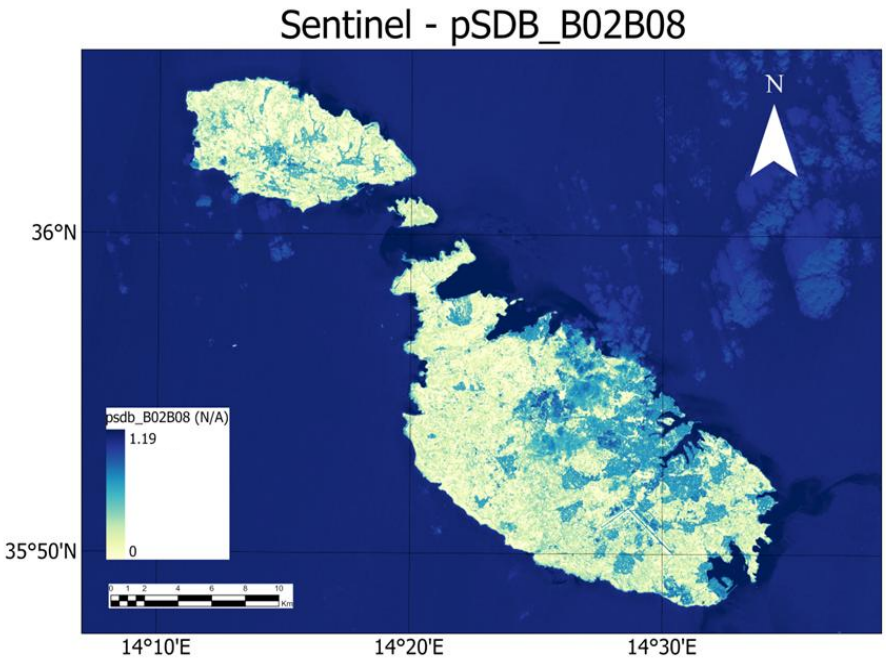

Figure 4.1.8 - Sentinel 2-A pSDB_B02B08

The relationship between the pSDB and the SDB was defined by the following empirical ratio model (Stumpf *et al.,* 2003) expressed in Equation 2:

$$SDB = m1 \cdot pSDB - m0 \qquad \text{(Equation 2)}$$

The coefficients m1 and m0 in the calculation were determined by calibrating the satellite-derived data with in-situ depth measurements. This calibration process ensured that the SDB values sharply represent the actual depths in the waters surrounding the Maltese Islands.

4.2 Survey One

Once the different pSDB values were obtained, a "Points to Raster" conversion process was carried out for each satellite used in this study according to each resolution (Figure 4.2.1). This was done to generate a spatially coherent representation of actual depth, based on in-situ measurements taken directly in the field. These measurements, known as "in-situ depth samples," will provide an accurate reference for adjusting the results derived from satellite data.

The "Points to Raster" process transforms point-based depth measurements into a continuous surface, where each pixel represents an interpolated mean depth value derived from nearby measurement points. The spatial resolution of the generated raster was specifically adjusted for each satellite, considering the characteristics and native resolution of its sensors. The resulting rasters will enable meaningful comparisons between field-measured depths and depth estimates derived from satellite images later.

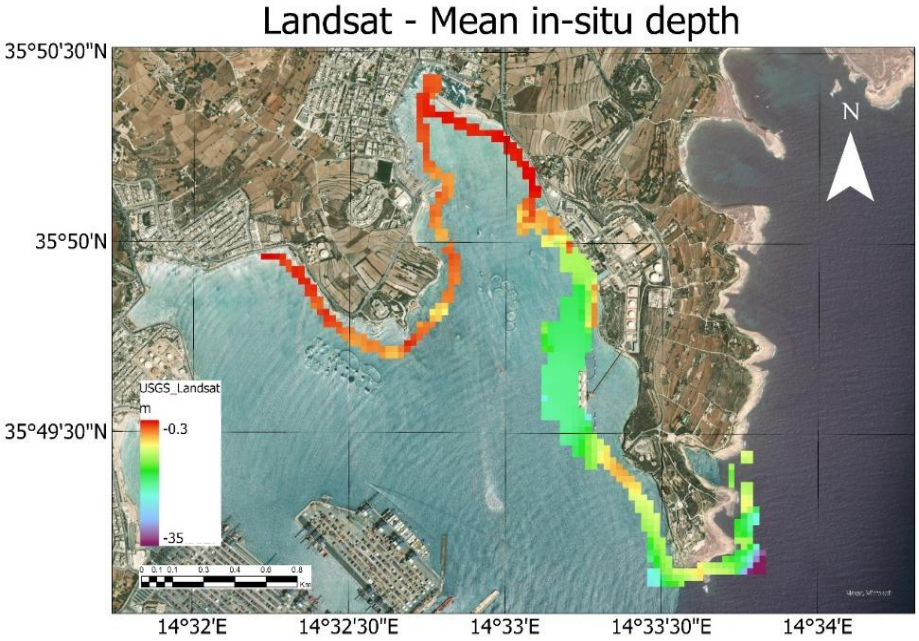

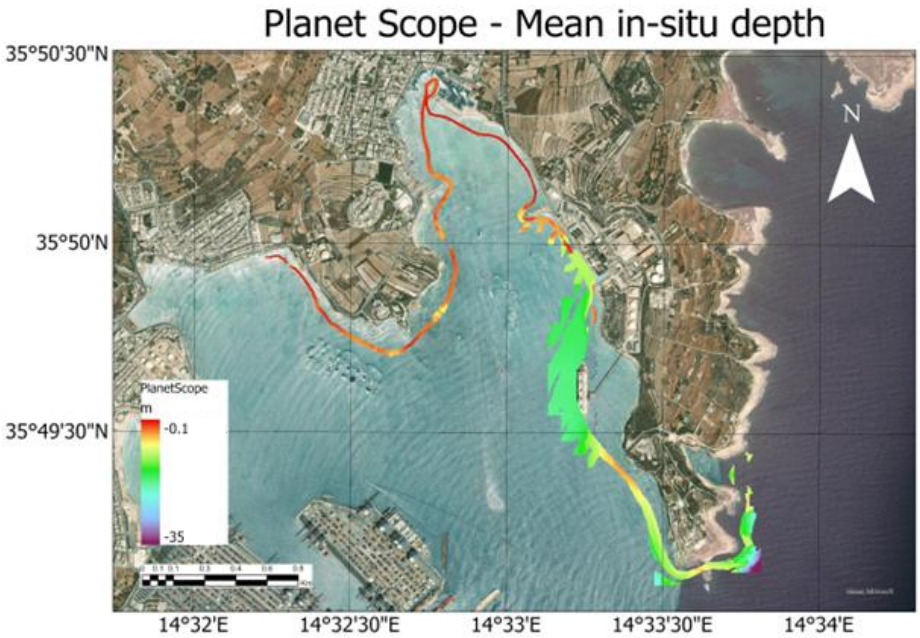

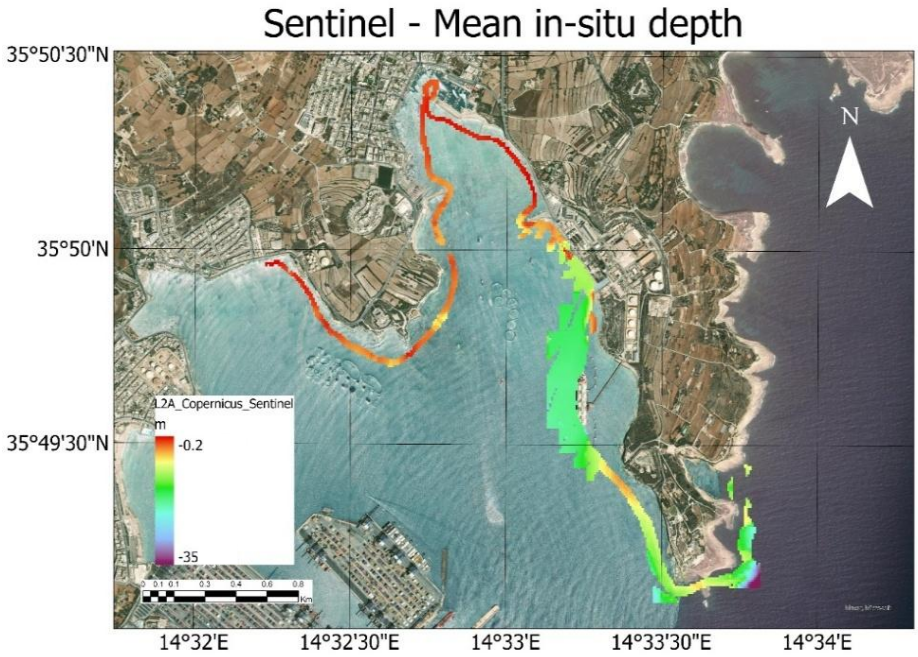

Figure 4.2.1 - "Points to raster" conversions from in-situ depth samples

Once the 3 rasters were generated, a "Raster to Points" tool was carried out to extract the centroids of each raster cell and assign them the corresponding mean depth value (Figure 4.2.2). This transformation is essential to convert the depth information, which is initially presented as a continuous surface, into a set of discrete points with depth attributes. Each resulting point was assigned to the mean depth value of the original pixel, providing a point representation of the depth with a spatial accuracy determined by the raster resolution. Additionally, a specific tool was employed to add the X and Y coordinates to each point, which allowed for precise georeferencing of the cell centroids and facilitated subsequent spatial analyses. This set of points, with their respective mean depths and geographic coordinates, will facilitate direct joining with pSDB data.

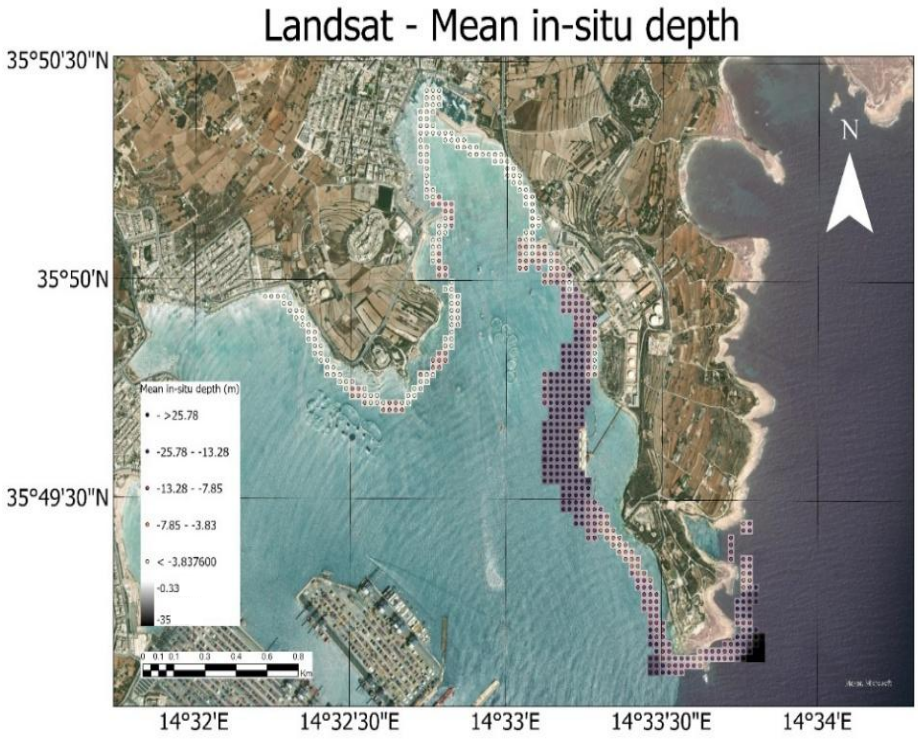

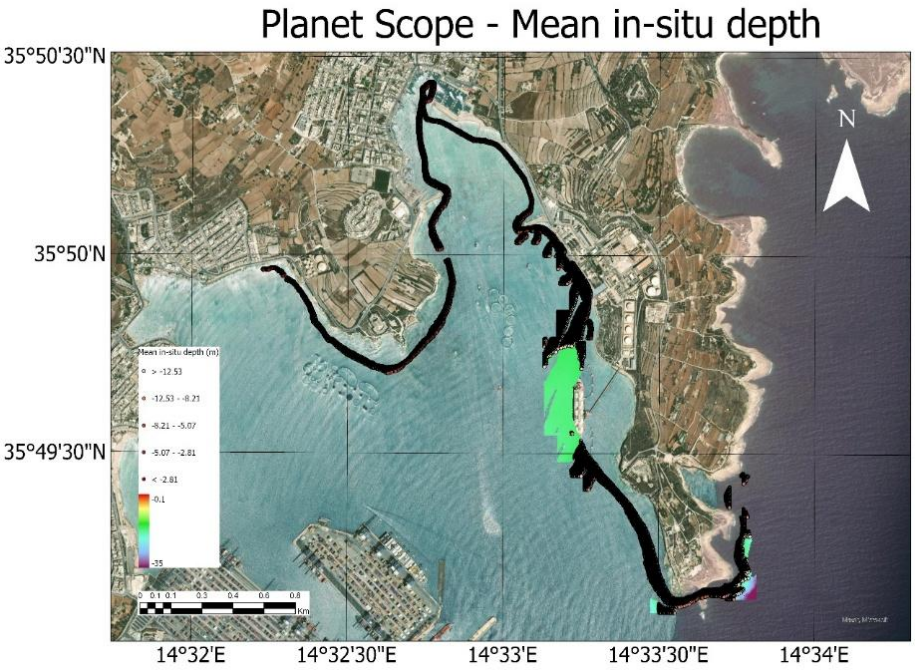

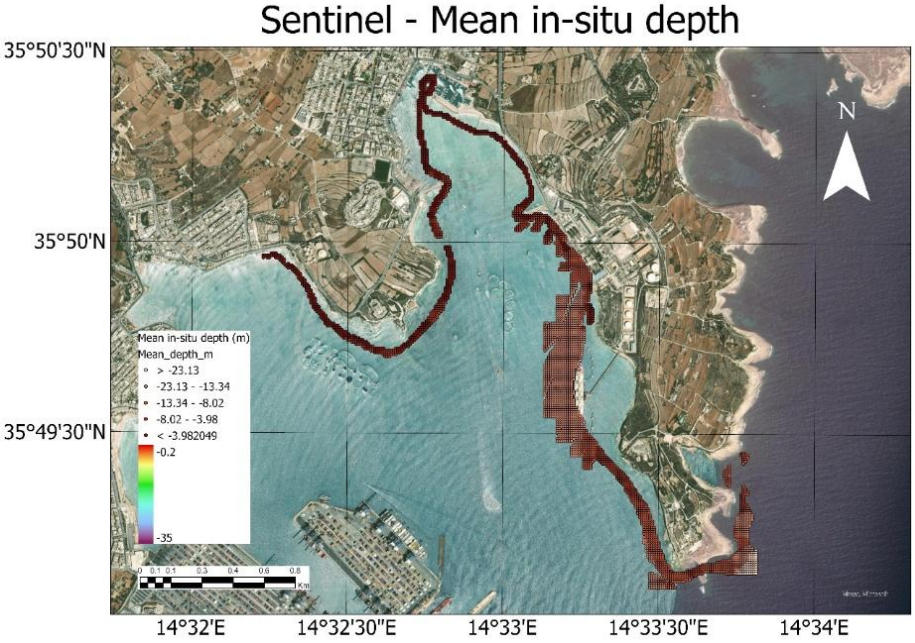

Figure 4.2.2 - "Raster to points" conversions from mean in-situ depth rasters

The application of the "Raster to points" tool resulted in the generation of 579 datasets that yielded elements for Landsat 9. The Planet Scope dataset produced 29,919 elements and the Sentinel 2-A dataset resulted in 3,398 elements. These variations in the number of elements reflect the differences in spatial resolution and coverage of the respective satellite sensors.

Following the generation of point features representing the mean in-situ depths, an important step was undertaken to integrate these field-derived measurements with the corresponding pSDB values calculated and extracted from the satellite imagery. This integration was achieved through the utilization of the "Extract values to points" tool. This geoprocessing tool facilitated the precise extraction of pSDB coefficients from each satellite's respective raster layer at the exact spatial locations corresponding to the in-situ depth measurement points as we can see on Table 4.2.1:

Table 4.2.1 - Landsat 9 (top), Planet Scope (center) and Sentinel-2A (bottom) attribute table samples

OBJECTID *	Easting	Northing	Shape *	Mean_Depth (m)	pSDB_B02B03
1	458970	3966360	Point	-2.49	0.99
2	459000	3966360	Point	-2.57	0.99
3	459030	3966360	Point	-2.67	0.98
4	458970	3966330	Point	-2.46	0.99
5	459000	3966330	Point	-2.58	0.99
6	459030	3966330	Point	-2.63	0.98
…	…	…	…	…	…

OBJECTID *	Easting	Northing	Shape *	Mean_Depth_m	pSDB_B01B02
1	460552	3963961	Point	-34.15	1.25
2	460537	3963961	Point	-33.46	1.24
3	460555	3963949	Point	-34.19	1.24
4	460549	3963961	Point	-33.94	1.24
5	460573	3963949	Point	-34.66	1.24
6	460552	3963973	Point	-34.15	1.24
…	…	…	…	…	…

OBJECTID *	Easting	Northing	Shape *	Mean_depth_m	pSDB_B02B03
1	458985	3966365	Point	-2.38	0.99
2	458995	3966365	Point	-2.49	0.99
3	459005	3966365	Point	-2.61	0.99
4	459015	3966365	Point	-2.63	1.00
5	459025	3966365	Point	-2.63	0.99
6	458975	3966355	Point	-2.45	0.99
…	…	…	…	…	…

As a result, each point was attributed with two key parameters, being the mean in-situ depth and the corresponding pSDB derived from the satellite imagery for that same location. To facilitate further analysis, the attribute tables associated with these point sets were exported to Comma Separated Values (CSV) format. In Microsoft Excel, the CSV files were imported and outliers were removed. Once this was done, scatter plots were made to visualize the relationship between pSDB coefficients (explanatory variable (x axis)) and mean in-situ depths (response variable (y axis)). For these linear regressions, a significance level of 95% ($\alpha = 0.05$) was established. This exploratory analysis allowed identifying patterns and trends in the data, as well as assessing the suitability of different band combinations for depth estimation.

To further analyze the accuracy of depth estimates, an evaluation of the prediction error in relation to the corrected depth was performed for each satellite platform. This analysis was conducted using the R Gui 4.4.2 programming language, which allows for detailed statistical and visual evaluation of regression models.

4.3 Survey Two

To evaluate the empirical ratio form for SDB using the derived regression models, a new satellite image was selected for each platform, acquired proximal to the in-situ depth measurements of “Survey Two” conducted on June 19, 2024. Specifically, the Sentinel 2-A image was acquired on September 28, 2024, the Landsat 9 image on August 29, 2024 and the Planet Scope image on June 19, 2024. Image selection prioritized temporal proximity and atmospheric similarity to minimize extraneous changeability. Subsequently, pSDB_B02B03 indices were computed for Landsat 9 and Sentinel 2-A and pSDB_B01B02 for Planet Scope.

Utilizing the previously established platform-specific regression equations, predicted depth maps were generated at the pixel level for each image using “Raster calculator” tool (Figure 4.3.1).

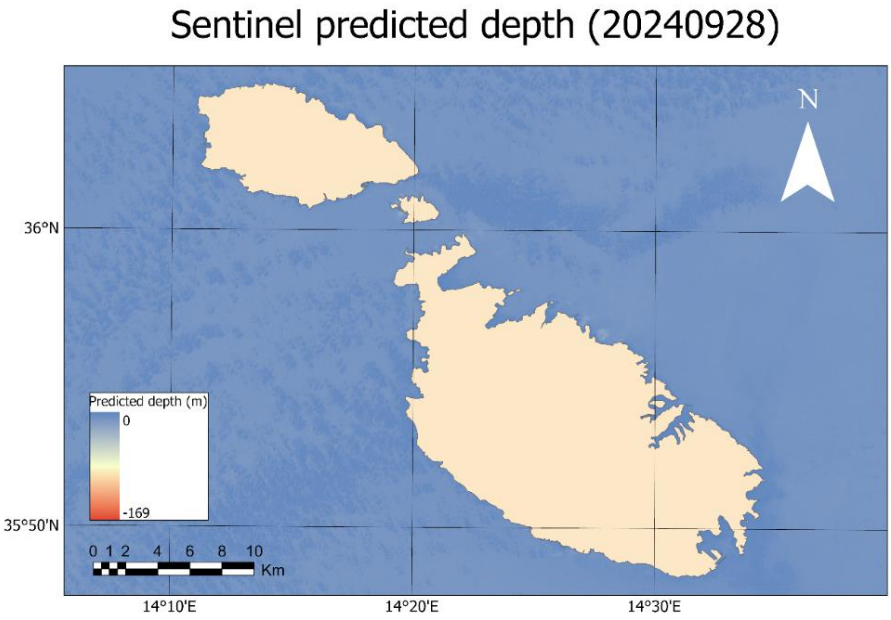

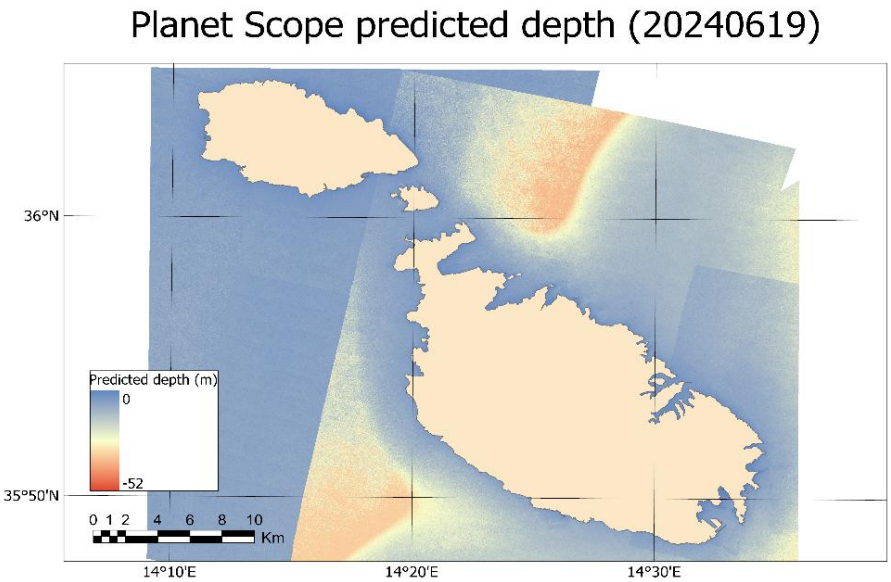

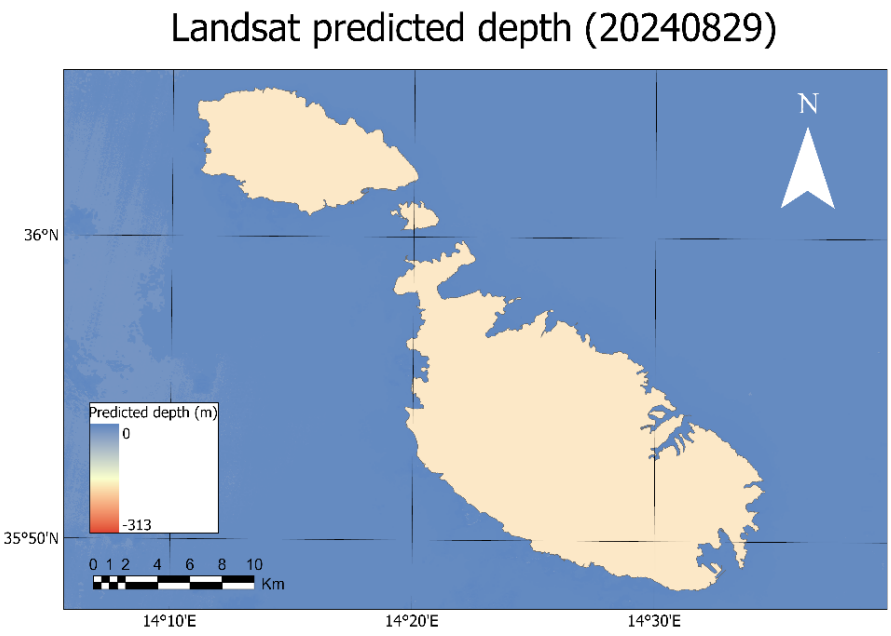

Figure 4.3.1 – Predicted depth for Sentinel 2-A (top), Planet Scope (center) and Landsat 9 (bottom) using raster calculator

For Sentinel 2-A and Landsat 9, the predicted depth maps were generated using the following formulas presented in Equation 3:

$$\mathrm{SDB} = 186.63 \cdot \mathrm{pSDB}_{\mathrm{Sentinel}} - 183.91 \qquad (\textit{If pSDB is less or equal to 1.0075})$$

$$\mathrm{SDB} = 643.8 \cdot \mathrm{pSDB}_{\mathrm{Sentinel}} - 641.45 \qquad (\textit{If pSDB is greater than 1.0075})$$

(Equation 3)

$$\mathrm{SDB} = 294.04 \cdot \mathrm{pSDB}_{\mathrm{Landsat}} - 289.96 \qquad (\textit{If pSDB is less or equal to 1.0075})$$

$$\mathrm{SDB} = 1693.1 \cdot \mathrm{pSDB}_{\mathrm{Landsat}} - 1688.1 \qquad (\textit{If pSDB is greater than 1.0075})$$

4.4 Conventional and machine learning regression techniques

Beyond traditional regression techniques, this study explored the feasibility of applying ML methods for the SDB estimation. A training set was constructed from the original digital numerical band values and calculated band ratios. In-situ depth measurements taken in Ghadira Bay and St. Paul Bay served as target values for model building. To evaluate the ML simulations, 6 specific data tables in CSV format were generated for each satellite platform and each bay. These tables served as the basis for training and evaluating the regression models.

These tables were created using the "Extract multiple values to points" tool and processed in Microsoft Excel later. This tool allowed information to be extracted from satellite images and combined with in-situ depth measurements. Specifically, the following fields can be shown in Figure 4.4.1:

- **"Easting" and "northing"**: geographic coordinates of the measurement point.
- **"Blue", "green", "red" and "NIR"**: reflectance values of the spectral bands for each satellite.
- **"mean_depth_m"**: in-situ depth measurements, used as target values for the systems.
- **"psdb_B01B02_GIS"** (or "psdb_B02B03_GIS" for Landsat 9 and Sentinel 2-A): pSDB indices calculated from the new spectral bands.
- **"psdb_B01B02_Excel"** (or "psdb_B02B03_Excel" for Landsat 9 and Sentinel 2-A): pSDB indices calculated in Microsoft Excel, used for comparison with the values calculated in ArcGIS Pro.

Easting	Northing	Blue	Green	Red	NIR	Mean_depth_m	psdb_B02B03_GIS	psdb_B02B03_Excel
443018.5	3982232.5	7402	7724	7191	7180	-13.66	0.99	0.95
443048.5	3982232.5	7410	7713	7176	7182	-13.16	0.99	0.96
443078.5	3982232.5	7422	7699	7177	7174	-13.28	0.99	0.96
443108.5	3982232.5	7427	7694	7185	7166	-12.96	0.99	0.96

Figure 4.4.1 - example of the data table generated in ArcGIS Pro, in this case for Landsat 9

Regarding the assessment set for the ML method, satellite imagery was loaded along with a polygon delineating the Maltese coastline, around a 3 km buffer area. This limit was considered since the study was focused on shallow waters, between -25 and -30 m. This polygon was subsequently converted to raster format using the "Polygon to raster" tool, ensuring that the output resolution matched the native resolution of each satellite sensor. Furthermore, values were assigned to differentiate between land and water through the "Value field." It is worth mentioning that the "Reclassify" tool was used to invert the values of this coastal raster.

The next step was to mask the individual bands of each satellite image. To do this, the "Raster calculator" tool was used, applying the "SetNull" function. Using conditional expressions, the pixel values corresponding to land in each spectral band were set to "no data", generating rasters of masked bands. Finally, the composite rasters were created using the "Composite bands" tool, combining the masked bands of each satellite in the appropriate spectral order and naming the resulting composite rasters.

Each masked composite raster was converted to a point layer using the “Raster to point” tool and descriptive names were assigned to the resulting point layers. The geographic X and Y coordinates were then added to each point layer using the “Add XY Coordinates tool”. The crucial step in creating the training dataset was the use of the “Extract Multi Values to Points” tool. This tool extracted pixel values from the three masked composite rasters. Finally, the attribute table of the resulting point layer, containing the coordinates and reflectance values of the spectral bands, was exported to a CSV file, ensuring the inclusion of the necessary columns for subsequent modeling with ML algorithms.

After thorough data preparation and the generation of CSV files, the feasibility of the Random Forest (RF) algorithm, was explored for modeling the relationship between the predictor variables derived from satellite images and the target depth variable. RF (Figure 4.4.2) is a supervised learning algorithm that utilizes an ensemble of decision trees for predictive estimation. The methodology involves the generation of multiple decision trees, each trained on a bootstrapped sample of the original dataset. These samples are created through random sampling with replacement, ensuring that each tree is built on a slightly different subset of data. Besides, at each node within a tree, a random subset of features is considered for the optimal split, introducing additional diversity among the trees. The final prediction is obtained

by aggregating the predictions from all individual trees, typically through averaging for regression tasks or voting for classification tasks. This ensemble approach mitigates the risk of overfitting and enhances the simulation's generalization capabilities.

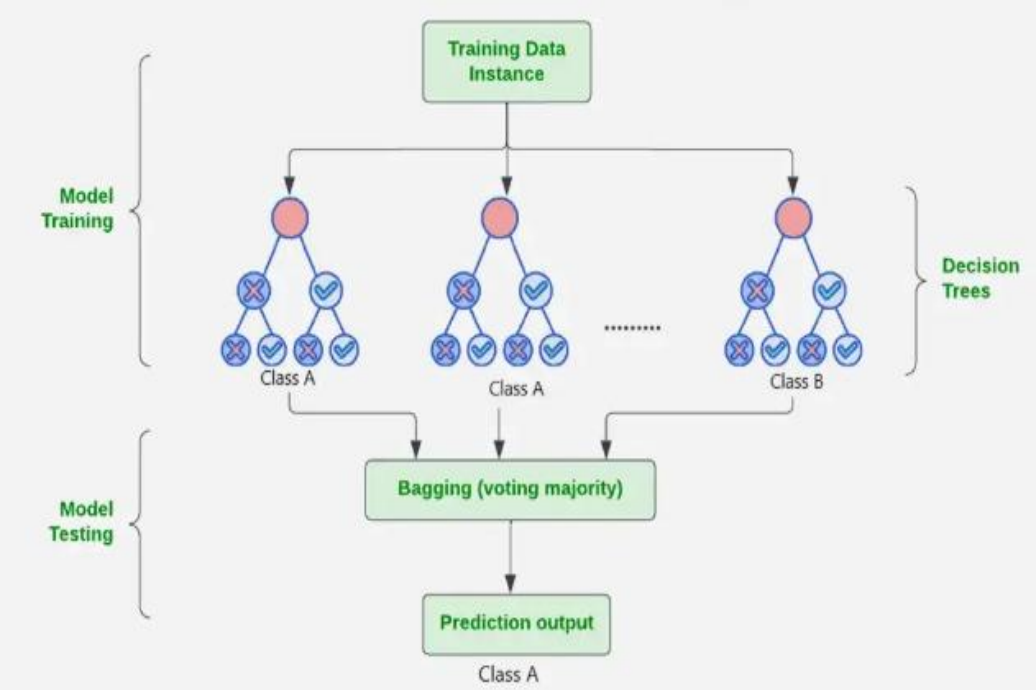

Figure 4.4.2 - RF explanation

The implementation of the RF algorithm necessitates the specification of two key parameters: the number of trees to be grown (N) and the number of features to be considered at each split (m). Initially, a training set was partitioned, with approximately two-thirds allocated for bootstrap sampling and the remaining one-third reserved for out-of-bag (OOB) error estimation. Each bootstrapped sample served as the training data for an individual decision tree, which is grown without pruning. At each node, the selection of the best feature for splitting is confined to a randomly chosen subset of m predictors. Unlike traditional linear models, RFs possess the capacity to structure complex, non-linear relationships between variables and can accommodate both numerical and categorical data types. Consequently, RFs offer a more flexible and clear-cut modeling framework compared to conventional empirical or semi-empirical approaches, enabling the development of robust predictive versions based on existing datasets.

To carry out the RF modeling, a training set was constructed from the digital numerical values of the original bands and the calculated band ratios. In-situ mean depth calculations calculated in Ghadira Bay and St. Paul Bay served as target values for building the representations. RF algorithm was applied to independent datasets corresponding to the selected satellite images. Specifically, Landsat 9 images from August 29, 2024, Sentinel 2-A from September 28, 2024 and Planet Scope from June 19, 2024, were used. The performance of the trained RF simulations was evaluated using metrics such as Root Mean Square Error (RMSE), Correlation Coefficient and Coefficient of Determination (R^2). The six generated CSV files, corresponding to each satellite platform and each study bay, were processed using the Python programming language in the Visual Studio Code development environment. *Pandas* libraries were used for the manipulation and analysis of tabular data and the *Scikit-learn* library, a leading ML library in Python, was used for the implementation of the RF algorithm and the model evaluation tasks.

Specifically, for each CSV file, the columns containing the reflectance values of the spectral bands ("Blue," "Green," "Red," "NIR") were defined as the predictor feature set. The column storing the in-situ mean depth measurements ("mean_depth_m") was set as the target variable that the schema was to learn to predict. To ensure a rigorous evaluation of the models' performance, the data were randomly split into training and test sets. Additionally, a feature scaling process was applied to the predictor variables in both sets using the *Scikit-learn StandardScaler* class, standardizing the data to have a mean of zero and a standard deviation of one, which is beneficial for many ML algorithms. The trained *StandardScaler* objects for each dataset were saved for later use in normalizing new data, including those intended for prediction across the entire Malta study area.

Subsequently, for each scaled training dataset, a *RandomForestRegressor* model from the *Scikit-learn* library was instantiated. These versions were trained using the fit method, learning the complex nonlinear relationship between spectral reflectances and depth. Although not detailed in the excerpt provided, a common practice in the development of ML simulations is the optimization of model hyperparameters (such as the number of trees in the forest, maximum tree depth, etc.) using techniques such as grid search or random search, with the aim of maximizing predictive performance. Once trained, the models were evaluated using the scaled test set and the correlation coefficient between predicted and actual depths was

used as the primary metric to quantify the model's ability to estimate shallow bathymetry. The trained RF algorithms, along with their corresponding scalers, were finally serialized and saved for later application in the generation of depth prediction rasters for the entire region of interest.

5. Results

5.1 Conventional regression method

Initially, conventional regression techniques were applied to estimate water depth from satellite data. These techniques, as mentioned in section 4, were based on linear relationships between spectral bands and in-situ measured depth. They provided first estimations of SDB:

I. **Landsat 9**: an initial attempt to establish a relationship between pSDB_B02B03 and in-situ depth measurements ($y = 960.32x - 952.14$ (R^2 = 0.74 – p-value ≈ 0)) revealed a non-linear trend across the depth range (Figure 5.1.1). Upon visual inspection of the scatter plot, a potential breakpoint was identified around 4.99 m, suggesting that the relationship between pSDB_B02B03 and depth might exhibit different linear trends in shallower and deeper waters. This hypothesis was based on the understanding that water optical properties and light attenuation can vary with depth. Accordingly, the Landsat 9 dataset was split into two subsets: one containing in-situ depths from 0 to 4.99 m and the other containing depths of 5 m and above. A linear regression analysis was then performed separately for each subset. The results, shown in Figure 5.1.2, demonstrated two distinct linear trends, with separate regression lines and equations for each subset. Specifically, the regression for depths from 0 to 4.99 m yielded the formula $y = 294.04x - 289.96$ (R^2 = 0.8 and p-value ≈ 0), while the regression for depths of 5 m and greater yielded the equation $y = 1693.1x - 1688.1$ (R^2 = 0.8 and p-value ≈ 0). The p-values obtained are extremely low, indicating that the models are below the chosen significance level. Moreover, the coefficients of determination for both subsets suggest a good fit of the predictors to the data.

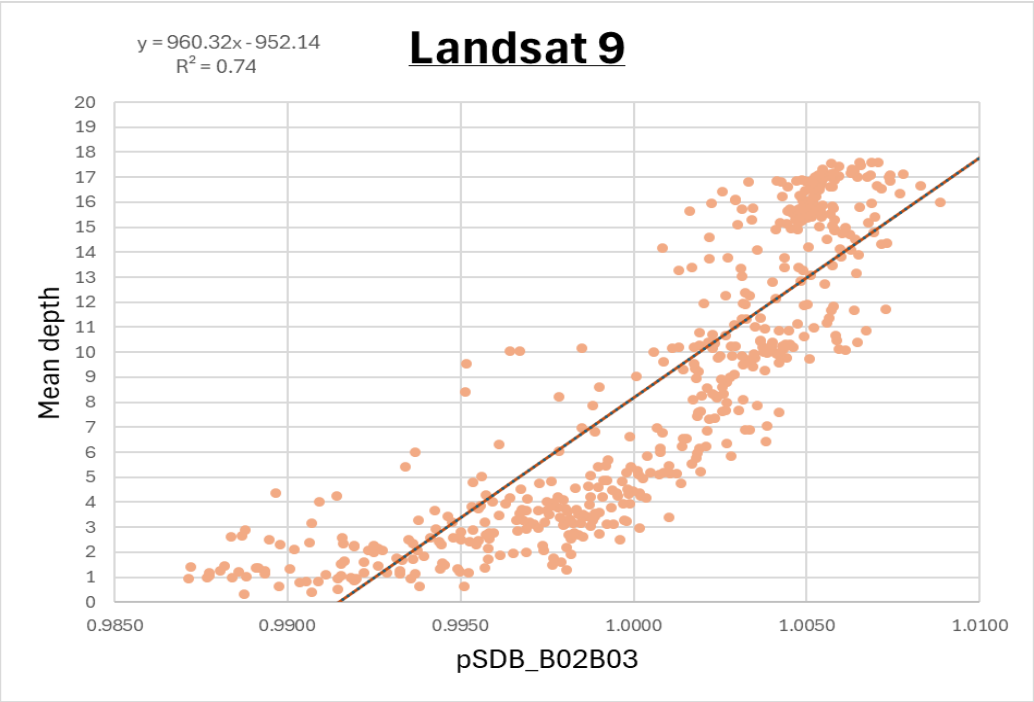

Figure 5.1.1 - Initial relationship between pSDB_B02B03 and mean depth for Landsat 9, showing a non-linear trend

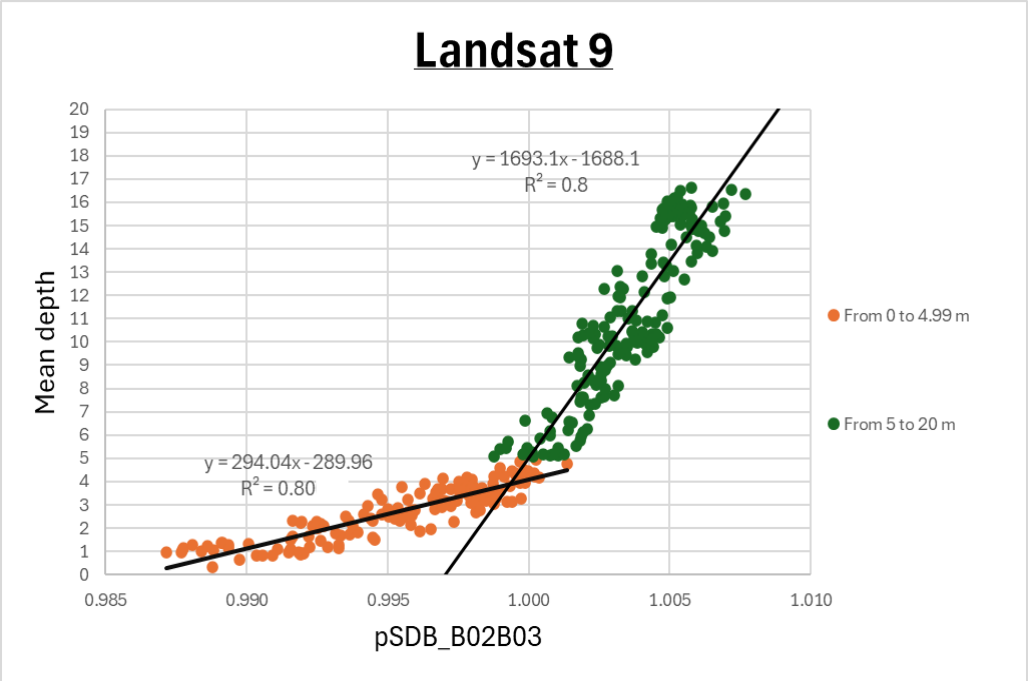

Figure 5.1.2 - Segmented linear regression of Landsat 9 showing separate linear trends: from 0 to 4.99 m and from 5 to 20 m

II. **Planet Scope**: its data revealed a strong positive relationship between the pSDB_B01B02 index and the in-situ depth measurements, as Figure 5.1.3 shows. The linear regression performed yielded the formula $y = 115.91x - 113.7$ with a R^2= 0.8 and p-value ≈ 0.00, indicating that the linear model explains a notable percentage of the volatility in depth. Visual inspection of the scatter plot confirms the presence of a clear and consistent linear trend throughout the studied depth range.

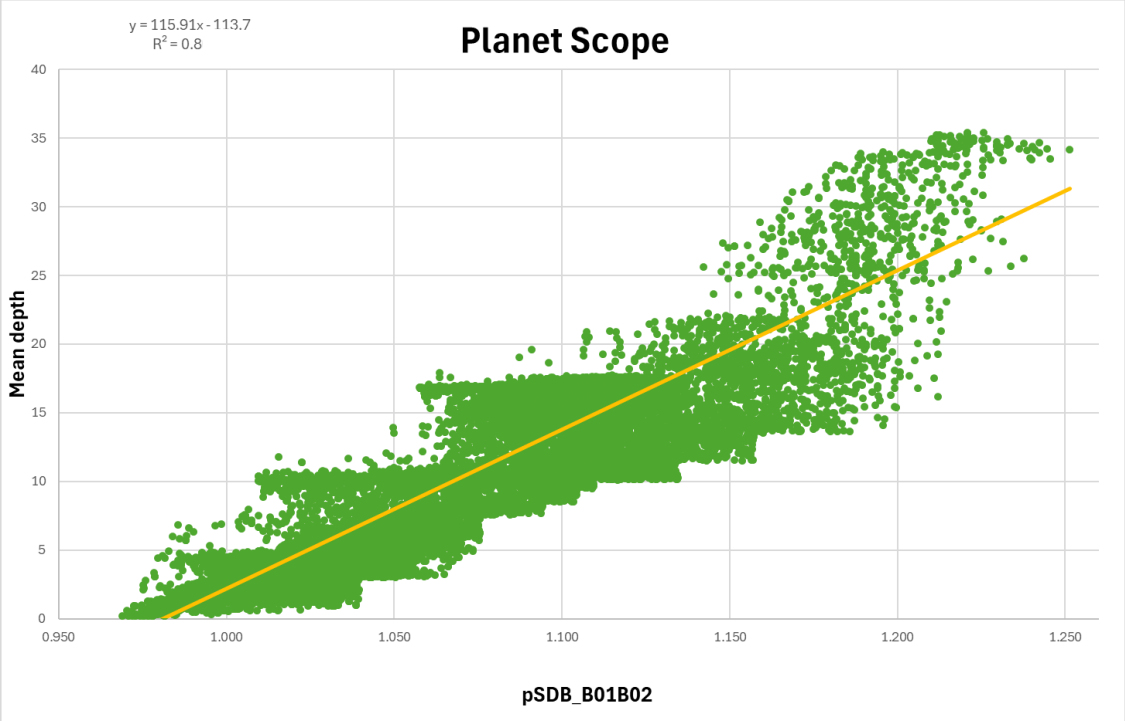

Figure 5.1.3 - Relationship between pSDB_B01B02 and mean depth for Planet Scope, showing a linear trend

III. **Sentinel 2-A:** it shows a strong overall linear relationship between the pSDB_B02B03 index and mean depth, with an equation of $y = 555.06x - 551.78$ (R^2 = 0.83 and p-value ≈ 0.00) (Figure 5.1.4). Nevertheless, its distribution of points suggests a potential difference in trend between shallower and deeper waters. Following a similar approach to that used with the Landsat 9 data, a potential inflection point was identified around 4.99 m too, obtaining two subsets: one containing in-situ mean depths from 0 to 4.99 m and the other containing depths of 5 m and above. A linear regression analysis was performed separately for each subset, as Figure 5.1.5 demonstrates. Specifically, the regression for depths from 0 to 4.99 m yielded the

formula $y = 186.63x - 183.91$ (R^2 = 0.8 and p-value ≈ 0.00), while the regression for depths of 5 m and above yielded the equation $y = 643.8x - 641.45$ (R^2 = 0.8 and p-value ≈ 0.00). These results suggest that the pSDB_B02B03 index may be a more accurate predictor of depth when separate linear models are applied for different depth ranges. The obtained p-values are extremely low, indicating that both systems met the criterion for statistical significance. This, together with the high coefficients of determination for both subsets, suggests that the linear models fit the data well and explain a substantial proportion of the observed oscillation in mean depth.

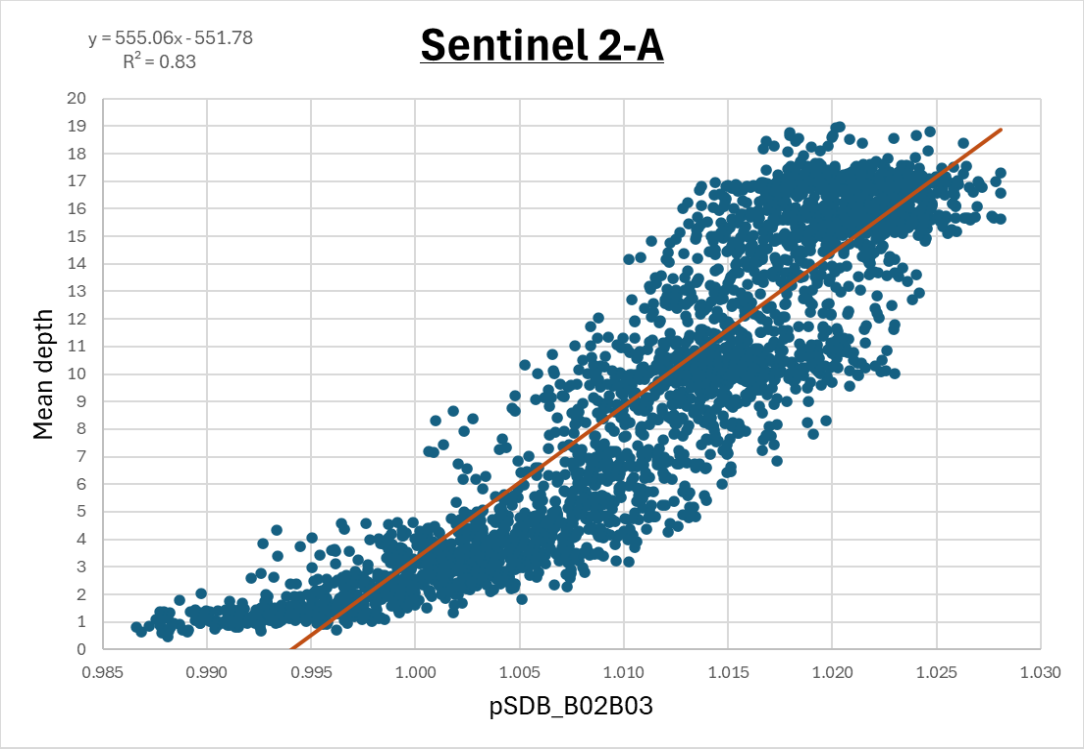

Figure 5.1.4 - Initial relationship between pSDB_B02B03 and mean depth for Sentinel 2-A, showing a non-linear trend

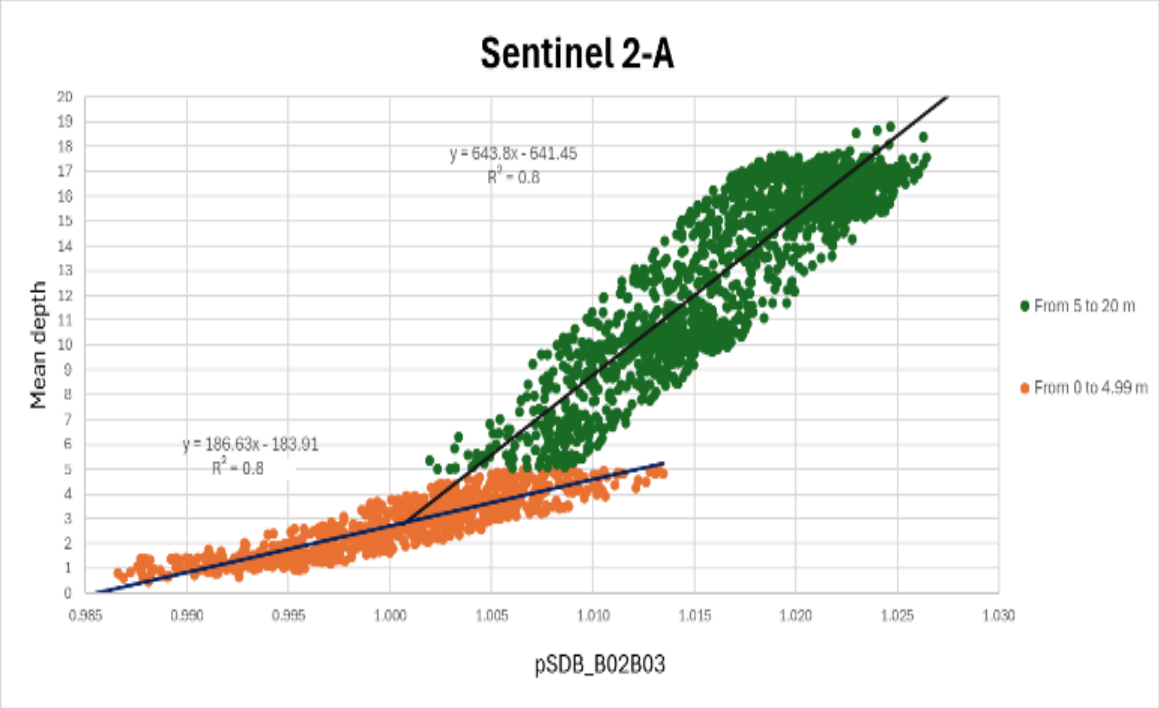

Figure 5.1.5 - Segmented linear regression of Sentinel 2-A showing separate linear trends: from 0 to 4.99 m and from 5 to 20 m

Besides the relationship between pSDB's and mean depth, a combined linear regression version was fitted to assess the overall relationship between corrected depth and error for Ghadira Bay and St. Paul Bay on R Gui 4.4.2 software. To further understand the distribution and magnitude of errors (residuals) between actual and predicted depths in "Survey Two" bays, visualizations were generated by using ArcGIS Pro:

- Ghadira Bay (Figure 5.1.6):

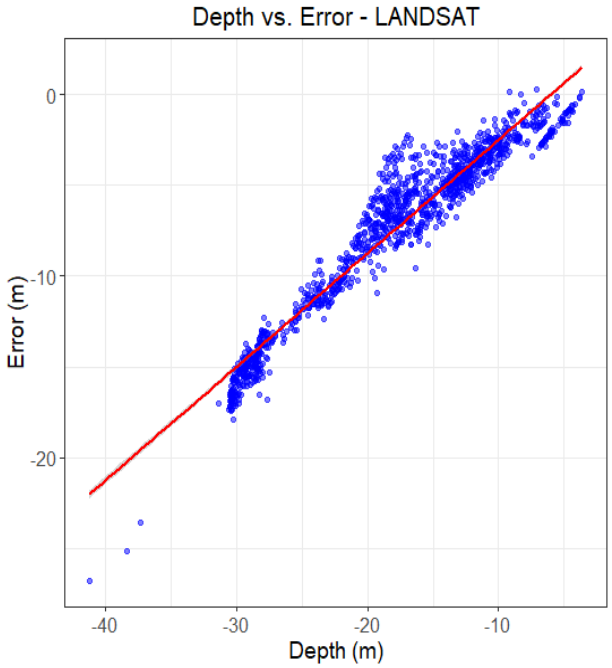

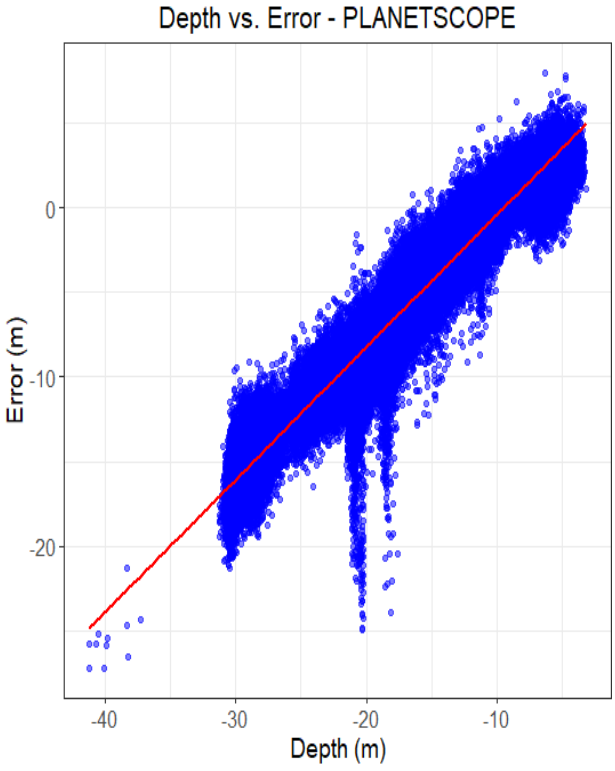

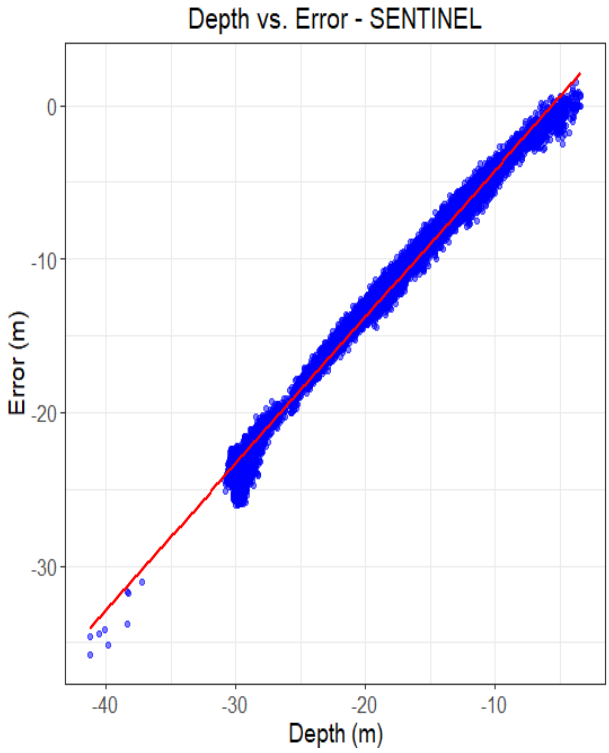

Figure 5.1.6 - Scatter plots of the relationship between depth and error for Landsat 9 (top), Planet Scope (center) and Sentinel 2-A (bottom) at Ghadira Bay

The linear regression presented 120,241 total samples, where the response variable is "Error - Mean depth m corrected". The intercept of 7.22, with a standard error of 0.01 and a p-value ≈ 0, indicates that when the pSDB_B01B02 index is zero, the corrected mean depth is 7.22 m, this value being statistically validated. The slope of the system was -0.79, with a standard error of 0.00085 and a p-value ≈ 0, suggesting that for each unit increase in the pSDB_B01B02 index, the corrected mean depth increases by 0.79 m, also statistically improbable under the null hypothesis. The framework presented an adjusted R^2 of 0.9, explaining 90% of the change in the corrected mean depth. The F statistic of 886,200 (p-value ≈ 0), the RMSE of 2.04 and the Mean Absolute Error (MAE) of 1.46 indicate that the model is statistically consistent and has a good fit to the data. The residuals range from -16.72 to 7.65, with a median of 0.33. Ten-fold cross-validation was used to ensure the robustness of the system and the intercept parameter was true.

I. Landsat 9: a positive correlation was observed between depth and error, with a relatively uniform dispersion around the line of best fit. Figure 5.1.7 visualizes the difference between the mean actual depth and the predicted depth obtained by linear

regression in Ghadira Bay. Dark blue values represent areas where the system overestimates depth, while yellow values indicate underestimation or minor differences. The dominance of dark blue in central zones highlights a clear overestimation trend. The histogram displays the distribution of residuals, showing a left-skewed pattern with a mean residual of -14.93 m, confirming the consistency to overpredict depth.

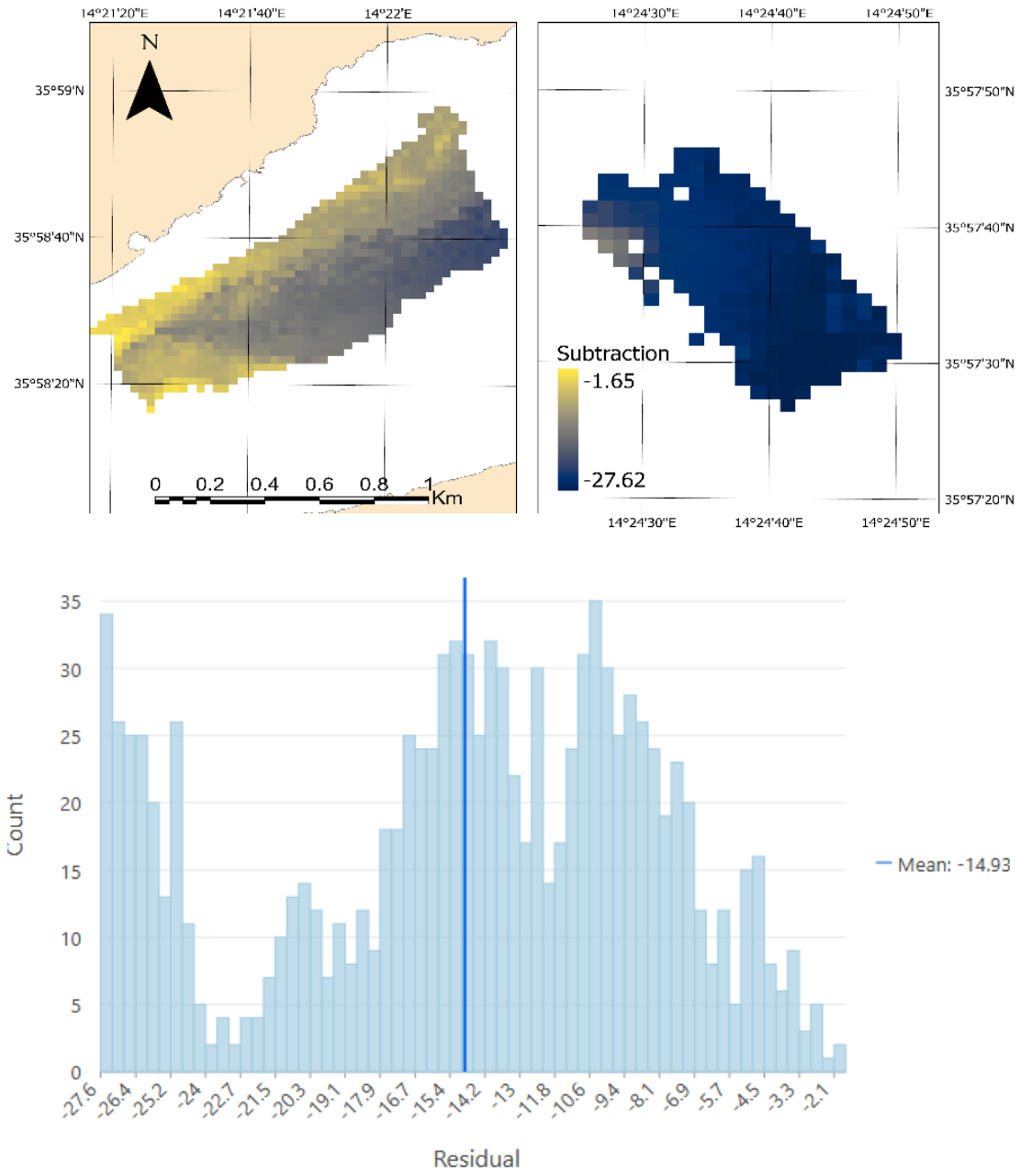

Figure 5.1.7 - Difference between actual and predicted depths for Landsat 9 at Ghadira Bay on August 29, 2024. The spatial distribution of errors (top) and the distribution of residuals (bottom)

II. Planet Scope: like Landsat 9, a positive linear relationship is observed between depth and error, though the spread of points is larger, indicating wider dispersion in the accuracy of the Planet Scope data compared to Landsat 9. Figure 5.1.8 depicts an accumulation of dark blue areas, predominantly in the central and northwestern regions. In contrast, peripheral and shallower regions and some scattered areas displayed yellow values. The histogram exhibits a left-skewed distribution with a mean residual of -12.65 m, confirming the model's tendency to overpredict depth. The presence of a few isolated bars at the extremes suggests the existence of outliers, which could be the result of measurement errors, anomalous data or extreme environmental conditions.

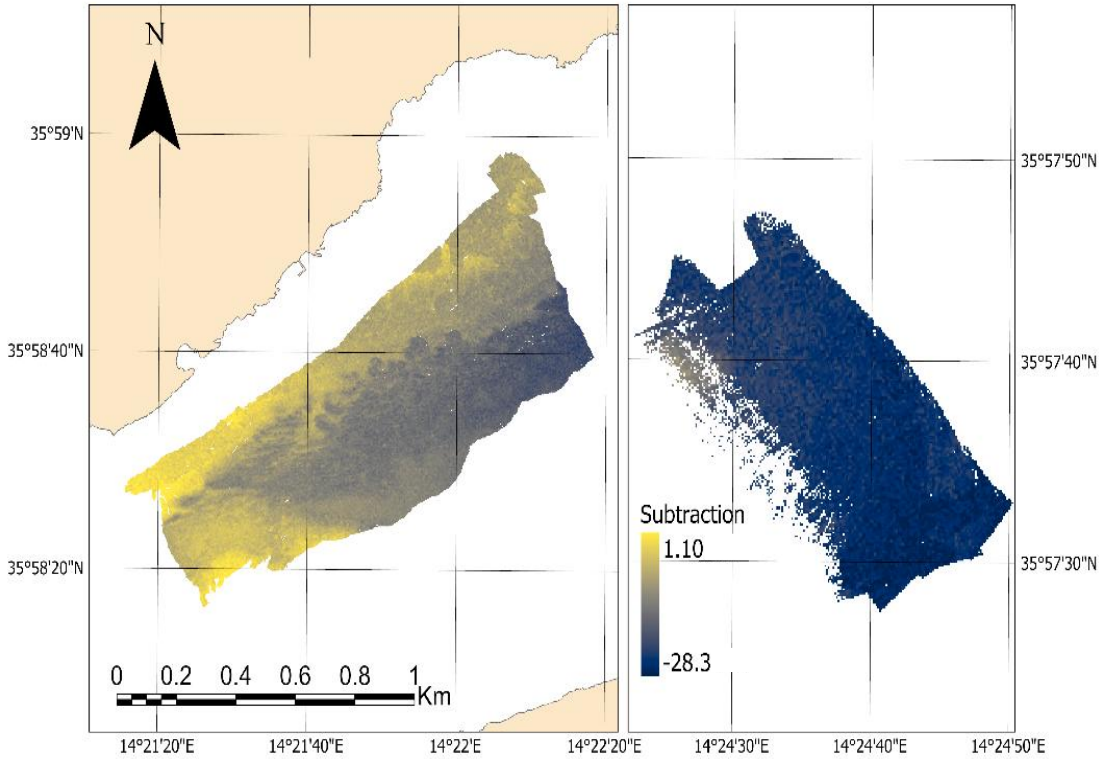

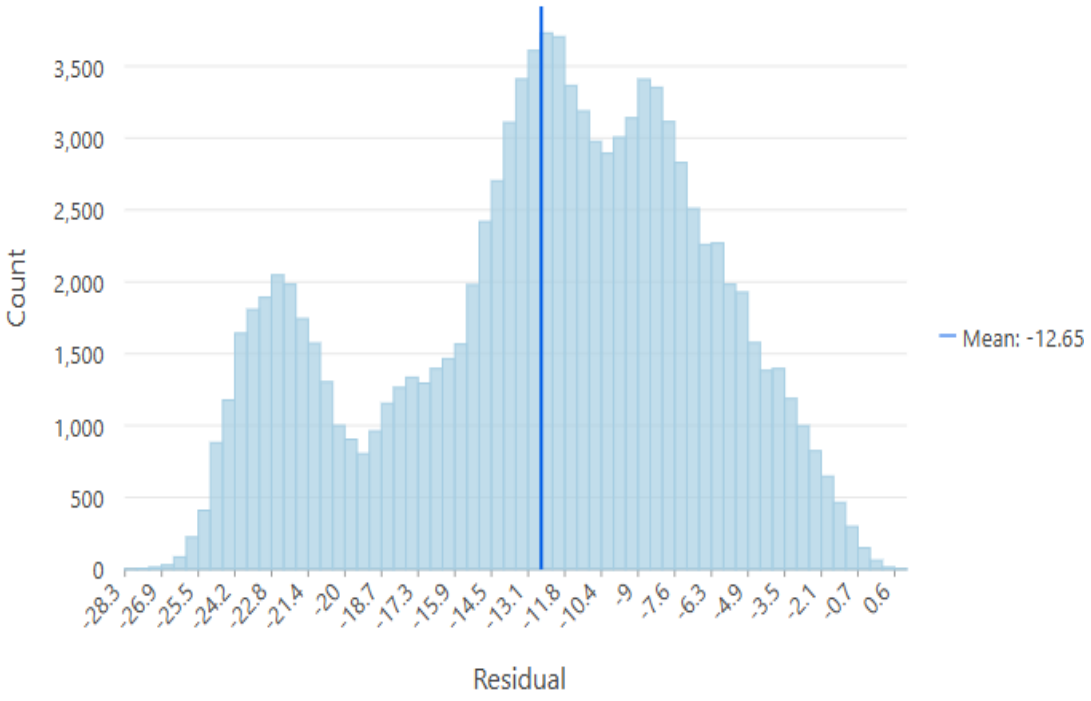

Figure 5.1.8 - Difference between actual and predicted depths for Planet Scope at Ghadira Bay on June 19, 2024. The spatial distribution of errors (top) and the distribution of residuals (bottom)

III. Sentinel 2-A: a very strong positive linear relationship is observed between depth and error, but with a very noticeable spread of points. This suggests significant inconsistency in the accuracy of Sentinel 2-A, like Planet Scope. The presence of outliers is also evident. Figure 5.1.9 reveals dark blue domination in the central and deeper areas, while yellow patches at the edges suggest underestimation or minor errors, reflecting local variations in model performance. Likewise, the histogram displays a left-skewed distribution with a mean residual of -26.05 m, the most negative among the satellites, confirming a pronounced tendency to overpredict depth.

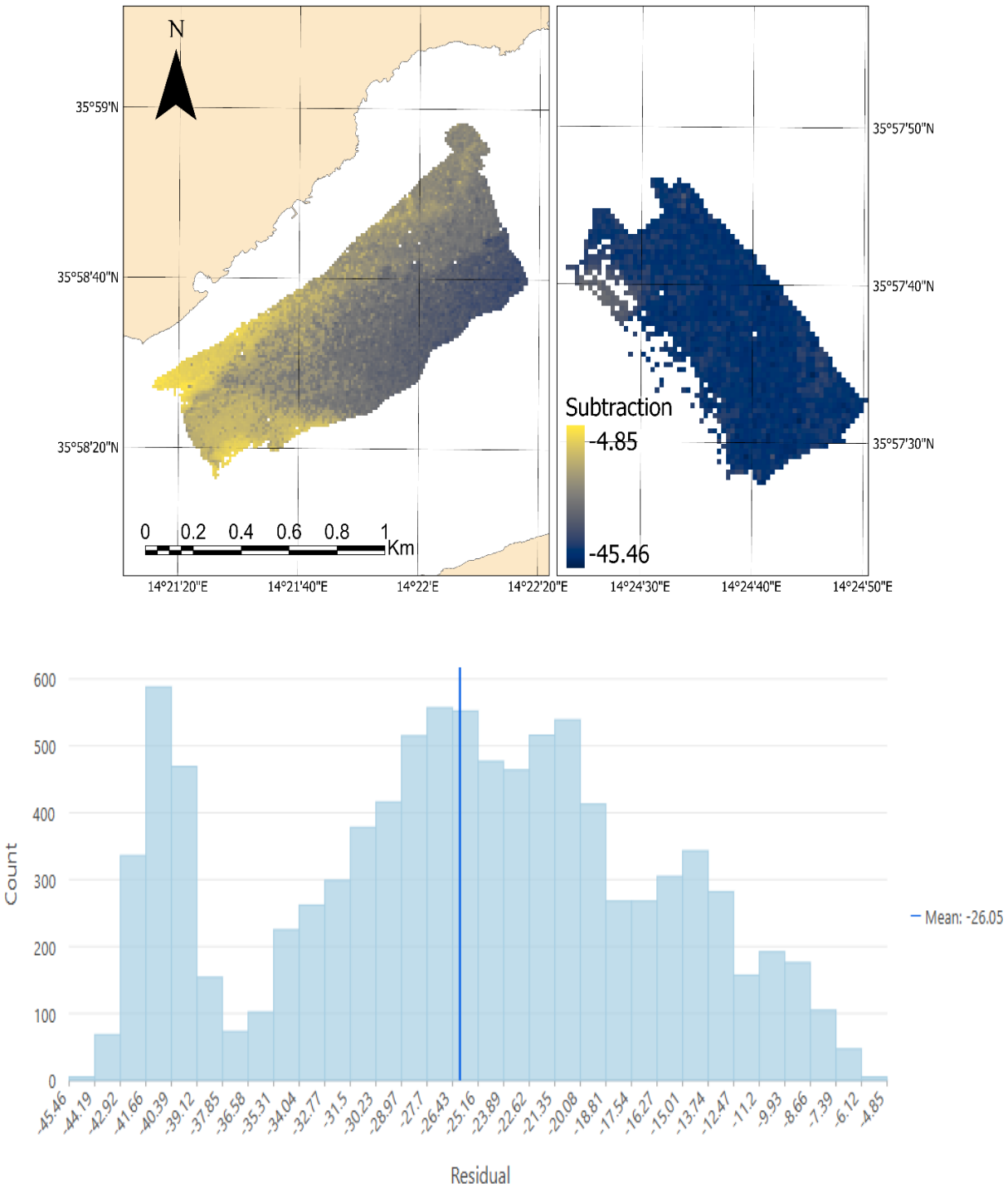

Figure 5.1.9 - Difference between actual and predicted depths for Sentinel 2-A at Ghadira Bay on September 28, 2024. The spatial distribution of errors (top) and the distribution of residuals (bottom)

- St. Paul Bay (Figure 5.1.10):

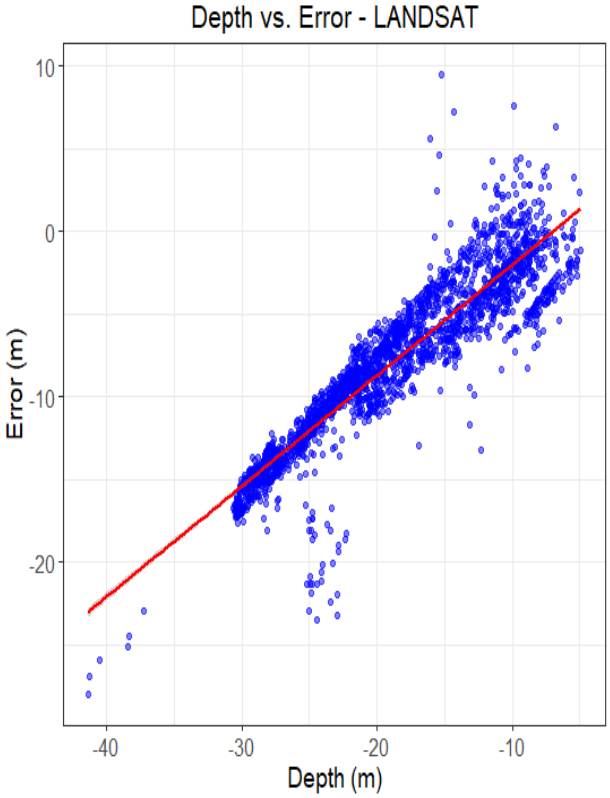

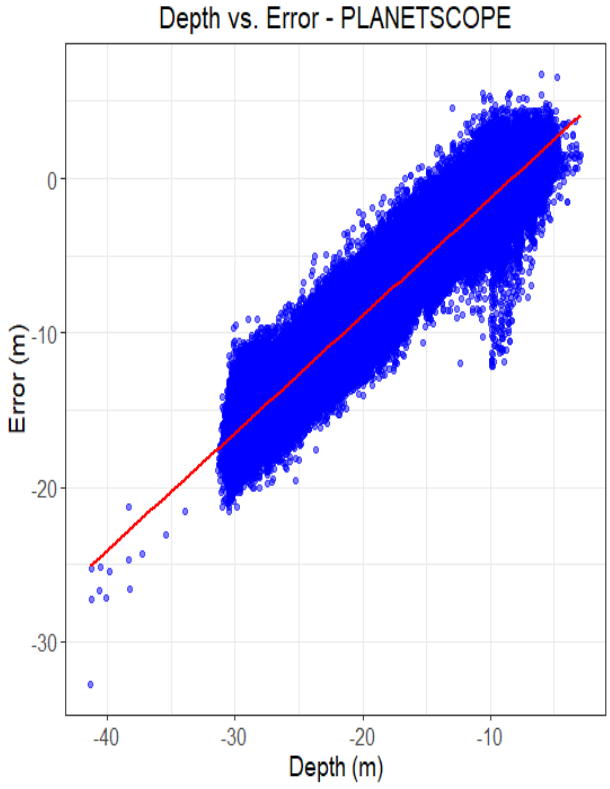

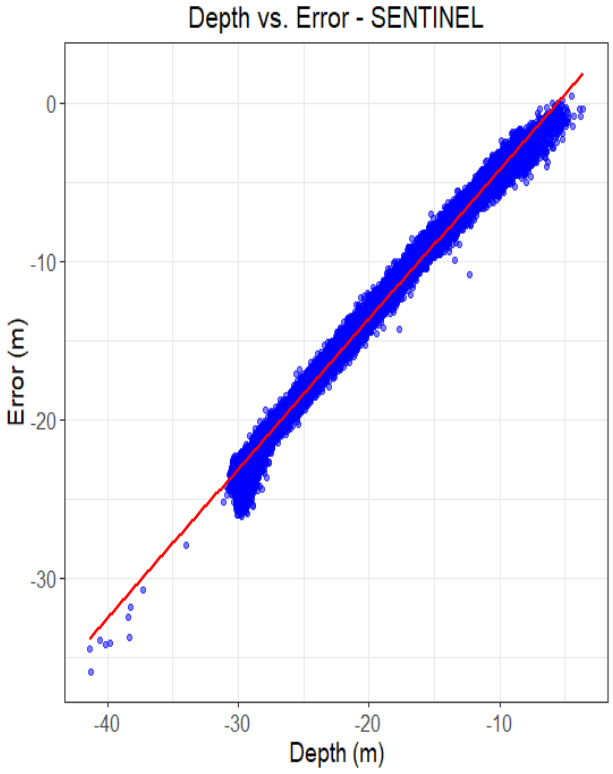

Figure 5.1.10 - Scatter plots of the relationship between depth and error for Landsat 9 (top), Planet Scope (center) and Sentinel 2-A (bottom) at St. Paul Bay

For St. Paul Bay, the linear regression was performed on a total of 232,713 samples. The intercept of 6.18, with a standard error of 0.01 and a p-value ≈ 0, indicates that when the corrected mean depth is zero, the error is 6.18 m, a significant value. The slope of the regression was -0.77, with a standard error of 0.0006 and a p-value ≈ 0, suggesting that for each unit increase in the corrected mean depth, the error decreases by 0.77 m, also statistically validated. The algorithm presented an adjusted R^2 of 0.8, explaining 87.24% of the changeability in the error. The F-statistic of 1,592,000 (p-value ≈ 0) confirms the equation's strong statistical significance. The RMSE of 1.95 and MAE of 1.46 indicate a good construct fit. The residuals ranged from -11.67 to 15.11, with a median of 0.17. Ten-fold cross-validation was applied to ensure the robustness of the model and the intercept parameter was set to true.

I. Landsat 9: a positive correlation was observed between depth and error, with a relatively uniform dispersion around the line of best fit. Figure 5.1.11 depicts depth overestimation is concentrated in the central and northwestern regions of the bay

while underestimation or smaller errors predominate at the edges. A clear gradient in the magnitude of these errors is evident across the bay. The histogram displays a left-skewed distribution with a mean residual of -16.72 m, reinforcing a consistent tendency toward overestimation. Compared to Ghadira Bay, where overestimation was more uniform with a mean residual of -14.93 m, St. Paul Bay exhibits greater inconsistency in error magnitude and distribution, suggesting Landsat 9 performs more reliably in Ghadira Bay.

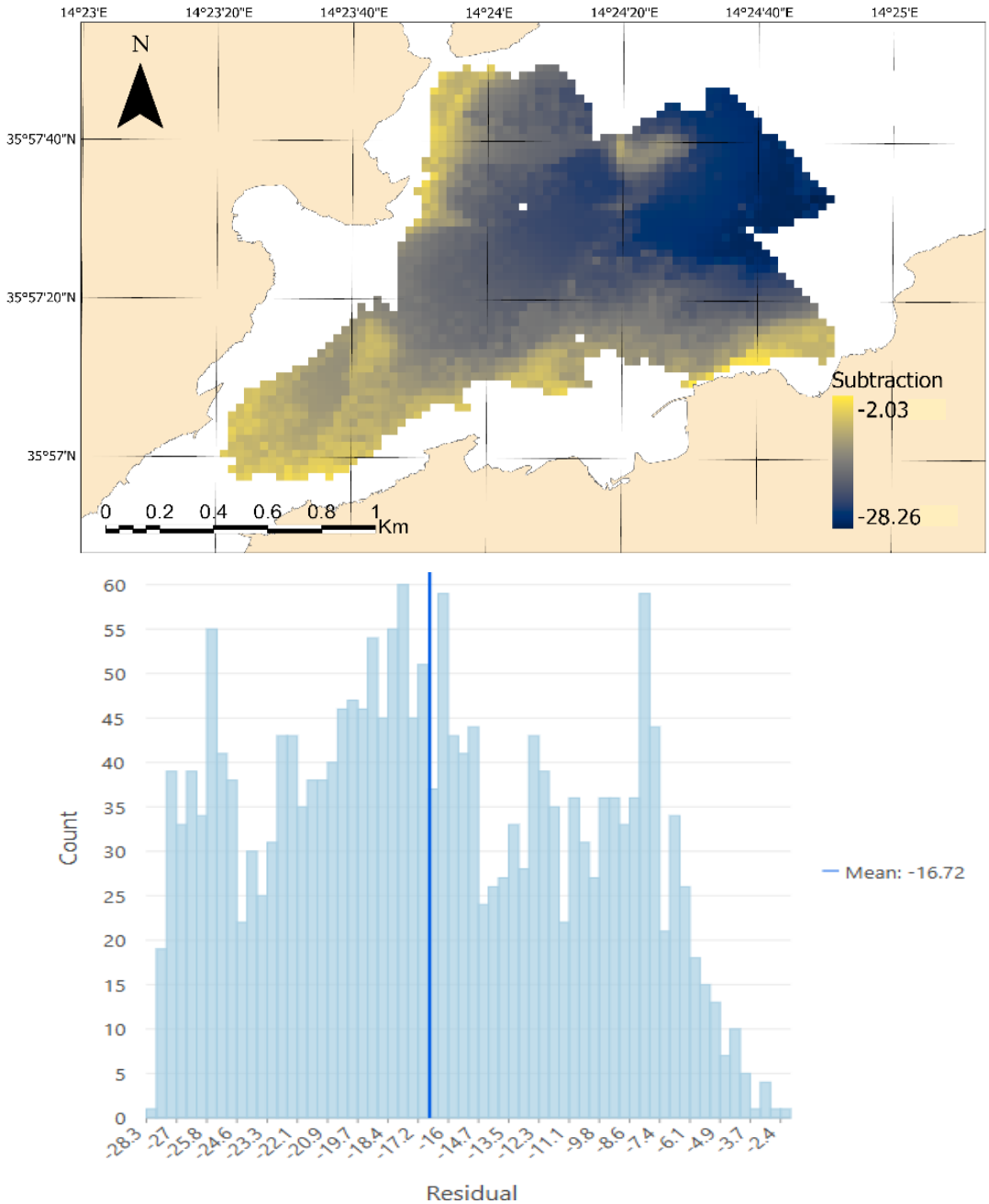

Figure 5.1.11 - Difference between actual and predicted depths for Landsat 9 at St. Paul Bay on August 29, 2024. The spatial distribution of errors (top) and the distribution of residuals (bottom)

II. Planet Scope: like in Ghadira Bay, a positive linear relationship is observed between depth and error, though the outliers are found in less depth. A density of dark blue sections is observed in the central region of the St. Paul Bay (Figure 5.1.12), extending northwestward. However, the distribution is less uniform than in Ghadira Bay, with more dispersed patches of overestimation and a greater presence of underestimation. The histogram displays a left-skewed distribution with a mean residual of -14.53 m, confirming a tendency to overestimate depth. Compared to the more consistent pattern in Ghadira Bay which was -12.65 m, it reflects greater error.

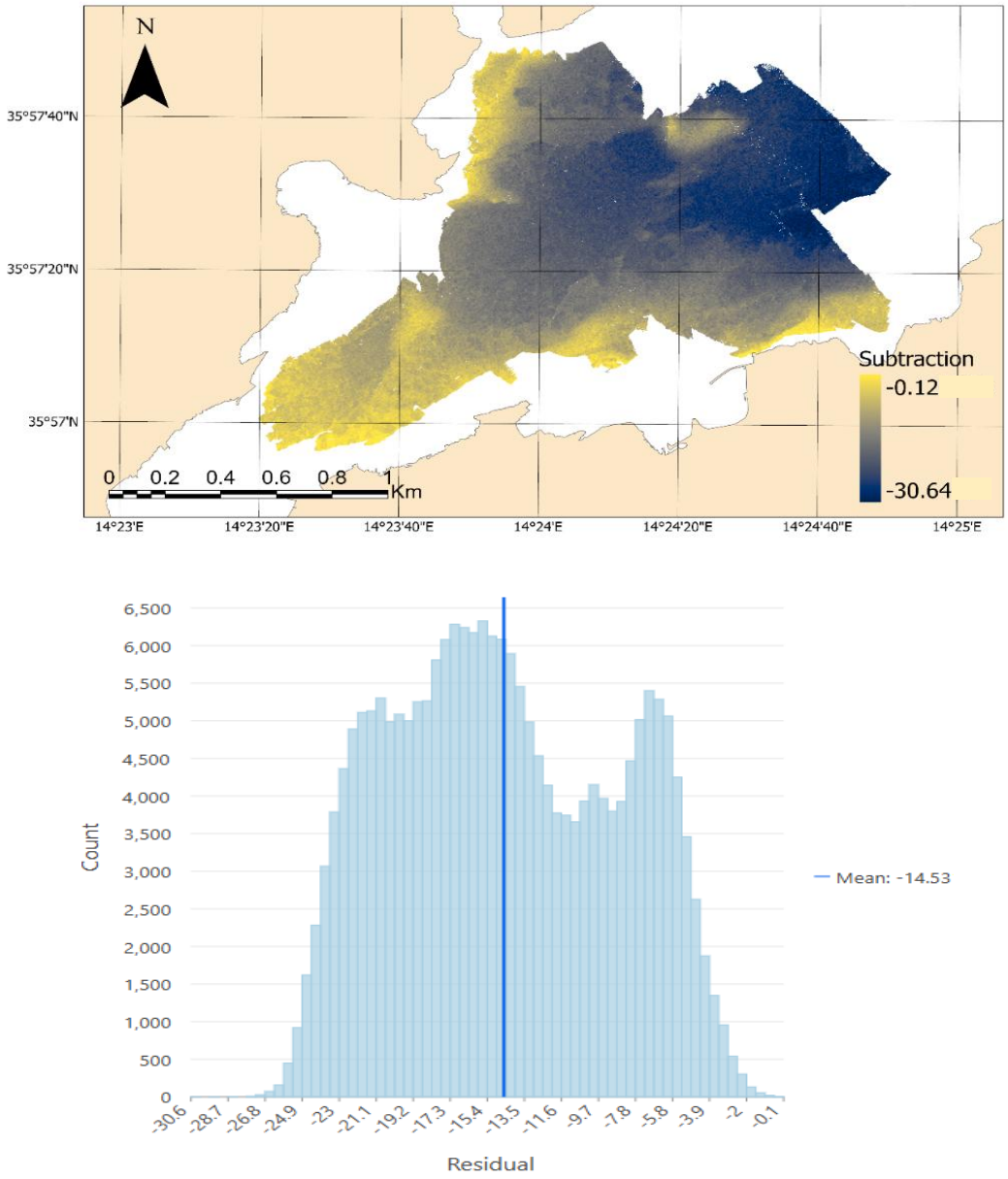

Figure 5.1.13 - Difference between actual and predicted depths for Planet Scope at St. Paul Bay June 19, 2024. The spatial distribution of errors (top) and the distribution of residuals (bottom)

III. Sentinel 2-A: a very strong positive linear relationship is observed between depth and error. Figure 5.1.13 shows a concentration of blue areas that was observed in the central region of the bay, extending northwestward. However, the distribution is less uniform than in Ghadira Bay, with more dispersed patches of overestimation and a more extensive presence of yellow areas, indicating underestimation or minor errors. This variability in accuracy across St. Paul Bay likely reflects diverse environmental conditions compared to Ghadira Bay's more consistent pattern, being -26.05 m. The histogram exhibits a left-skewed distribution with a mean residual of -9.85 m, confirming a general tendency to overestimate depth.

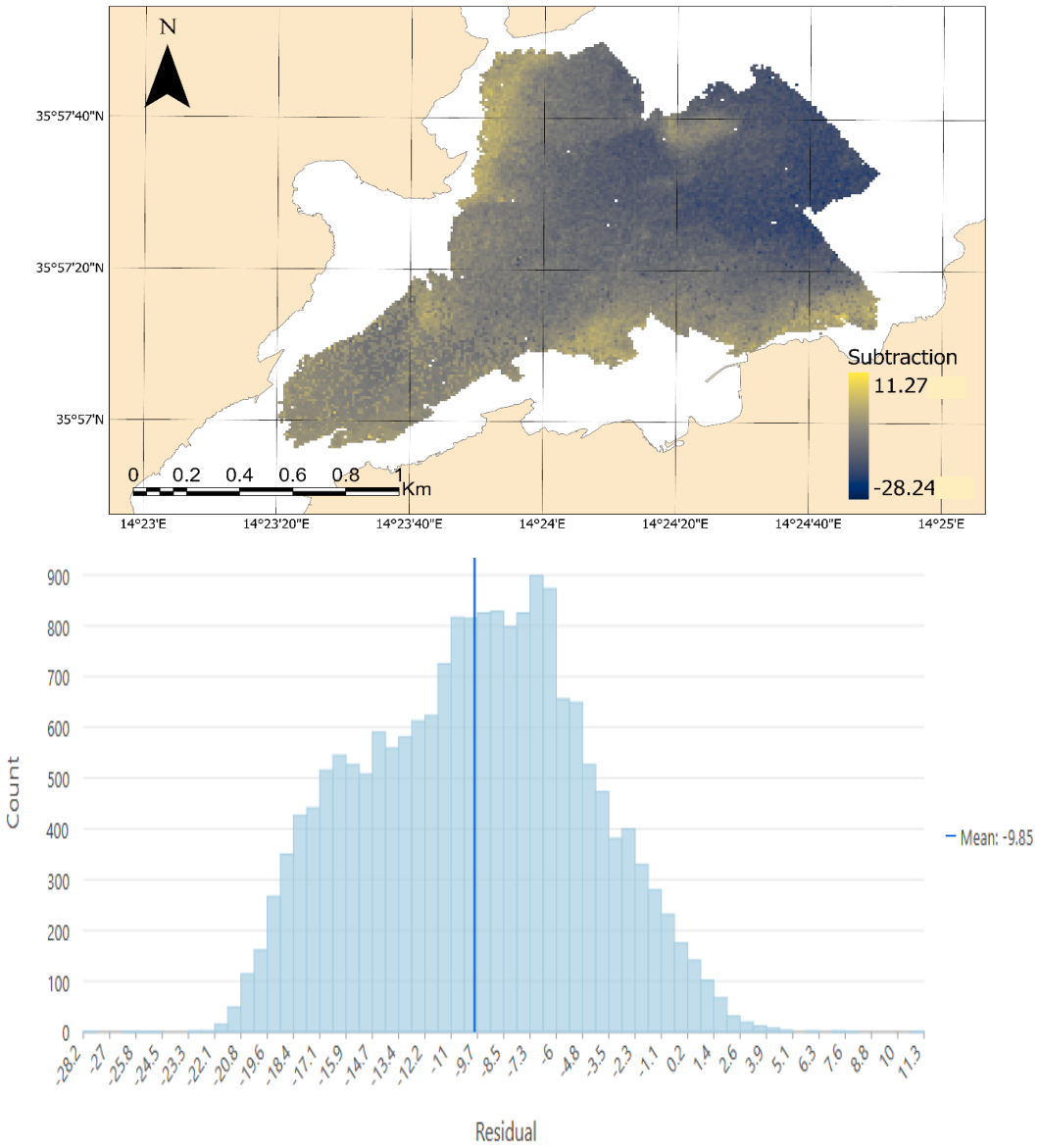

Figure 5.1.13 - Difference between actual and predicted depths for Sentinel 2-A at St. Paul Bay on September 28, 2024. The spatial distribution of errors (top) and the distribution of residuals (bottom)

While the scatter plots demonstrated a positive linear relationship between depth and error across all three satellites, a comparative analysis of results from Ghadira Bay and St. Paul Bay revealed notable trends and alteration. Specifically, all satellites exhibited a general tendency towards depth overestimation, though the extent of this overestimation differed noteworthily between satellites and study areas.

St. Paul Bay consistently displayed bigger alternation in both the distribution and magnitude of errors compared to Ghadira Bay, regardless of the satellite used. When comparing satellite performance, Landsat 9 showed the most consistent error distribution within Ghadira Bay, whereas Planet Scope and Sentinel 2-A presented more dispersed and variable error patterns.

Furthermore, variations in mean residuals and the presence of outliers were observed, suggesting differences in model performance and potential influences from measurement errors or extreme environmental conditions. Along with this, regression equation diagnostic plots provided additional information about the traditional framework's validity:

- Ghadira Bay:
    - Residuals vs. fitted and Scale-location:

      Figure 5.1.14 depicts the residuals on the y axis and the fitted values on the x axis. Ideally, the residuals should be randomly distributed around the horizontal line (zero), showing no clear pattern. However, the plot reveals a noticeable clustering of residuals, particularly around fitted values near -15 to 5, with a dense concentration of negative residuals suggesting a consistent underestimation or overestimation bias not fully captured by the linear model. The presence of this pattern, especially the upward trend in residuals at higher fitted values, implies that the model may fail to account for non-linear relationships or heteroscedasticity in the data across Ghadira Bay. The Scale-location plot complements this analysis by illustrating the relationship between fitted values and the square root of standardized residuals, with points ideally dispersed around the horizontal red line to indicate homogeneous variance. Most points are indeed scattered around this line, suggesting relatively consistent variance across fitted values, which supports the model’s assumption of homoscedasticity to some extent.

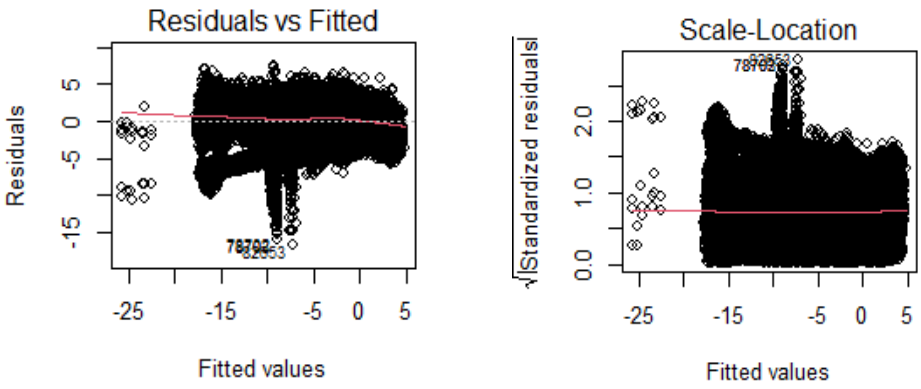

Figure 5.1.14 - Residuals vs. Fitted (left) and scale – location (right)

- Quantile-Quantile (Q-Q) residuals

  Figure 5.1.15 shows the comparison of standardized residuals with the theoretical quantiles of a normal distribution, where points aligning closely with the diagonal line indicate that. The plot shows that the residuals initially follow the diagonal line up to approximately the -1 theoretical quantile, suggesting approximate normality in the central range of the data. However, a noticeable deviation occurs beyond this point, with the curve bending upward and extending beyond the diagonal, indicating heavier tails and a departure from normality.

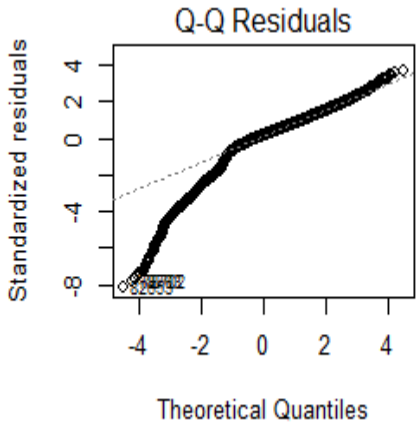

Figure 5.1.15 - Q-Q residuals

- Residuals-leverage and Cook's distance:

  Figure 5.1.16 illustrates the relationship between leverage and standardized residuals, with most data points clustered on the left side, indicating low leverage and minimal influence on the model fit. The red line, representing the fitted trend, cuts through this cluster, while dashed lines demarcate Cook's distance thresholds, highlighting influential observations. A few points, particularly those with higher leverage and residuals exceeding ±4, stand out, suggesting potential outliers or high-influence cases that could disproportionately affect the regression model's parameters. Figure 5.1.17 further details the Cook's distance by plotting distance values against the index, where most points hover near zero, indicating minimal influence across the dataset. However, prominent spikes, especially toward higher indices, reveal influential observations with significantly elevated Cook's distance values. These dominant spikes suggest that removing these specific data points could lead to noticeable shifts in the fitted regression model's parameters, pointing to the presence of outliers or extreme environmental conditions impacting the model's stability.

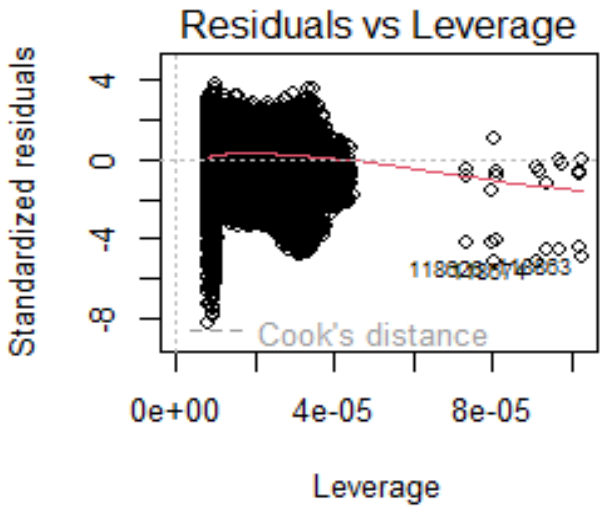

Figure 5.1.16 – Residuals-leverage

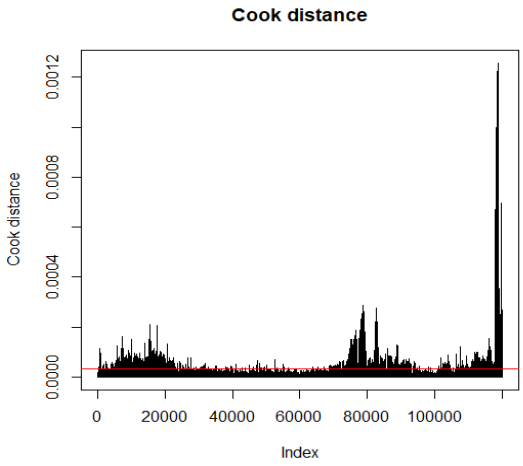

Figure 5.1.17 – Cook's distance

- St. Paul Bay:
  - Residuals vs. fitted and Scale-location:

    Figure 5.1.18 shows a seemingly random distribution of residuals around the horizontal zero line, suggesting that the regression formula meets the assumptions of homoscedasticity and linearity. The Scale-location plot complements this by plotting the square root of standardized residuals against fitted values, with an even spread around the red horizontal line indicating constant variance and supporting homoscedasticity. Most points are distributed uniformly across the fitted value range, reinforcing the model's consistency in variance. Nonetheless, a few outliers, particularly at the extremes, show slight deviations, suggesting isolated instances where variance may not be fully homogeneous.

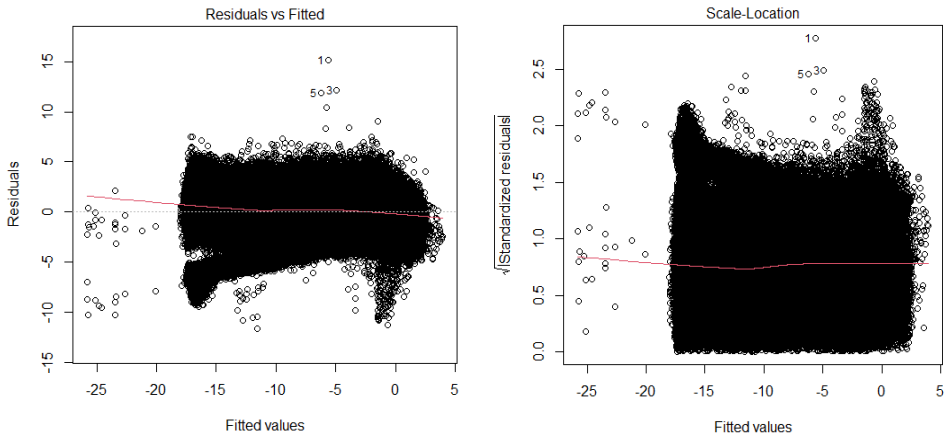

Figure 5.1.18 - Residuals vs. Fitted (left) and scale – location (right)

- Q-Q residuals:

  Figure 5.1.19 follows a linear trend close to the diagonal line that indicates an approximate normal distribution of residuals. The plot shows that residuals largely follow this diagonal until -1 theoretical quantile, suggesting good alignment with normality in the mid-range of the data. However, deviations are evident at the extremes, where points curve away from the diagonal, indicating potential outliers or heavier tails that could compromise the normality assumption.

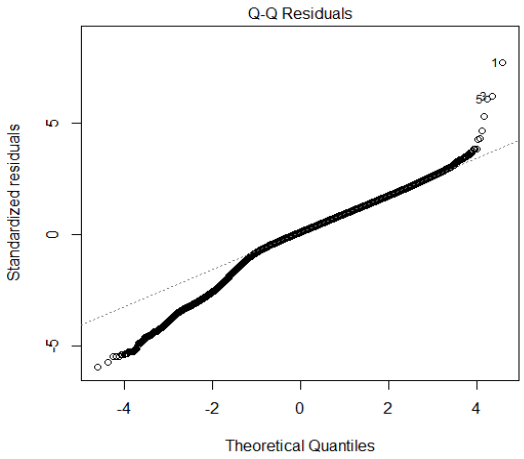

Figure 5.1.19 - Q-Q residuals

- Residuals-leverage and Cook's distance:

  Most of the data points in Figure 5.1.20 are clustered on the left side of the graph, indicating low leverage and minimal influence on the regression fit. Cook's distance thresholds highlight a few points extending beyond this boundary, particularly at higher leverage values, with indices like 22,896 and 22,910. Cook's distance graph (Figure 5.1.21) further elucidates this, indicating minimal impact on the regression equation. However, distinct spikes at specific indices reveal a small number of observations with considerably larger influence. These influential points, if removed, could lead to noticeable changes in the fitted model, underscoring the presence of

outliers that warrant closer examination to ensure the model's stability and accuracy.

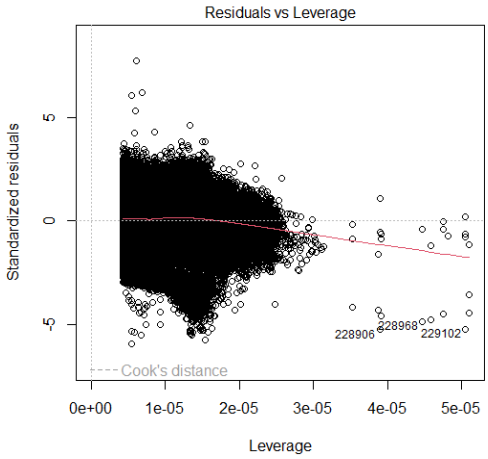

Figure 5.1.20 – Residuals-leverage

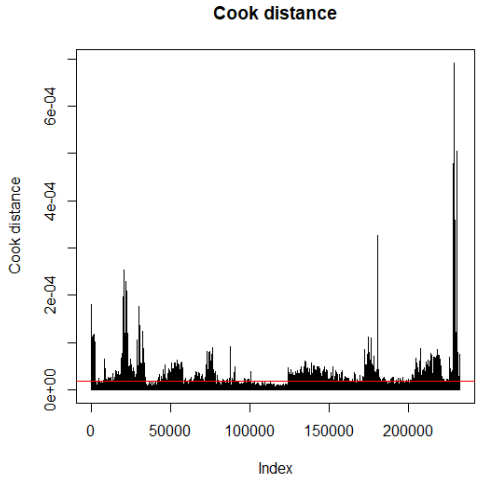

Figure 5.1.21 – Cook's distance

5.2 Random Forest regression method

I. Landsat 9: for Ghadira Bay the results showed an RMSE of 2.77 m, a Correlation Coefficient of 0.93 and an R^2 of 0.86. For St. Paul Bay achieved an RMSE of 2.53 m, a Correlation Coefficient of 0.93 and an R^2 of 0.87.

II. Planet Scope: it yielded an RMSE of 2.94 m, a Correlation Coefficient of 0.91 and an R^2 of 0.82 for Ghadira Bay. For St. Paul Bay an RMSE of 3.20 m, a Correlation Coefficient of 0.88 and an R^2 of 0.77 were obtained.

III. Sentinel 2-A: the results for Ghadira Bay indicated an RMSE of 3.34 m, a correlation coefficient of 0.88 and an R^2 of 0.77. For St. Paul Bay, an RMSE of 4.19 m, a correlation coefficient of 0.78 and an R^2 of 0.61 were achieved.

To visualize the correlation between the values predicted by each algorithm and the in-situ measured depths, scatter plots were generated for each bay**.** No specific satellite resolutions were considered. The regression line in each diagram represents the relationship between the SDB and the in-situ data, showing the line of best fit for the given data. To further understand the distribution and magnitude of errors (residuals) between in-situ depth and predicted depths by using RF in "Survey Two" bays, visualizations were generated as well as previously:

- Ghadira Bay (Figure 5.2.1):

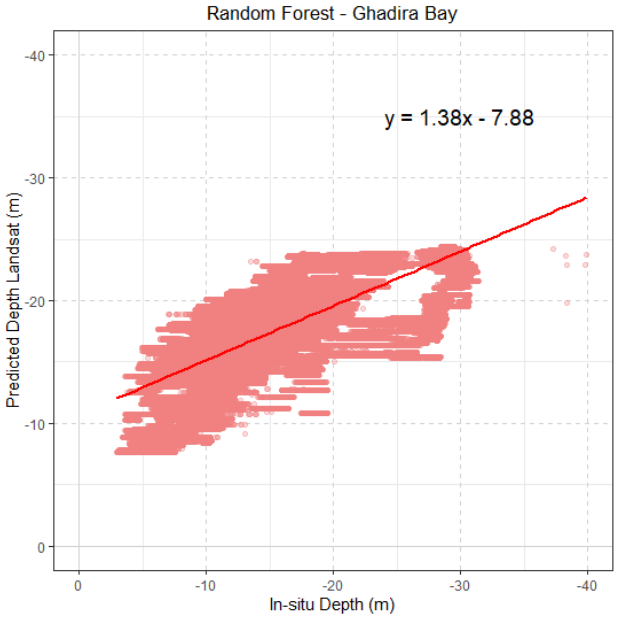

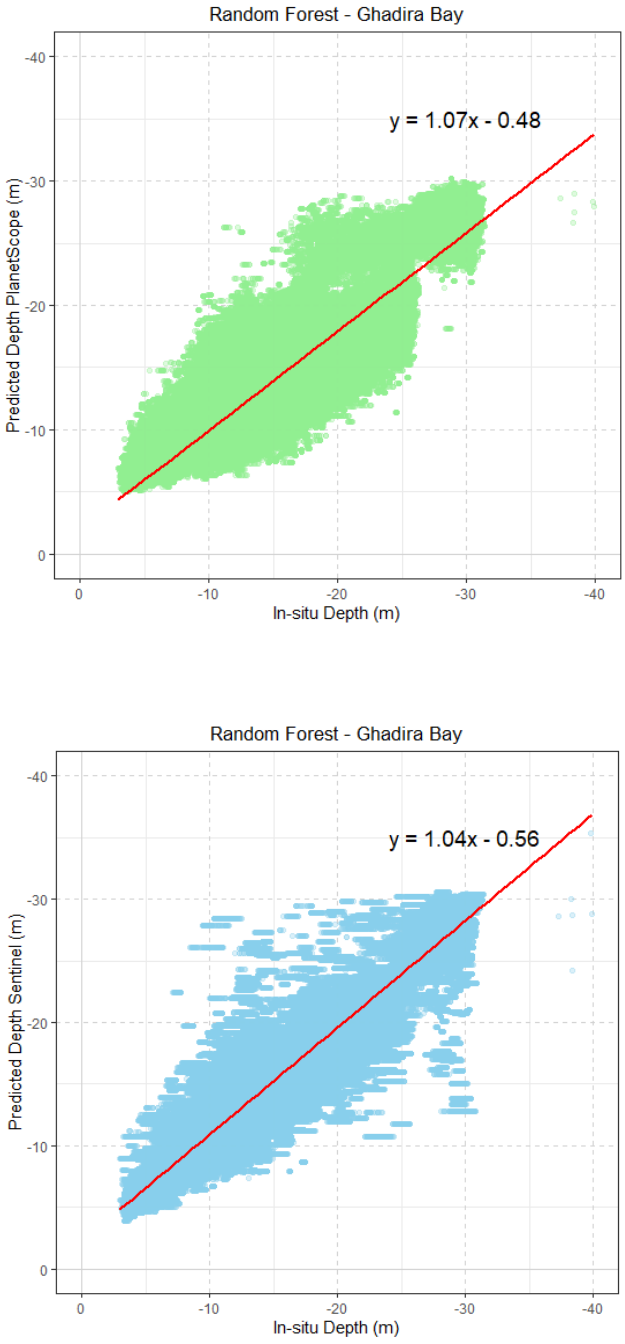

Figure 5.2.1 - Scatter plots of the relationship between in-situ depth and predicted depth for Landsat 9 (top), Planet Scope (center) and Sentinel 2-A (bottom) at Ghadira Bay

Individual linear regressions were conducted for each satellite to predict 'In-situ depth'. The resulting relationships are represented by the following formulas: for Landsat 9, $y = 1.38x - 7.88$; for Planet Scope, $y = 1.07x - 0.48$; and for Sentinel 2-A, $y = 1.04x -$

0.56. In these equations, 'y' signified the 'In-situ depth', while 'x' denoted the predicted depth from the corresponding satellite.

A separate linear regression using the average predicted depth from the three satellites as a single predictor presented 952,107 total samples, where the response variable was 'In-situ depth'. The intercept of the model was 4.83, with a standard error of 0.01 and a p-value ≈ 0, indicating that when the average predicted depth was zero, the estimated in-situ depth was -4.83 m, this value reaching statistical significance. The slope of the formulation for the average predicted depth was -1.29, with a standard error of 0 and a p-value ≈ 0, suggesting that for each meter increase in the average predicted depth, the in-situ depth increases by -1.29 m, this result also being significant. This coefficient represented the combined influence of the three satellites' predictions on the estimation of the in-situ depth. The equation presented an adjusted R^2 of 0.91, explaining approximately 91% of the fluctuation in the in-situ depth. The F statistic was 9,523,074.21 (p-value ≈ 0), the RMSE was 2.08 and the MAE was 1.66, indicating that the overall system is carrying statistical weight and has a good fit to the data. The residuals ranged from -14.27 to 10.17, with a median of -0.28. Ten-fold cross-validation was used to ensure the robustness of the model.

I. Landsat 9: its predicted depths show a positive linear trend when compared to in-situ measurements, consistently appearing greater than the actual depths. Figure 5.2.2 reveals negative errors extending up to -18.56 m, suggesting that the predicted depths are shallower than the in-situ measurements across extensive areas. While positive errors reach as high as 11.9 m, the prevalence of negative residuals points to an overall tendency for the RF model to overestimate depth in this region. The histogram displays a bimodal distribution of residuals, highlighting two distinct error groups: a primary peak at negative values, reflecting a consistent overestimation trend, and a secondary, smaller peak at positive values, indicating occasional underestimation. The mean residual, at 0.88 m, leans toward the positive, suggesting a slight overall bias toward underestimation when considering all residuals collectively.

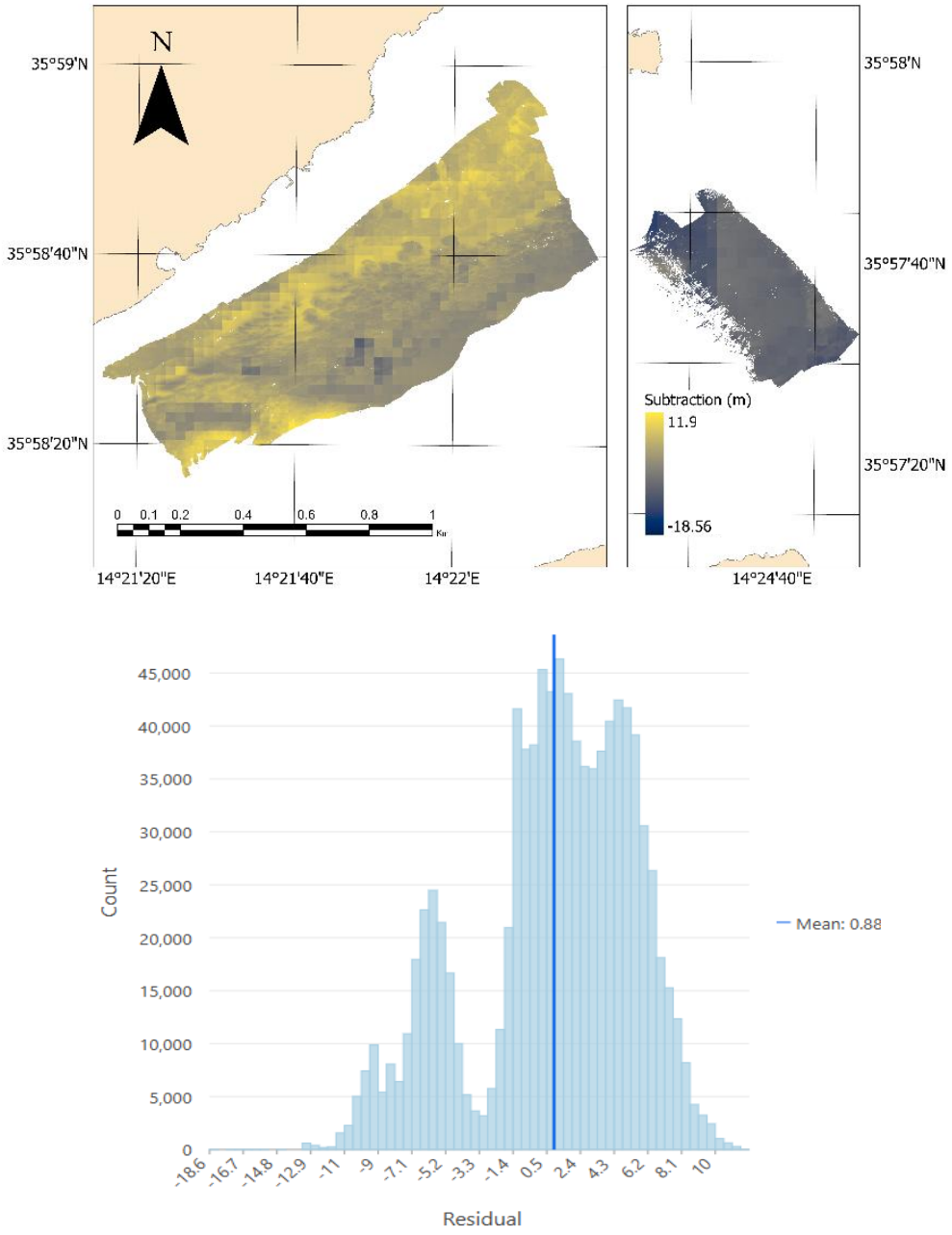

Figure 5.2.2 - Difference between in-situ and RF predicted depths for Landsat 9 at Ghadira Bay on August 29, 2024. The spatial distribution of errors (top) and the distribution of residuals (bottom)

II. Planet Scope: its scatter plot shows a dense clustering of points with a positive slope, closely aligned with the regression line, though the spread indicates some variability. Figure 5.2.3 reveals negative errors up to -13.22 m, suggesting that the predicted depths are deeper than the in-situ measurements across much of the area. Positive errors extend to 15.17 m, marking regions of underestimation, though the larger extent of overestimated areas points to a dominant overestimation trend. The

histogram of residuals showed a clear asymmetry toward negative values, with a substantial concentration of errors in this range, confirming its propensity to generate depth predictions that exceed actual values. The mean residual value of -1.63 m quantified this general bias toward overestimation in its output.

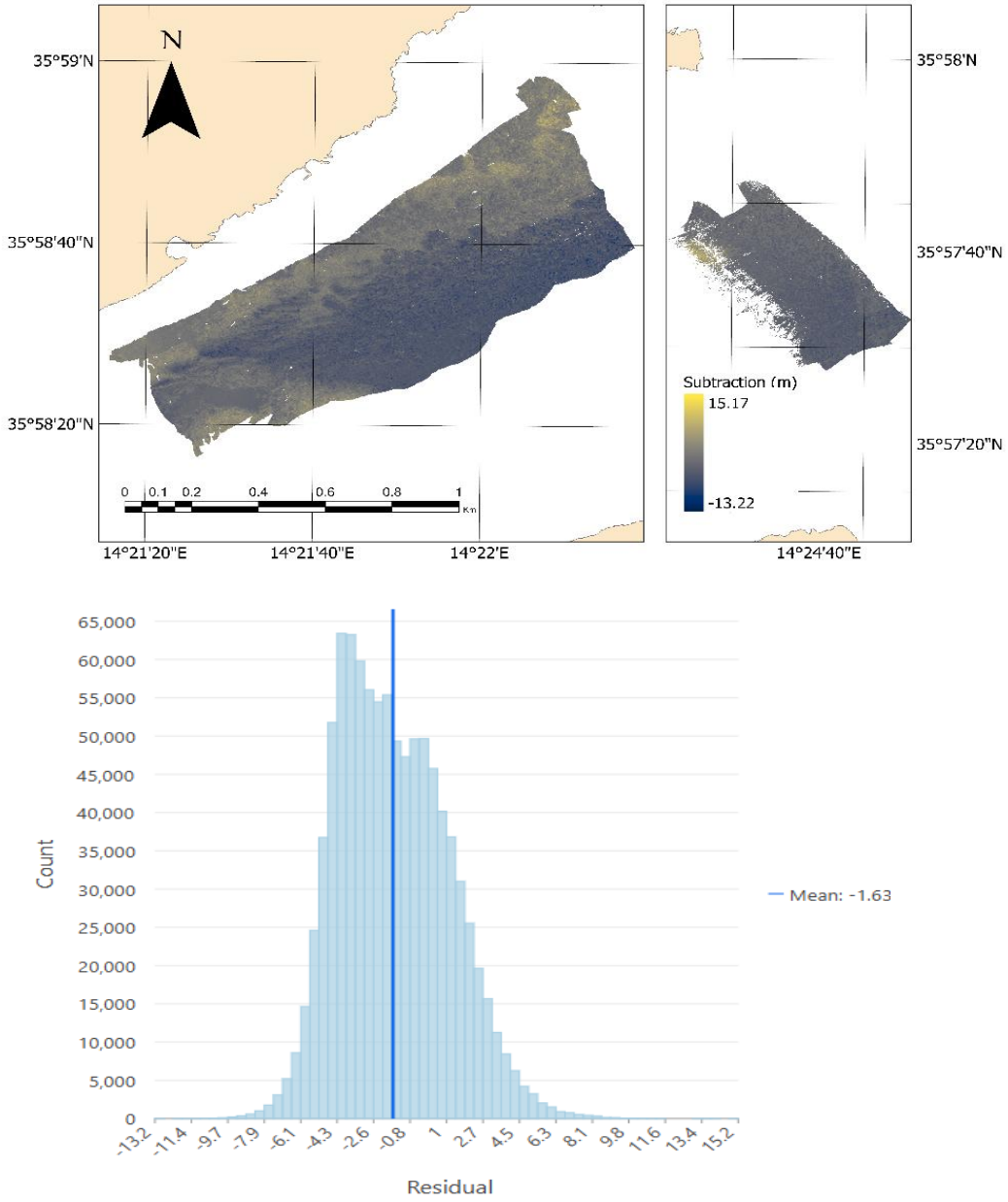

Figure 5.2.3 - Difference between in-situ and RF predicted depths for Planet Scope at Ghadira Bay on June 19, 2024. The spatial distribution of errors (top) and the distribution of residuals (bottom)

III. Sentinel 2-A: a very strong positive linear relationship is observed between depth and error as well. Figure 5.2.4 depicts negative errors of up to -19.37 m, indicating a tendency to predict shallower depths than actual ones, particularly in the central

region. In parallel, areas with positive errors reaching 18.36 m are observed, indicating scattered underestimations in the area. This spatial mutability suggests that the model's accuracy is not uniform. The histogram of the residuals showed a distribution centered on values close to zero, implying that most predictions are right. However, the presence of extended tails toward negative and positive values denoted the existence of larger errors in both directions. The mean of the residuals, very close to zero (-0.09 m), confirms that, overall, Sentinel 2-A does not exhibit a meaningful bias toward overestimation or underestimation for this data set.

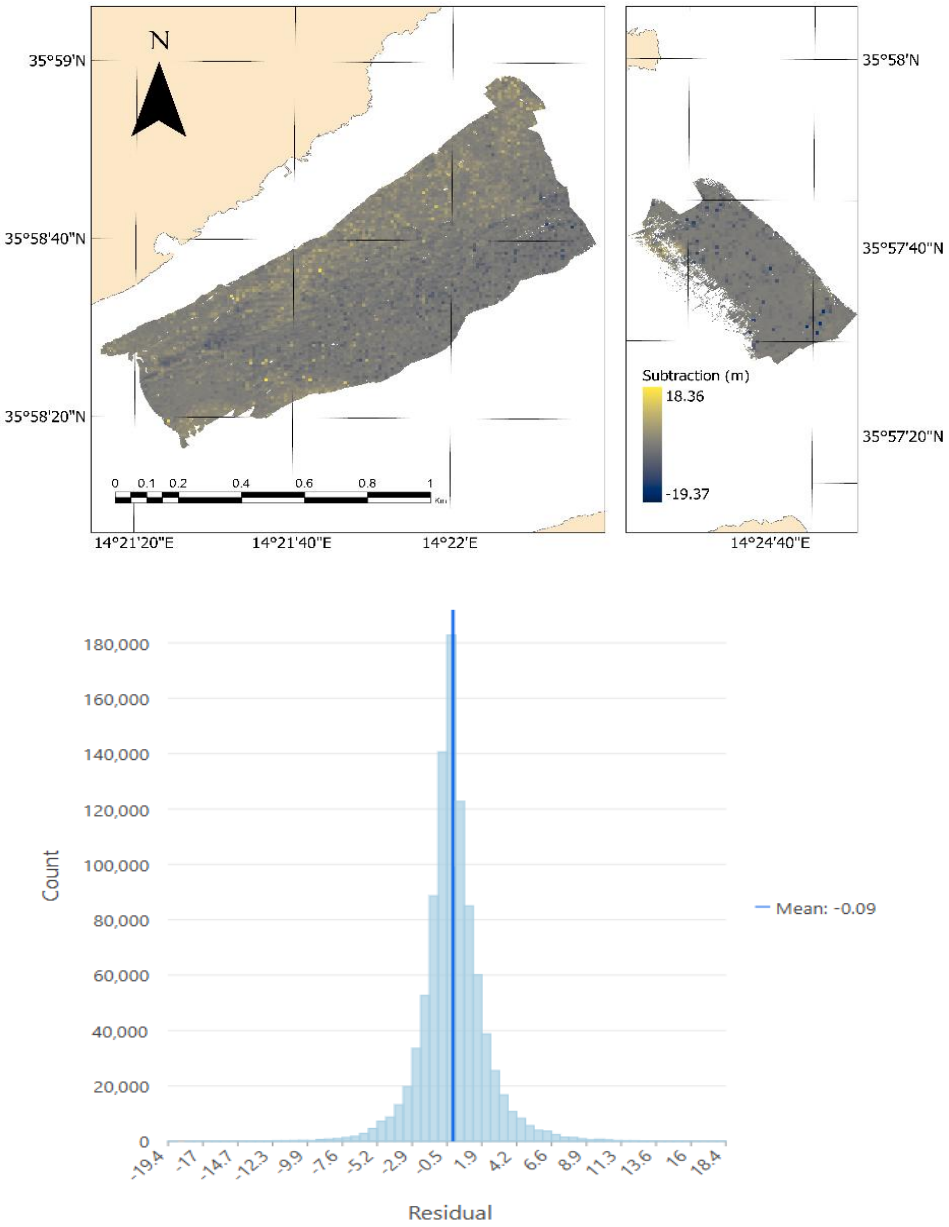

Figure 5.2.4 - Difference between in-situ and RF predicted depths for Sentinel 2-A at Ghadira Bay on September 28, 2024. The spatial distribution of errors (top) and the distribution of residuals (bottom)

- St. Paul Bay (Figure 5.2.5):

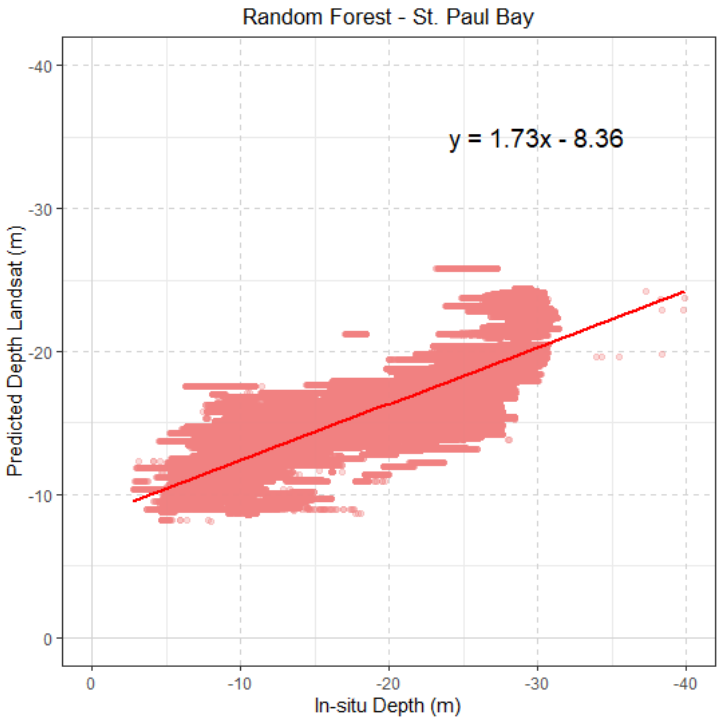

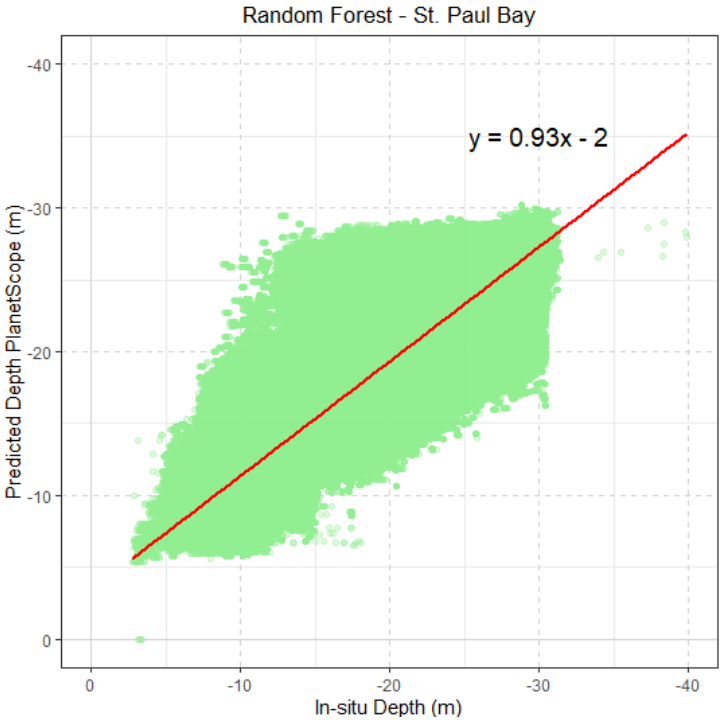

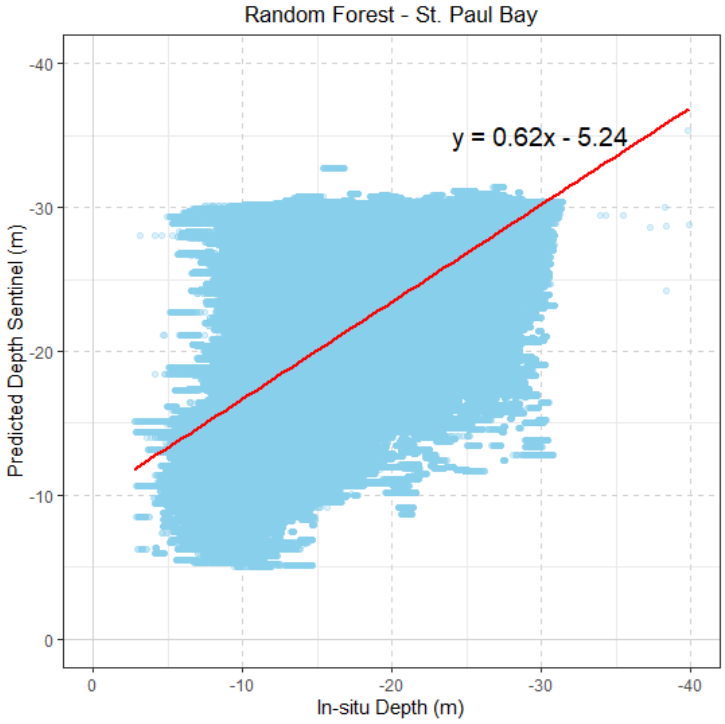

Figure 5.2.5 - Scatter plots of the relationship between in-situ depth and predicted depth for Landsat 9 (top), Planet Scope (center) and Sentinel 2-A (bottom) at St. Paul Bay

The resulting relationships for St. Paul Bay are represented by the following equations: for Landsat 9, $y = 1.73x - 8.36$; for Planet Scope, $y = 0.93x - 2$; and for Sentinel 2-A, $y = 0.62x - 5.24$.

The linear regression presented 1,878,089 total samples, where the intercept of the model was 5.22, with a standard error of 0.009 and a p-value ≈ 0, indicating that when the average predicted depth from Landsat 9, Planet Scope and Sentinel 2-A was zero, the estimated mean depth was -5.22 m, this value demonstrated statistical significance. The slope of the formulation for the average predicted depth was 1.27, with a standard error of 0.0005 and a p-value < ≈ 0, suggesting that for each meter increase in the average predicted depth, the mean depth increases by -1.28 m, this result also found to be statistically robust. This coefficient represented the combined influence of the three satellites' predictions on the estimation of the mean depth. The system presented an adjusted R^2 of 0.79, explaining approximately 79.45% of the variability in the mean depth. The F statistic was 7,262,132.15 (p-value ≈ 0), the RMSE was 2.98 and the MAE was 2.32, highlighting the model's strong performance and fruitful representation of the data. The residuals ranged from -15.13 to

14.70, with a median of -0.35. Ten-fold cross-validation was used to ensure the robustness of the algorithm.

I. Landsat 9: the scatter plot shows a positive linear relationship between in-situ and predicted depths, indicating a tendency to overestimate depths. Figure 5.2.6 reveals a predominance of depth overestimation, with negative errors reaching -20.14 m. Although areas of underestimation are identified, with positive errors as high as 11.26 m, the extent and magnitude of overestimation appear to be greater in most of the bay. The histogram of residuals displayed a main peak at negative values, confirming the tendency toward overestimation and a secondary peak at positive values, also indicating cases of underestimation. The mean residual of -3.4 m confirms a general bias toward overestimation in depth predictions. Comparison between the two bays suggests that the model tends to overestimate depth in both areas, but this tendency appears to be more pronounced and consistent in St. Paul Bay, as indicated by a more negative residual mean and a larger extent of areas with pronounced negative errors. The bimodal distribution of the residuals was observed in both bays, suggesting similar error patterns, albeit with differences in the relative magnitude of the peaks and overall bias.

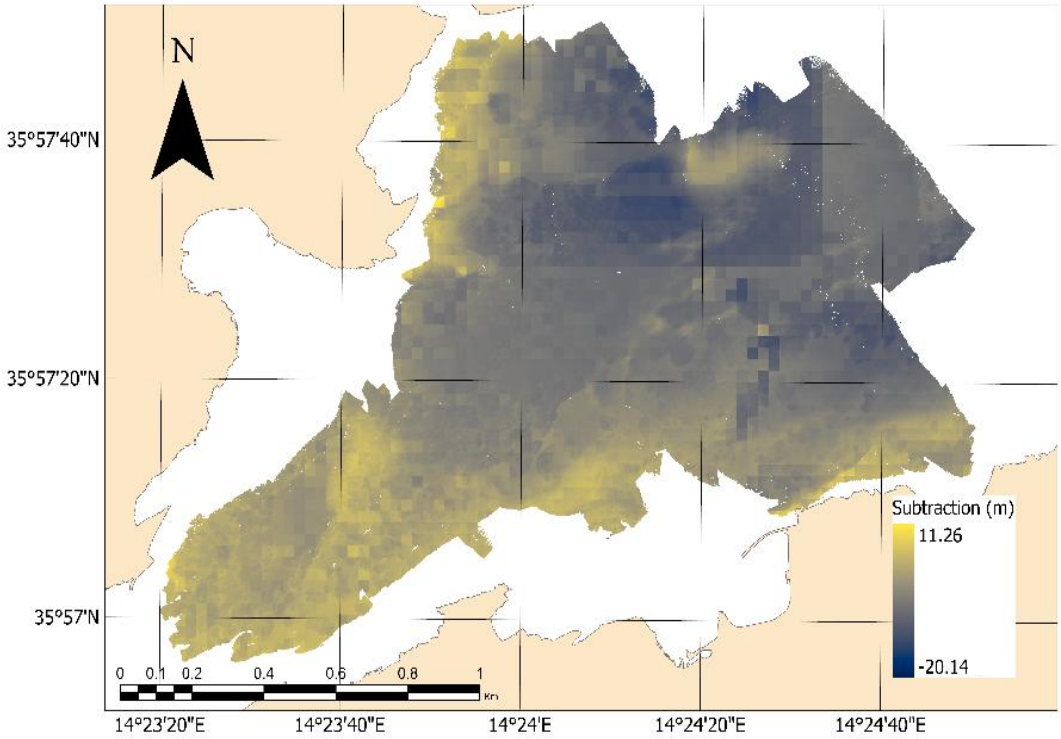

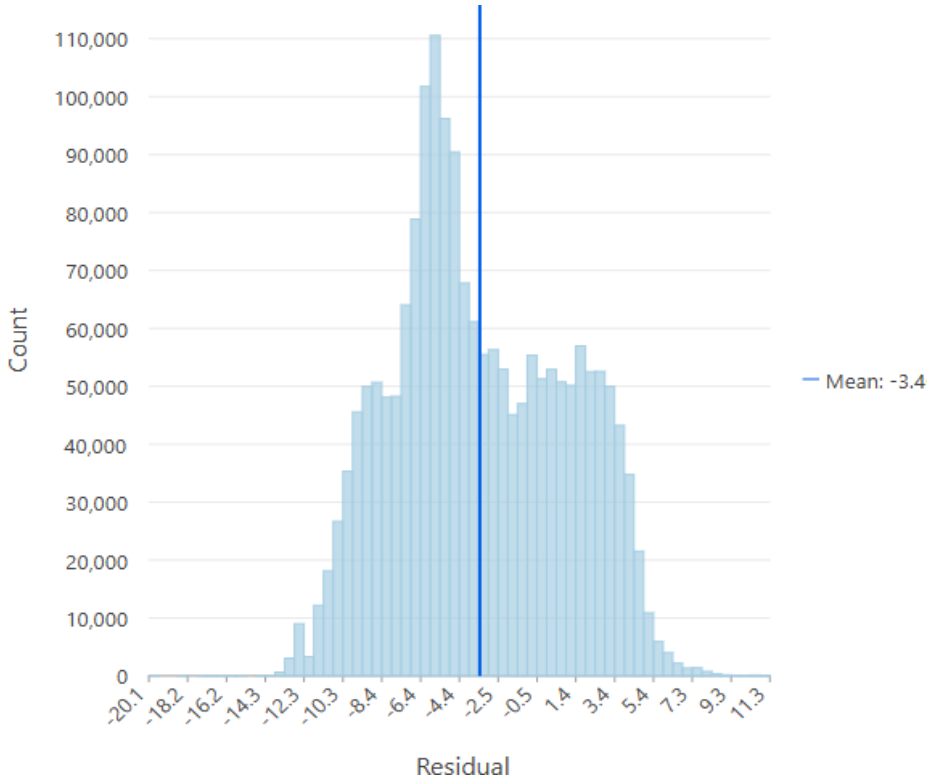

Figure 5.2.6 - Difference between in-situ and RF predicted depths for Landsat 9 at St. Paul Bay on August 29, 2024. The spatial distribution of errors (top) and the distribution of residuals (bottom)

II. Planet Scope: its scatter plot reveals a positive linear relationship between in-situ and predicted depths. Figure 5.2.7 shows a tendency to estimate depths cured than those observed in much of the area, with negative errors reaching -15.9 m. Although there are areas where the prediction underestimated the depth, reaching positive errors of 17.25 m, the extent of the areas with overestimation is considerably larger. The histogram of the residuals showed slightly negative concentration error, confirming the general tendency toward overestimation. The average value of the residuals, located at -0.57 m, quantifies this slight bias toward predicting excessive depths. Comparing both bays, a consistent trend toward overestimation of depth is observed. However, the overall bias, as measured by the mean of the residuals, was slightly smaller in St. Paul Bay (-0.57 m) compared to Ghadira Bay (-1.63 m). The distribution of residuals showed a negative skew in both bays, although the asymmetry appeared more pronounced in Ghadira Bay. This suggests that while Planet Scope tended to

overestimate depth in both locations, the degree of overestimation was slightly less in St. Paul Bay.

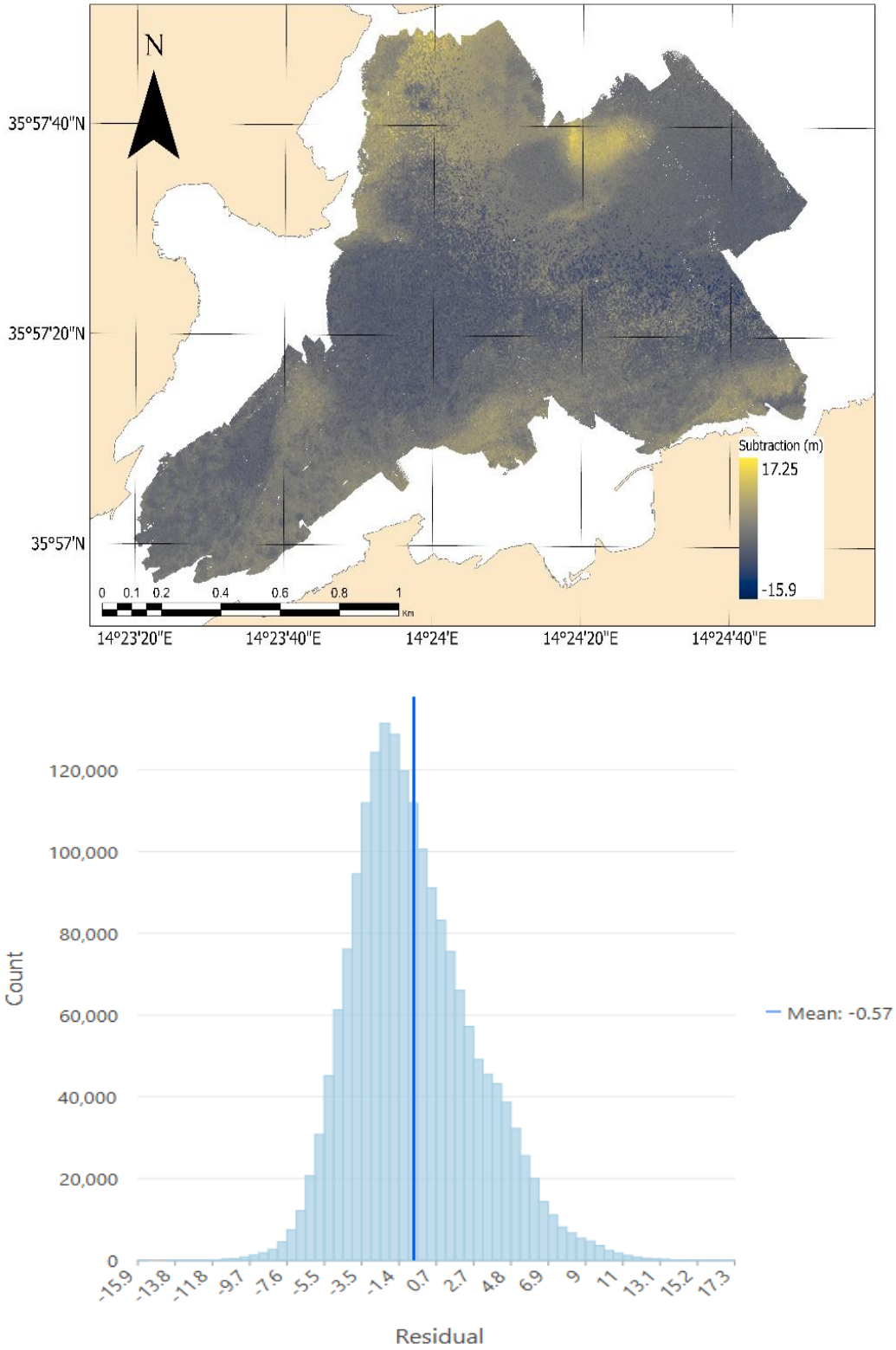

Figure 5.2.7 - Difference between in-situ and RF predicted depths for Planet Scope at St. Paul Bay on June 19, 2024. The spatial distribution of errors (top) and the distribution of residuals (bottom)

III. Sentinel 2-A: its scatter plot shows a strong positive linear trend for in-situ versus predicted depths. Figure 5.2.8 revealed a heterogeneous distribution, with areas of overestimation (up to -19.37 m) and underestimation (up to 24.91 m). The histogram of the residuals shows a unimodal distribution with a peak clearly shifted toward positive values, confirming a general tendency toward underestimation. The mean residual, 3.58 meters, confirms a general bias toward underestimation in depth predictions. The comparison between the two bays reveals contrasting behavior. In Ghadira Bay, it showed overall accuracy with minimal bias, although with errors in both directions. In St. Paul Bay, on the other hand, a clear tendency toward underestimation was observed, with a positive residual mean and a skewed residual distribution. The magnitude of underestimation errors also appeared to be bigger in St. Paul Bay compared to overestimation. This difference suggests that the performance of the Sentinel 2-A system is influenced differently by the specific characteristics of each bay, showing a greater tendency to underestimate depth in St. Paul Bay.

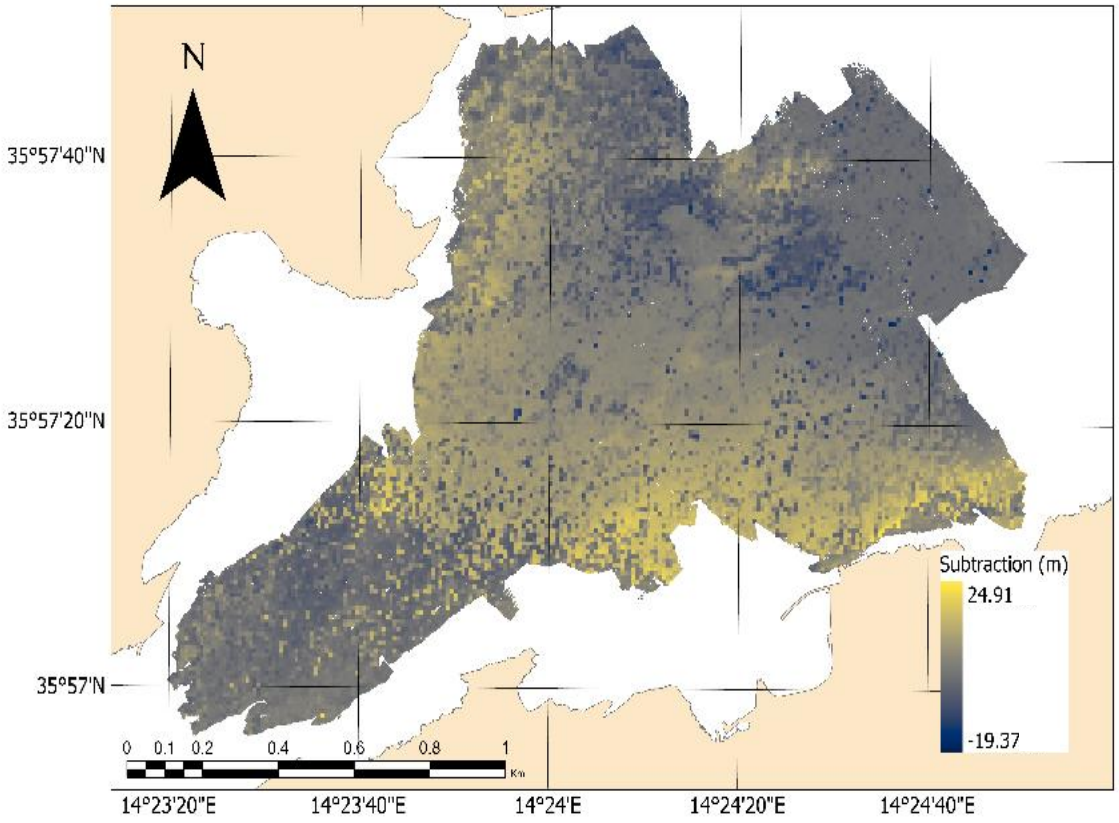

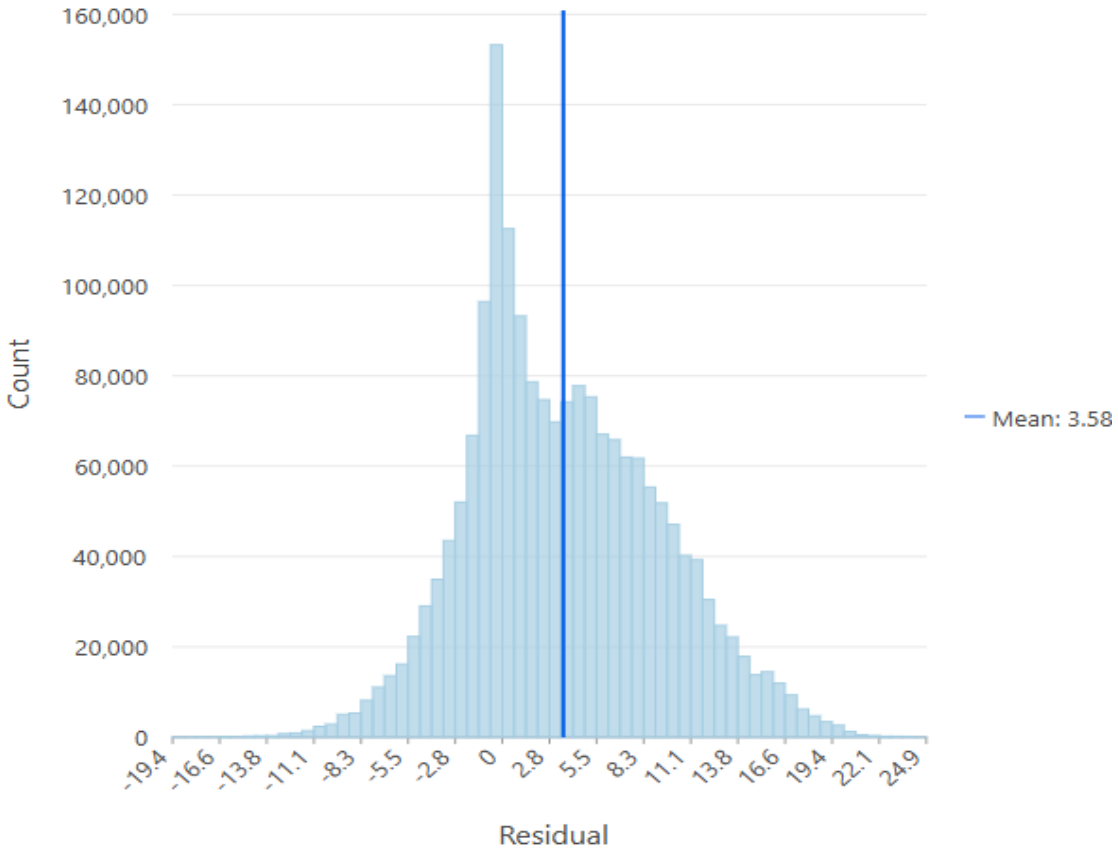

Figure 5.2.8 - Difference between in-situ and RF predicted depths for Sentinel 2-A at St. Paul Bay on September 28, 2024. The spatial distribution of errors (top) and the distribution of residuals (bottom)

While spatial visualizations revealed varying patterns of overestimation and underestimation depending on the satellite and bay, a direct comparison between Ghadira Bay and St. Paul Bay highlights significant trends and differences. Overall, all three satellites exhibited a propensity to overestimate depth in both study areas, although the degree of this overestimation varied considerably between satellites and bays. Consistently, St. Paul Bay demonstrated larger oscillation in both the distribution and magnitude of errors compared to Ghadira Bay, regardless of the satellite used. This suggests that the bathymetric characteristics or environmental conditions of St. Paul Bay present a superior challenge to the accuracy of satellite-based predictions.

When comparing satellite performance, Landsat 9 showed a relatively more consistent error distribution within Ghadira Bay, with similar patterns in both bays, albeit with differences in the magnitude of bias. In contrast, Planet Scope and Sentinel 2-A presented more dispersed

and variable error patterns, with notable differences in the overall bias trend and in the shape of the residual distribution between the two bays. This variability underscores the different sensitivities of each satellite sensor and model to the specific conditions of each coastal environment.

Besides spatial analysis, 3 maps (Figure 5.2.9) were generated for each date to provide a visual representation of how the depth values predicted by the RF algorithm vary:

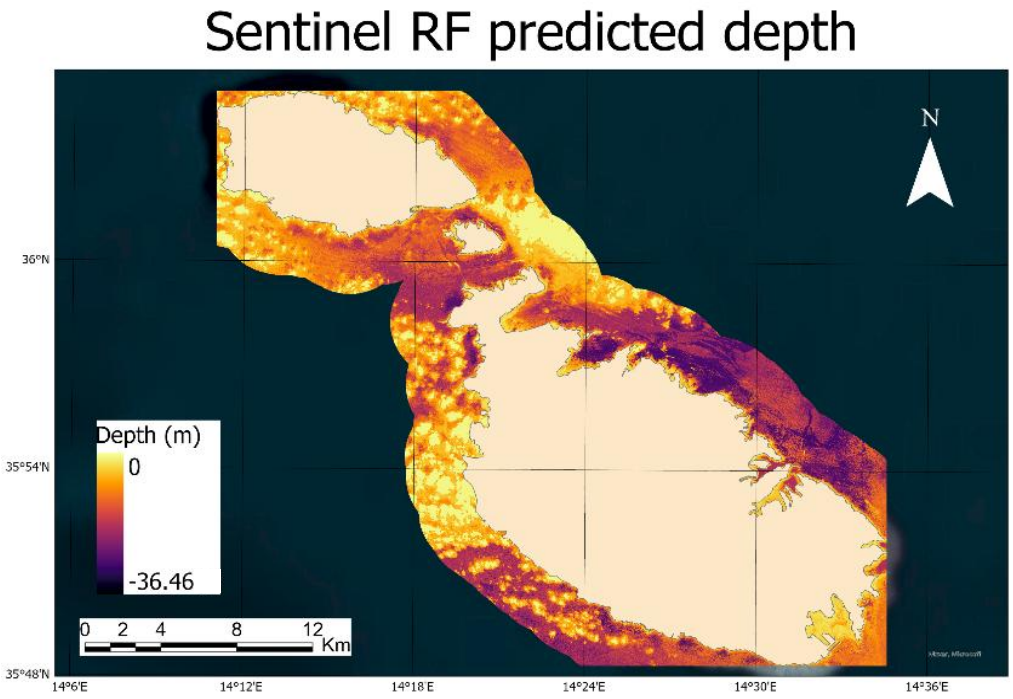

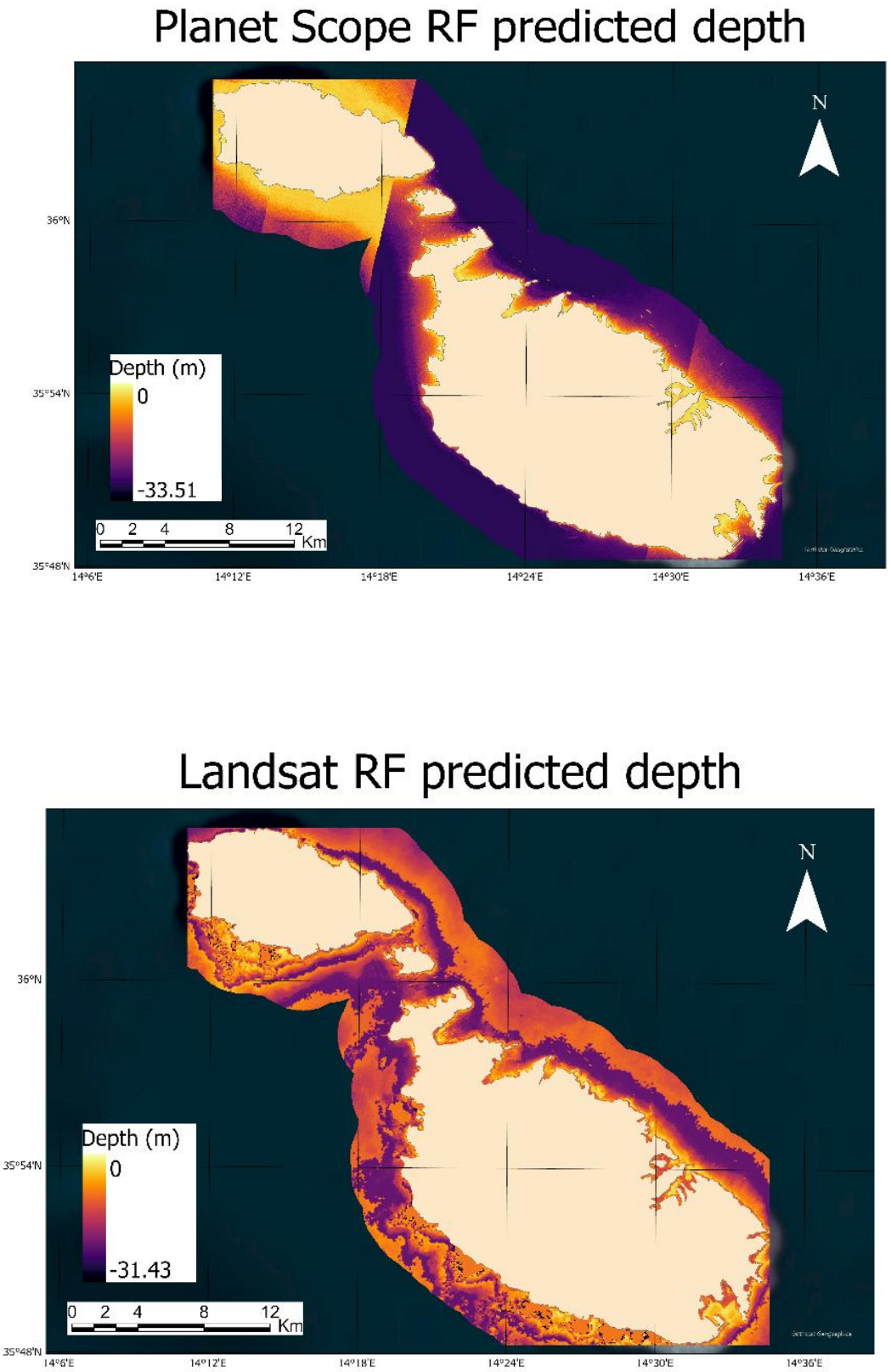

Figure 5.2.9 - Predicted depth visual representation for Sentinel 2-A (top), Planet Scope (center) and Landsat 9 (bottom) using RF

Based on the visual representation of the predicted depth using the RF algorithm applied to data from different satellites, variations are observed in the spatial detail and the estimated depth range for the region of Malta.

The bathymetry derived from Landsat 9 offers a general overview of the depth distribution. The transition from shallow waters near the coast to deeper waters offshore is clearly visible, although fine details of underwater structures are not as evident. The depth range visualized in the Landsat 9 map appears to be the most limited compared to the other sensors.

In contrast, the bathymetry predicted from Planet Scope data reveals a considerably higher level of spatial detail. This excels resolution allows for a more precise identification of seabed features near the coast and variations in depth at smaller scales. It's important to note a specific visual characteristic observed in the Planet Scope predicted depth map. The presence of a distinct line or artifact across the image is likely attributed to an inherent issue related to the data acquisition time. This artifact, therefore, does not necessarily reflect a true physical discontinuity in the bathymetry but rather a technical limitation or artifact of the satellite data acquisition and processing for Planet Scope. Despite this visual anomaly, the overall patterns and the higher spatial detail provided by PlanetScope remain valuable for understanding the nearshore bathymetry. While the general depth patterns agree with those of Landsat 9, the representation of transition zones and underwater structures is much more defined. The depth range visualized with Planet Scope extends slightly further than that of Landsat 9.

The bathymetry estimated using Sentinel 2-A data presents an intermediate level of spatial detail between Landsat 9 and Planet Scope. A significant improvement in the representation of underwater features is observed compared to Landsat 9, although it does not reach the fineness of detail provided by Planet Scope. The Sentinel 2-A map suggests a slightly bigger depth range than the other two sensors, particularly in further offshore areas.

These differences in the bathymetric representation are attributable to the inherent spatial resolution of each satellite sensor, which influences the system's ability to capture depth variations at different scales. Notably, the unique spectral characteristics of each sensor, the meteorology and the way the RF algorithm represents their relationship with the training depth measurements, also contribute to the subtle differences observed in the predicted depth mapped representations.

6. Conclusion

This study compared conventional and ML techniques for SDB in Malta's coastal waters, combining satellite data with in-situ measurements. While conventional linear regressions achieved weighty results, they systematically overestimated depths, especially in St. Paul Bay, and showed higher spatial error variation. The RF algorithm, however, proved to be more effective. It captured non-linear relationships inherently, eliminating the need for manual depth-range segmentation, and delivered superior accuracy across both study areas. Sentinel 2-A performance varied by location: predictions were balanced in Ghadira Bay but underestimated depths in St. Paul Bay, underscoring how local conditions influence model outcomes. The success of this research crucially redefines the capabilities of SDB methodologies that allow us to closely track pressures regularly while also predicting future impacts. With their high visual and temporal resolutions, combined with their wide coverage, gives us a clearer picture of both seasonal and long-term patterns and changes, complementing temporal insights.

Despite these advancements, there are still some limitations, like inaccuracies under certain conditions. The accuracy of SDB depends heavily on the quality and density of input data and meteorology. Satellite sensors can introduce uncertainties, but with well-calibrated methods, we can minimize these issues. Moving forward, I would recommend focusing on expanding and diversifying training datasets, developing correction techniques and incorporating more environmental factors into the process. Exploring machine learning approaches can further improve predictions of seasonal and longstanding changes, and validating the predictor with real world data from Malta would help ensure its reliability and applicability.

7. **Bibliography**

Al Shehhi, M. R., & Zhang, X. 2025. ***Bathymetry estimation for coastal regions using self-attention***. Scientific Reports, 15 (1), 970.

Amrari, S., Bourassin, E., Andréfouët, S., Soulard, B., Lemonnier, H., & Le Gendre, R. 2021. ***Shallow water bathymetry retrieval using a band-optimization iterative approach: application to New Caledonia coral reef lagoons using Sentinel-2 data***. Remote Sens., 13 (10), 4108.

Ashphaq, M., Srivastava, P. K., & Mitra, D. 2021. ***Review of near-shore satellite derived bathymetry: classification and account of five decades of coastal bathymetry research***. Journal of Ocean Engineering and Science, 6 (4), 340-359.

Cesbron, G., Melet, A., Almar, R., Lifermann, A., Tullot, D., & Crosnier, L. 2021. ***Pan-European Satellite-derived coastal bathymetry—review, user needs and future services***. Frontiers in Marine Science, 8, 740830.

Chénier, R., Ahola, R., Sagram, M., Faucher, M. A., & Shelat, Y. 2019. ***Consideration of level of confidence within multi-approach satellite-derived bathymetry***. ISPRS International Journal of Geo-Information, 8 (1), 48.

Duan, Z., Chu, S., Cheng, L., Ji, C., Li, M., & Shen, W. 2022. ***Satellite-derived bathymetry using Landsat-8 and Sentinel 2-A images: assessment of atmospheric correction algorithms and depth derivation models in shallow waters***. Opt. Express, 30 (3), 3238–3261.

Fitton, J. M., Rennie, A. F., Hansom, J. D., & Muir, F. M. 2021. ***Remotely sensed mapping of the intertidal zone: a Sentinel-2 and Google Earth Engine methodology***. Remote Sensing Applications: Society and Environment, 22, 100499.

French, C., Hunt, C., Grima, R., McLaughlin, R., Stoddart, S., & Malone, C. 2020. ***Temple Landscapes: fragility, change and resilience of Holocene environments in the Maltese Islands***. McDonald Institute for Archaeological Research Cambridge; Queen's University Belfast.

Giordan, D., Notti, D., Villa, A., Zucca, F., Calò, F., Pepe, A., Dutto, F., Pari, P., Baldo, M., & Allasia, P. 2018. ***Low cost, multiscale and multi-Sensor application for flooded area mapping***. Nat. Hazards Earth Syst. Sci., 18 (5), 1493–1516.

Han, T., Zhang, H., Cao, W., Le, C., Wang, C., Yang, X., & Lou, X. 2023. ***Cost-efficient bathymetric mapping method based on massive active–passive remote sensing data***. ISPRS Journal of Photogrammetry and Remote Sensing, 203, 285-300.

Janowski, L., Trzcinska, K., Tegowski, J., Kruss, A., Rucinska-Zjadacz, M., & Pocwiardowski, P. 2018. ***Nearshore benthic habitat mapping based on multi-Frequency, multibeam echosounder data using a combined object-based approach: a case study from the Rowy Site in the southern Baltic Sea***. Remote Sens., 10 (12), 1983.

Jawak, S.D.; Vadlamani, S.S., Luis, A.J. ***A synoptic review on deriving bathymetry information using remote sensing technologies: models, methods and comparisons***. Adv. Remote Sens. 2015, 4, 147.

Lichter, M., Vafeidis, A. T., Nicholls, R. J., & Kaiser, G. 2011. ***Exploring data-related uncertainties in analyses of land area and population in the "low-elevation coastal zone" (LECZ)***. COAS, 27 (4), 757–768.

Lubac, B., Burvingt, O., Nicolae Lerma, A., & Sénéchal, N. 2022. ***Performance and uncertainty of satellite-derived bathymetry empirical approaches in an energetic coastal environment***. Remote Sensing, 14 (10), 2350.

Said, G., & Schembri, J. 2010. 8.17 Malta. ***Encyclopedia of the world's coastal landforms***, 751-759.

Sammut, S., Gauci, R., Drago, A., Gauci, A., & Azzopardi, J. 2017. ***Pocket beach sediment: a field investigation of the geodynamic processes of coarse-clastic beaches on the Maltese islands (Central Mediterranean)***. Marine Geology, 387, 58-73.

Schembri, P. J. 1993. ***The Maltese coastal environment and its protection. Atti dell'ottavo convegno internazionale: mare e territorio, la protezione dell'ambiente Mediterraneo ed il piano della commissione delle comunità europee***. Università degli Studi di Palermo, Palermo, 107-112.

Stumpf, R.P.; Holderied, K.; Sinclair, M. ***Determination of water depth with high-resolution satellite imagery over variable bottom types***. Limnol. Oceanogr. 2003, 48, 547–556.

Szczyrba, L., Mulligan, R., Pufahl, P., Humberston, J., & McNinch, J. 2024. ***Nearshore flow dynamics over shore-oblique bathymetric features during storm wave conditions***. Journal of Geophysical Research: Oceans.

Thomas, N., Pertiwi, A.P., Traganos, D., Lagomasino, D., Poursanidis, D., Moreno, S., & Fatoyinbo, L. 2021. ***Space-borne cloud-native Satellite-Derived Bathymetry (SDB) models using ICESat-2 and Sentinel-2***. Geophys. Res. Lett., 48 (4), e2020GL092170.

Vargas, R.; Wasserman, J.C.d.F.A.; da Silva, A.L.; Tavares, T.L.; dos Santos, C.A.; Dias, F.F. ***Satellite-Derived Bathymetry models from Sentinel 2-A and 2B in the coastal clear waters of Arraial Do Cabo, Rio de Janeiro, Brazil***. Rev. Bras. Geogr. Fís. 2021, 14, 3078.

Vanneste, M., Sultan, N., Garziglia, S., Forsberg, C. F., & l'Heureux, J. S. 2014. ***Seafloor instabilities and sediment deformation processes: the need for integrated, multi-disciplinary investigations***. Marine Geology, 352, 183-214.

Wang, X., & Andutta, F. (2013). ***Sediment transport dynamics in ports, estuaries and other coastal environments***. https://doi.org/10.5772/51022.

Wölfl, A. C., Snaith, H., Amirebrahimi, S., Devey, C. W., Dorschel, B., Ferrini, V., & Wigley, R. 2019. ***Seafloor mapping–the challenge of a truly global ocean bathymetry***. Frontiers in Marine Science, 6, 283.